IPP-Report

Max-Planck-Institut
für Plasmaphysik

Alex Versteegh

Untersuchung eines lang lebenden atmosphärischen Plasmoids

Analysis of a Long Living Atmospheric Plasmoid

IPP 13/10
Juni, 2008

Analysis of a Long Living Atmospheric Plasmoid

Thesis

to obtain the degree of Master of Science in Applied Physics at

Technische Universiteit Eindhoven
Factulteit Technische Natuurkunde

about the research conducted at

Humboldt Universität zu Berlin
Arbeitsgruppe Plasmaphysik

Author:
Alex Versteegh

Supervisors:
Prof. Dr. Gerd Fussmann
Prof. Dr. Burkhard Jüttner
Prof. Dr. Ir. Gerrit Kroesen

November 12, 2007

Abstract

Ball-like plasmoids were generated from discharging a capacitor bank via a water surface. In the autonomous stage after current zero they have diameters up to 0.2 m and lifetimes of some hundreds milliseconds, thus resembling ball lightning in some way. They were studied by means of spectroscopy, high speed cameras, probes and calorimetric measurements. The plasmoids are found to consist of a true plasma confined by a cold envelope. Decreasing electron densities in the order of 10^{20} m^{-3} to 10^{22} m^{-3} were measured from Stark broadening in the initial (formation) phase. The central electron temperature is found to be 2000–5000 K during most of the plasmoids lifetime. This is determined from intensity ratios of copper lines, assuming local thermodynamic equilibrium and considering optical thickness, as well as from a collisional radiative model for atomic calcium. Gas temperatures above 1300 K have been measured using thermocouples and it is expected to reach values in the range of 2000 K to 4000 K during formation. The plasmoids store chemical energy by dissociating water at their formation, as is supported by spectroscopic investigations of OH-radical emission and by the outcomes of a thermodynamical model assuming chemical equilibrium. Calcium hydroxide (CaOH) molecular band emission is the major source of visible radiation in the autonomous phase. Chemiluminescence reactions between dissociation products of water and dissolved calcium are proposed as a source for this emission. The plasmoids colder boundary layer consists of electric double layers. Vortices have been observed that likely attribute to the characteristic shape of the balls.

Contents

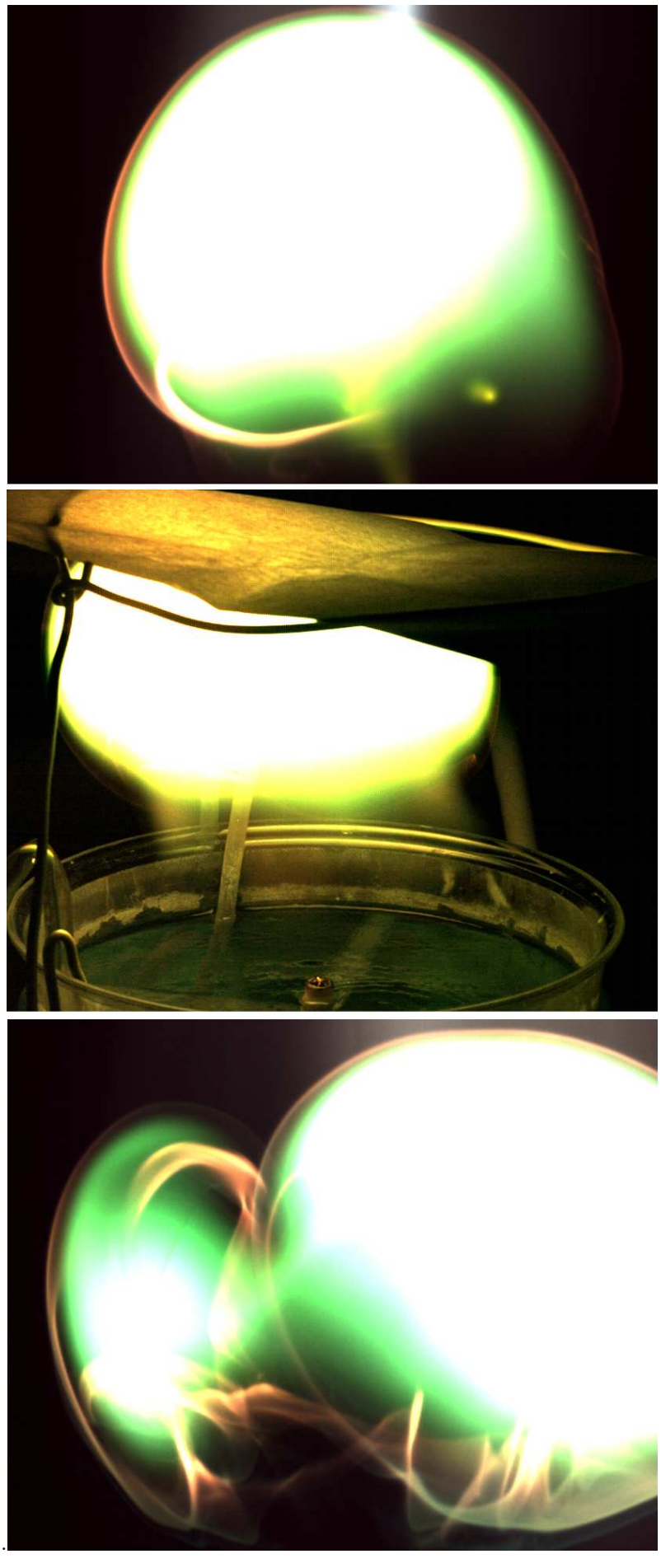

FIGURE 1: *Examples of atmospheric plasmoids. The top image was recorded using high exposure at 30 ms after quenching the discharge current. It clearly shows the distinct boundary layer surrounding the ball-shaped plasmoid, which is approximately 20 cm in diameter. The central image shows an experiment in which a sheet of paper placed in the path of the discharge. The paper is not burnt and the plasmoid deforms. The figure on the bottom shows a rare case of a double plasmoid, with remarkable turbulent structures in the boundary layer*

Chapter 1

Introduction

Over the last few years, luminous plasmoids generated from an electric discharge in a water vessel at atmospheric pressure were described in a number of papers (see [1, 2, 3] and the references therein). These experiments are all based on those first described by Shabanov [4] in St. Petersburg in 2001. The experiments, including our own, received remarkable attention in and outside the physics community because they were associated with natural ball lightning.

The mysterious phenomenon of ball lightning has puzzled scientist for centuries. No satisfying explanation for its occurrence has been found to the present day. No model exists that can account for all the reported observations and the ones that do exist, lack experimental evidence. Inevitably, some rather wild speculations surround the subject. A review of some of the ball lightning models developed over the years, as well as a statistical analysis of a large collection of observational data, is written by Smirnov [5].

An recent interesting collection of ball lightning sightings, collected by correspondence with eye-witnesses was published by Abrahamson *et al.* [6]. A ball-lightning theory that received much attention was developed by Abrahamson and Dinnis [7]. It is based on the idea that a lightning strike on soil forms nanoparticles of Si, SiO or SiC, which are ejected into the air as filamentary networks. As these networks oxidize in the atmosphere, the stored energy is released as light and heat.

Very recent experiments by the Brazilian group of Paiva *et al.* also generated some attention [8]. These authors managed to produced bright glowing objects the size of ping-pong balls from a DC arc discharge ($\sim$ 20 V, 140 A) on a silicon wafer. They roll and bounce on the floor and some glow as long as 8 seconds. The authors claim that their experiments forms experimental support for the Abrahamson-Dinnis theory. However, the appearance of the 'sparks' does not resemble reported ball lightning observations very accurately.

The analogy of the present experiments with natural ball lightning will not be elaborated on in this report. However tables 1.1 and 1.2 are presented to sketch a picture of the natural phenomenon, so a quick comparison can be made. Based on these tables and other properties determined from observations, the 'average' ball lightning can be described as a sphere with a diameter of 20 cm, a lifetime of about 10 s, and a luminosity similar to a 100 W light bulb. It floats freely in the air, and ends either in an explosion, or by fading away. It mostly occurs during stormy weather.

Parameter	Value	No. cases
Diameter	23 ± 5 cm	3763
Lifetime	$9 \cdot 10^{\pm 0.3}$ s	2111
Brightness	1500 ± 200 lm	1918

TABLE 1.1: *Parameters of the mean ball lightning, determined from collections of observations [5]. The number of sightings from which a value for each parameter could be obtained is also listed.*

The present work repeats the experiment of Shabanov and co-workers [1, 2], adding a variety of diagnostics to get better insight into the phenomenon illustrated in figure 1. Some simple models will also be presented. Perhaps already from the appearance of the plasmoids, it becomes clear

Table 1.2: *Probabilities associated with various properties of ball lightning, determined from collections of observations [5].*

Parameter	Characteristic	Probability [%]	No. cases
Form	spherical	91 ± 1	2891
Color	orange	25 ± 10	3497
	yellow	20 ± 3	
	white	19 ± 5	
	red, pink	17 ± 1	
	blue, violet	12 ± 1	
	green	1.4 ± 0.3	
	mixture	6 ± 3	
Decay	explosion	52 ± 9	2291
	slow decay	39 ± 7	
	fragments	9 ± 3	
Place of	indoors	50 ± 5	1984
observation	outdoors	50 ± 5	

that a vast amount of physics would be needed to completely understand their nature. So, the models focus on some very particular aspects of it – and can in no way replace the experiments. Specifically, the investigations are aimed at understanding the energy storage mechanism that enables the autonomously radiating behavior of the plasmoids. Also of interest are *e.g.* the characteristic colors, spherical shape and apparently confining boundary layer or 'skin' surrounding them. Of course, to achieve an understanding in qualitative as well as quantitative terms, it is a first and important goal to determine (plasma) parameters such as densities and temperatures, as well as chemical composition.

Most experimental effort was put into emission spectroscopy. As one of the best established diagnostic tools in plasma physics, it provides a wealth of information on the processes and parameters governing the plasma [9, 10, 11]. Moreover it is a non-invasive technique and insensitive to the presence of large electric or magnetic fields, RF-signals, or a high plasma potential, that can sometimes severely complicate the use of other diagnostics. Nevertheless, other measurement techniques (*e.g.* cameras, electric probes, thermocouples) were also used – simultaneously when possible – and provide useful and important additional information.

Finally a few words are said about the institute and the background of the project. The experimental setup was built in the summer of 2006 as a demonstration experiment of the Institute for Plasma Physics at Humboldt University. It was presented at the visitor's day 'Lange Nacht der Wissenschaften' of the scientific institutes in Berlin and Potsdam and received much attention as such. The experiment was considered worthwhile and interesting and the decision was made at the institute to further investigate the subject. I was the first graduation student to join the then three person project team, which was completed by another student about a month later. The experiments were planned to last one year. Some preliminary results were already presented on other occasions: at the spring meeting of the German Physical Society (DPG Tagung) in Düsseldorf in April 2007 (presentation) and at the International Conference on Ionized Gases (ICPIG) in Prague in July (poster and talk). Most recently, an article was submitted for publication in the Plasma Sources Science and Technology journal [12]. An interesting side-effect of unconventional nature of the experiments is that they received some media attention in Germany and the Netherlands, featuring in television programs and articles in popular magazines.

The structure of the rest of this report is as follows: chapter 2 discusses some the most important plasma physics concepts and serves as theoretical background, to which will be referred in the following chapters. Next, conducted experiments are described, directly followed by their results and discussions. The following two chapters are devoted to a collisional radiative model for calcium, and molecular processes and molecular emission. Experimental results specifically related to these topics are also discussed in these chapters. General points of discussion as well as conclusions follow towards the end. Most figures (graphs) are included at the appropriate place in the report. An exception form very large figures or extensive series of similar results. These are presented in appendices, to which reference is made.

Chapter 2

Plasma physics concepts

2.1 Definitions, classifications

A plasma is a partly of fully ionized gas. More precisely a plasma is a gas in which so many of the atoms or molecules have lost (gained) one or more electrons that the electrical interaction between the charged particles starts to dominate their behavior over the normal "hard sphere" collisions and Van der Waals attractions involving neutral particles. A plasma contains positive and negative charge carriers moving freely and independently of each other, resulting in a high electric conductivity.

Many of the parameters used to describe a plasma, such as density, pressure and temperature, are the same as in basic kinetic theory of gases. An important difference is that one must distinguish between particles of different charge states (*e.g.* neutrals, ions, and electrons). For instance, when the plasma is not in (complete or local) thermodynamic equilibrium, as is often the case in laboratory plasmas, the temperature of the ions T_i and neutrals T_g can be significantly different from that of the electrons T_e. The electron (or ion) temperature is often expressed in energy units (electron volt, eV: 1 eV $\sim$ 11604 K).

An important property of a plasma is the *ionization degree* α, defined by:

$$\alpha = \frac{n_\mathrm{i}}{n_0 + n_\mathrm{i}}. \tag{2.1}$$

Here n_i is the ion- and n_0 is the neutral density. If there are molecules present in a plasma, these can dissociate and the *dissociation degree* β is defined in a similar way, *e.g.* for $\mathrm{H_2O} \rightarrow \mathrm{OH} + \mathrm{H}$:

$$\beta = \frac{n_\mathrm{OH}}{n_{\mathrm{H_2O}} + n_\mathrm{OH}}, \tag{2.2}$$

so that a dissociation degree of 1 means complete dissociation.

The ion density is related to the electron density through the important concept of *quasi neutrality* which says that in a plasma there can be no significant deviation from charge neutrality over a distance larger than the *Debye length* λ_D:

$$\frac{n_\mathrm{e} - Zn_\mathrm{i}}{n_\mathrm{i}} = \epsilon \ll 1. \tag{2.3}$$

Here Z is the average ion charge in the plasma and ϵ is a small number, depending on the size of the measurement volume V: $\epsilon \approx 0$ for $V \gg \lambda_\mathrm{D}^3$. In other words, on a macroscopic scale the plasma is neutral:

$$n_\mathrm{e} - Zn_\mathrm{i} = 0. \tag{2.4}$$

Since electrons and ions can move freely, a change in the electric potential *e.g.* through the introduction of a test particle with charge q into the plasma, will alter the movement of the surrounding electrons and ions. The net effect is a "shielding" or "screening" of the normal

Coulomb potential $\Phi(r) = \frac{q}{4\pi\epsilon_0 r}$ at distance r of the test particle, which is replaced with the *Debye potential* [13]:

$$\Phi(r) = \frac{q}{4\pi\epsilon_0 r} \exp\left(-\frac{r}{\lambda_\mathrm{D}}\right), \tag{2.5}$$

with ϵ_0 the vacuum permittivity. The Debye length for a plasma with singly charged ions is given by:

$$\lambda_\mathrm{D} = \sqrt{\frac{\varepsilon_0 k_\mathrm{B} T_\mathrm{e} T_\mathrm{i}}{e^2(n_\mathrm{e} T_\mathrm{i} + n_\mathrm{i} T_\mathrm{e})}} \approx \sqrt{\frac{\epsilon_0 k_\mathrm{B} T_\mathrm{e}}{n_\mathrm{e} e^2}}, \tag{2.6}$$

with e the elementary charge and k_B the Boltzmann constant. At a distance $r \gg \lambda_\mathrm{D}$ of the test particle, its disturbing effect on the plasma potential is completely suppressed; hence this is called *Debye shielding*.

Plasmas can be classified into *ideal* and *non-ideal* plasmas. The definition of an ideal plasma can be derived analogous to the definition of an ideal gas. A gas is called ideal when the average interaction energy (through Van der Waals interactions) between the molecules is small compared to their average kinetic energy $E_\mathrm{kin} = \frac{3}{2} k_\mathrm{B} T$, which is the case for sufficiently high temperature and distance between the molecules. In the case of a plasma, the Coulomb interaction energy:

$$\Phi_{12} = \frac{1}{4\pi\epsilon_0} \frac{q_1 q_2}{r_{12}} \tag{2.7}$$

takes the place of the Van der Waals interaction energy. Assuming a plasma with singly charged ions $q_1 = q_2 = e$ and density $n_\mathrm{i} = n_\mathrm{e} = n$, the average distance between the particles r_{12} is given by $n^{-1/3}$. So, a plasma is called ideal when:

$$\frac{e^2 n^{1/3}}{4\pi\epsilon_0} \ll \frac{3}{2} k_\mathrm{B} T \quad \text{or} \quad T \gg 1.11 \cdot 10^{-5} n^{1/3}, \tag{2.8}$$

with T in K and n in m^{-3}.

Another way to arrive at the same criterion for an ideal plasma involves the concept of Debye screening. The electrons or ions surrounding the test particle discussed above can only effectively screen the potential of this test-particle when macroscopically large number of plasma particles is present in the shielding cloud. In other words the number of particles N_D in a sphere with radius λ_D, the *Debye sphere*, should be large:

$$N_\mathrm{D} = n_\mathrm{e} \frac{4}{3} \pi \lambda_\mathrm{D}^3 = n_\mathrm{e} \frac{4}{3} \pi \left(\frac{\epsilon_0 k_\mathrm{B} T_\mathrm{e}}{n_\mathrm{e} e^2}\right)^{3/2} \gg 1, \tag{2.9}$$

which is the same as equation (2.8) apart from a constant factor. For example, a plasma with a density of 10^{22} m^{-3} is ideal for $T \gg 240$ K according to 2.8.

Finally, the word *plasmoid* deserves some explanation. The term is used to refer to a localized (compact) plasma formation (plasma entity) that possesses a coherent structure. In literature the term plasmoid is sometimes used to refer specifically to a *magnetically* confined plasma or a plasma of which the structure is determined by magnetic fields. It is emphasized that this is not the definition used here; the use of the term plasmoid does not imply any form of magnetic confinement.

2.2 Collisions and cross sections

The frequency with which a particle moving at speed v in a plasma of density n collides can be written as:

$$f_\mathrm{c} = v \sigma_\mathrm{c} n, \tag{2.10}$$

which defines the collision *cross section* σ_c. The related (average) collision time τ_c and collision mean free path λ_{mfp} are defined by:

$$\tau_c = \frac{1}{f_c} \quad \text{and} \quad \lambda_{mfp} = v/f_c. \tag{2.11}$$

The total number of collisions between particles of type 1 and 2 per unit time and volume is given by $n_1 n_2 \langle \sigma_c v \rangle$. The angular brackets indicate the values are averaged over all particles, the energies of which are distributed according to a distribution function $f(\epsilon)$:

$$\langle \sigma v \rangle = \int \sigma_c(\epsilon) v(\epsilon) f(\epsilon) d\epsilon. \tag{2.12}$$

This averaged product of cross section and velocity is called the *rate coefficient* $K_c \equiv \langle \sigma_c v \rangle$.

Cross sections and rate coefficients are easily calculated for hard sphere collisions between uncharged particles, *e.g.* $\sigma_c \approx \pi a_0^2$, where a_0 is the Bohr radius. For other processes, obtaining accurate energy dependent cross sections or, in the case of a Maxwellian velocity distribution, temperature dependent rate coefficients can be much more difficult. When no experimental data is available and accurate quantum mechanical calculations are to complex, one often has to rely on rough theoretical approximation. Three examples that are relevant to the model in chapter 4 will be given:

(a) the excitation of bound electrons into higher electronic states by collision with an electron: *electron impact excitation*,

(b) the removal of a bound electron from an atom or ion by collision with an electron: *electron impact ionization* and

(c) The recombination of a free electron with an ion while emitting a photon: *radiative recombination*.

2.2.1 Electron impact excitation

In electron impact excitation the free electron transfers a discrete amount of energy E_{pq} that 'fits' to a particular electronic transition (from state p to q), to the bound electron. Of course the incident electron must have an initial energy greater than this value, so there is a threshold behavior of the cross section.

There is a large collection of formulae for cross sections and rate coefficients available in literature, based on several collision theories. Most of these have a limited range of validity, *e.g.* based on the ratio of the transition energy and the electron temperature $\epsilon_{pq} = E_{pq}/kT_e$. Vriens and Smeets [14] connect several of these approximations into semi-empirical formulae with a large range of validity for the incident electron energy or electron temperature. Their result for the electron-impact excitation rate coefficient (assuming Maxwellian EEDF) is:

$$K_{pq} = \frac{1.6 \cdot 10^{-13} \sqrt{k_B T_e}}{k_B T_e + \Gamma_{pq}} e^{\epsilon_{pq}} \left[\mathcal{A}_{pq} \ln \left(\frac{0.3 k_B T_e}{R_y} + \Delta_{pq} \right) + \mathcal{B}_{pq} \right] [\mathrm{m^3 s^{-1}}], \tag{2.13}$$

with $k_B T_e$ and R_y, the Rydberg energy, both in eV and

$$\Delta_{pq} = \exp\left(-\frac{\mathcal{B}_{pq}}{\mathcal{A}_{pq}} \right) + \frac{0.06 s^2}{q p^2}, \tag{2.14}$$

with $s = q - p$ and

$$\Gamma_{pq} = \frac{R_y \cdot \ln\left(1 + \frac{p^3 k_B T_e}{R_y}\right) \left[3 + 11 \frac{s^2}{p^2}\right]}{6 + 1.6 q s + \frac{0.3}{s^2} + 0.8 \frac{q^{1.5}}{\sqrt{s}} |s - 0.6|}. \tag{2.15}$$

The variables p and q (as opposed to the indices that are used to label the states) are the *effective quantum numbers* of the initial and final energy levels, given by:

$$p = Z\sqrt{R_\mathrm{y}/\chi_p} = Z\sqrt{R_\mathrm{y}/(E_+ - E_p)}. \tag{2.16}$$

The variables $\mathcal{A}_{pq}$ and $\mathcal{B}_{pq}$ are given by:

$$\mathcal{A}_{pq} = 2(R_\mathrm{y}/E_{pq})f_{pq}, \tag{2.17}$$

with f_{pq} the absorption oscillator strength and

$$\mathcal{B}_{pq} = \frac{4R_\mathrm{y}^2}{q^3}\left(\frac{1}{E_{pq}^2} + \frac{4E_{pi}}{3E_{pq}^3} + b_p\frac{E_{pi}^2}{E_{pq}^4}\right), \tag{2.18}$$

where b_p can be approximated by:

$$b_p = \frac{1.4\ln(p)}{p} - \frac{0.7}{p} - \frac{0.51}{p^2} + \frac{1.16}{p^3} - \frac{0.55}{p^4}. \tag{2.19}$$

For many (optically allowed) transitions of many elements the absorption oscillator strength f_{pq} can be found in the NIST [15] database. For optically *forbidden transitions* the situation is more complicated and accurate rate coefficients are often more difficult to obtain. When no other data is available the following approximation can be used [16]:

$$f_{pq} = 1.52p^{-5}q^{-3}(p^{-2} - q^{-2})^{-3} \quad \text{for} \quad s/p \ll 1, \tag{2.20}$$

and

$$f_{pq} = 1.95p^{-5}q^{-3}(p^{-2} - q^{-2})^{-3} \quad \text{for} \quad s/p \gtrsim 1. \tag{2.21}$$

These formulae all assume a hydrogenic structure of the atom and become more accurate for transitions between higher excited states. The rate coefficients calculated using 2.13 or similar methods can have significant errors – of more than an order of magnitude – for transitions between low-lying states in non-hydrogenic elements, where the influence of the atomic electron cloud is large.

Experimentally derived electron impact excitation cross section are often only available for a small number of transitions (when at all). The best theoretical results are obtained from quantum mechanical *R-matrix* calculations. The results of such calculations (for a Maxwellian electron energy distribution) are usually given in terms of an *effective collision strength* Υ_{pq} ('Upsilon'). It is defined by

$$\Upsilon_{pq} = \int_0^\infty \sigma_{pq}(\epsilon)\exp\left(-\frac{\epsilon}{k_\mathrm{B}T_\mathrm{e}}\right)d\left(\frac{\epsilon}{k_\mathrm{B}T_\mathrm{e}}\right). \tag{2.22}$$

Υ_{pq} is related to the excitation rate coefficient by

$$K_{pq}^\mathrm{exc} = 2\sqrt{\pi}\alpha c a_0^2\frac{1}{g_p}\sqrt{R_\mathrm{y}/k_\mathrm{B}T_\mathrm{e}}\exp(-E_{pq}/k_\mathrm{B}T_\mathrm{e})\Upsilon_{pq}. \tag{2.23}$$

Here, $2\sqrt{\pi}\alpha c a_0^2 = 2.1716\cdot 10^{-14}$ m^{3}s^{-1}, g_p is the degeneracy of the lower state involved in the transition (usually $2J+1$, with J the total spin+orbital angular momentum quantum number).

2.2.2 Electron impact ionization

The bound electron is trapped in the atom's or ion's potential, which lies an amount of χ_p, the ionization energy for the initial state p, below the continuum potential. For ionization to take place the incident electron must have an energy greater than this value. So there is an energy threshold

in the ionization cross section and the process becomes important at higher temperatures. A semi-empirical formula for the rate coefficient is [14]:

$$K_{p+}^{\mathrm{ion}} = \frac{9.56 \cdot 10^{-12} (k_{\mathrm{B}} T_{\mathrm{e}})^{-1.5} \mathrm{e}^{-\epsilon_{p+}}}{\epsilon_{p+}^{2.33} + 4.38 \epsilon_{p+}^{1.72} + 1.32 \epsilon_{p+}} \ [\mathrm{m}^3 \mathrm{s}^{-1}], \tag{2.24}$$

where $\epsilon_{p+} = \chi_p/(k_{\mathrm{B}} T_{\mathrm{e}})$. K_{p+}^{ion} is the rate per atomic electron and needs to be summed over all significant electrons in the atom if the total ionization cross section for the atom is required. Usually only those in the uppermost level need to be considered. Occasionally, lower levels should also be included, with the ϵ_{p+} appropriate for each level. Other semi-empirical expressions can be found elsewhere [17, 10, 18]. Note that though this section refers to ionization of an atom, we can apply the same formula to ionization from stage, say, r to stage $r+1$. Since higher ionization stages are not relevant for the experiments conducted, this generalization will not be made explicit in the following sections.

2.2.3 Radiative recombination

A free electron can be captured by an ion and end up in a bound state (principal quantum number n) with energy $-\chi_n$ while emitting a photon with a wavelength $\lambda_{\mathrm{fb}} = hc/(\chi_n + \epsilon)$ with h Planck's constant with c the speed of light and ϵ the incident electron energy. Since the final electron energy is negative (bound) there is no energy threshold in the cross section for radiative recombination. The rate coefficient decreases with temperature. An approximation for the rate coefficient for hydrogenic ions with charge Z is [10]:

$$K_{+n}^{\mathrm{rr}} = 5.2 \cdot 10^{-20} Z \left(\frac{Z^2 R_{\mathrm{y}}}{n^2 T_{\mathrm{e}}} \right)^{1/2} \frac{\chi_n}{T_{\mathrm{e}}} \left[\exp\left(\frac{\chi_n}{T_{\mathrm{e}}} \right) \mathrm{Ei}\left(\frac{\chi_n}{T_{\mathrm{e}}} \right) \right] \bar{g}_n \ [\mathrm{m}^3 \mathrm{s}^{-1}], \tag{2.25}$$

where

$$\mathrm{Ei}(x) = -\int_{-x}^{\infty} \frac{\exp(-s)}{s} ds \tag{2.26}$$

is the exponential integral. Values $\bar{g}_n$ are in the order of 1 and can be found in literature [19]. For a level that is partially filled the rate should be corrected by a factor $\xi/(2n^2)$, where ξ is the number of available 'holes' in that level. For the lower levels (high χ_n) the ionization energy is usually much higher than the electron temperature in equilibrium and the asymptotic behavior for the term in brackets is useful:

$$\exp\left(\frac{\chi_n}{T_{\mathrm{e}}} \right) \mathrm{Ei}\left(\frac{\chi_n}{T_{\mathrm{e}}} \right) \to \frac{T_{\mathrm{e}}}{\chi_n} \quad \text{for} \quad \frac{\chi_n}{T_{\mathrm{e}}} \to \infty. \tag{2.27}$$

For a singly charged ion, taking $\bar{g} = 1$, and $T_{\mathrm{e}} \ll \chi_n$ equation (2.25) simply becomes:

$$K_{+n}^{\mathrm{rr}} = 5.2 \cdot 10^{-20} \frac{1}{n} \sqrt{R_{\mathrm{y}}/T_{\mathrm{e}}}. \tag{2.28}$$

The total recombination rate can be obtained by summing equation (2.27) over all n. A reasonable approximation is [10]:

$$K_{+,\mathrm{tot}}^{\mathrm{rr}} = 5.2 \cdot 10^{-20} \frac{Z}{2} \left(\frac{Z^2 R_{\mathrm{y}}}{T_{\mathrm{e}}} \right)^{1/2} \left(1 - \exp\left[\frac{-\chi}{T_{\mathrm{e}}} \left(1 + \frac{1}{n_0} \left[\frac{\xi}{n_0^2} - 1 \right] \right) \right] \right) \left(\left[\ln \frac{\chi}{T_{\mathrm{e}}} \right]^2 + 2 \right)^{1/2}, \tag{2.29}$$

where n_0 is the principal quantum number of the lowest incompletely filled shell of the ion and χ is the ionization potential of the recombined atom.

For the recombination to individual states, a more advanced treatment that uses cross sections depending on the angular momentum l can be found in [20]. The resulting rate coefficients $K_{+,nl}^{\mathrm{rr}} = K_{+,nl}^{\mathrm{rr}}(\Theta)$ are tabulated as a function a scaled electron temperature $\Theta = T_{\mathrm{e}}/Z_{\mathrm{eff}}^2$. Here,

Z_{eff} is an effective ion charge. For this, approximate formulae depending on the core charge and the number of bound electrons as well as the incident electron energy (weakly) are also given. The rate coefficients peaks at a temperature around $\Theta = 10^{-4}$ and decrease with increasing principle quantum number, so that radiative recombination is most important for the low lying states.

2.3 Equilibrium plasmas

In a plasma, many atomic and molecular processes occur simultaneously. Only a few of these have been described in the previous section. In general, in order to determine the distribution of particles over all their different states, including ionization stages, excitation states, velocities, etc. one would have to know all these processes in detail. The situation becomes extremely much simpler when the plasma is in thermal equilibrium (TE). The system will then be in the most probable state, which is found by quantum statistical mechanics.

2.3.1 Boltzmann and Saha balances

In equilibrium for every process the number of reactions going forward is equal to the number of reactions going backward. This is called the principle of *detailed balancing*. This principle can be applied to the process of excitation of an atom X from state p to state q by electron impact and the reverse deexcitation:

$$\mathrm{X}_p + \mathrm{e}^-(\epsilon + E_{pq}) \;\rightleftarrows\; \mathrm{X}_q + \mathrm{e}^-(\epsilon), \tag{2.30}$$

with $E_{pq} = E_q - E_p$. In equilibrium, the occupation of the excitation states follows from well known Boltzmann statistics. If the states are non-degenerate, the ratio of the occupation of states p and q is given by a simple Boltzmann factor:

$$\frac{n_q}{n_p} = \exp(-E_{pq}/k_{\mathrm{B}}T_{\mathrm{e}}). \tag{2.31}$$

If the states are g_i-fold degenerate, the ratio becomes:

$$\frac{n_q}{n_p} = \frac{g_q}{g_p}\exp(-E_{pq}/k_{\mathrm{B}}T_{\mathrm{e}}), \tag{2.32}$$

what is called the *Boltzmann balance*.

In the case of ionization (here from the ground state neutral X_0^0 to the ground state first ionized stage X_0^+) and radiative recombination the number of free particles involved in the forward and backward reaction is no longer equal:

$$\mathrm{X}_0^0 + \mathrm{e}^-(\epsilon + \chi_{0,0}) \;\rightleftarrows\; \mathrm{X}_0^+ + \mathrm{e}^-(\epsilon) + e^-. \tag{2.33}$$

The balance must be altered to include the number of possible states (statistical weight) per unit of volume of the extra free electron in the ionized stage. This is given by the electrons' internal degeneracy (2, for the spin states), times the number of possible states for the free electron in phase space given by $u_{\mathrm{e}}{=}(2\pi m_{\mathrm{e}}k_{\mathrm{B}}T_{\mathrm{e}})^{3/2}/h^3$. When the degeneracy of the ion ground state is $g_{+,0}$, the total statistical weight for the ion and the free electron equals $g = 2u_e g_{+,0}$. So the balance becomes:

$$\frac{n_{\mathrm{e}}n_{+,0}}{n_{0,0}} = 2\frac{(2\pi m_{\mathrm{e}}k_{\mathrm{B}}T_{\mathrm{e}})^{3/2}}{h^3}\frac{g_{+,0}}{g_{0,0}}\exp(-\chi_{0,0}/k_{\mathrm{B}}T_{\mathrm{e}}). \tag{2.34}$$

This is called the *Saha balance*. By summing the occupations of all possible electronic stages in the neutral and ionized stage, one can arrive at a similar formula for the *total* neutral density $n_0 = \sum_0^{p_{\max}} n_{0,p}$ and ion density $n_+ = \sum_0^{q_{\max}} n_{+,q}$:

$$\frac{n_{\mathrm{e}}n_{+}}{n_{0}} = 2\frac{(2\pi m_{\mathrm{e}}k_{\mathrm{B}}T_{\mathrm{e}})^{3/2}}{h^3}\frac{Q_{+}}{Q_0}\exp(-\chi/k_{\mathrm{B}}T_{\mathrm{e}}). \tag{2.35}$$

where

$$Q_r = \sum_p g_{r,p} \exp(-\frac{E_{r,p} - E_{r,0}}{k_B T_e}) \tag{2.36}$$

is the total number of particles in each ionization stage, called the partition function. For a plasma with only singly charged ions and atoms, where $n_e = n_+$ this ratio can be used to calculate the ionization degree $\alpha = n_e/(n_e + n_0)$ when the electron density and temperature are known.

For hydrogen like atoms or ions the ratio of the ground state densities given by equation (2.34) can be used as a good approximation to calculate the ionization degree without the need to calculate the partition functions, since the occupation of the excited states is only a small fraction of that of the ground state. For other atoms, such as alkali or alkaline earth metals, which have lower lying excited states that can reach populations of more than 10% of the ground state occupation, this is only a rough approximation.

As a numerical example, the ionization degree of a plasma containing calcium atoms and ions is plotted in figure 2.1, using both equation (2.34) and equation (2.35). The (temperature dependent) partition functions have been approximated by a polynomial expansion from literature [21]. De decrease in ionization degree with increasing density is due to the fact that the backward process (3 particle recombination) is proportional to n_e^2 and thus becomes more important for higher n_e.

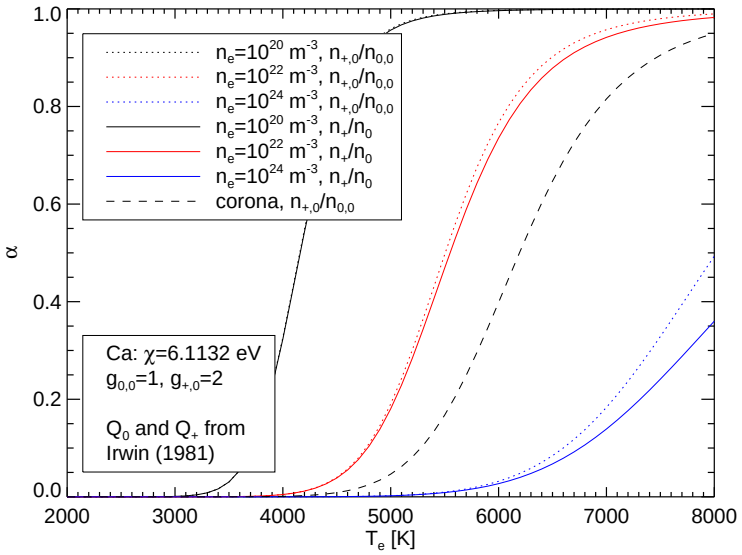

Figure 2.1: *Equilibrium ionization degree of a calcium plasma at different electron densities, calculated using equation (2.34) for the ratio of the ground state occupations (dotted lines) and using equation (2.35) for the total ionization stage balance (solid lines). For the latter case the partition functions were approximated by a polynomial expansion from [21]. The occupation of higher ionization stages is negligible so $n_e = n_+$ is assumed. Also included is the ionization degree in coronal equilibrium, calculated using equation (2.48) (dashed line).*

Instead of assuming values for electron density and temperature to calculate the Saha-balance, one can also assume a closed system, where the total number of calcium atoms and (singly charged) ions is fixed: $n_+ + n_0 = n_{tot}$. Writing the fraction of the ions belonging to the considered species as x, quasineutrality can be use to write this as $xn_e + n_0 = n_{tot}$. At given (constant) x, n_{tot} and T_e this equation together with the saha-balance (2.34) gives a system of two equations for the two unknown concentrations $n_+ = xn_e$ and n_0. This system can by solved analytically (`Mathematica` is used here), giving:

$$n_+ = \frac{1}{2g_0 h^3} \exp(-\frac{E_{ion}}{k_B T_e})[-4\sqrt{2} g_+ k_B m_e \pi^{3/2} T_e \sqrt{k_B m_e T_e} x + 4\{\sqrt{2} \exp(\frac{E_{ion}}{k_B T_e}) g_0 g_+ h^3 k_B m_e n_{tot} \pi^{3/2} T_e \sqrt{k_B m_e T_e} x + 2 g_+^2 k_B^3 m_e^3 \pi^3 T_e^3 x^2\}^{1/2}] \tag{2.37}$$

and

$$n_0 = n_{tot} - n_+. \tag{2.38}$$

This solution is plotted for the case of calcium with a total density of $n_{\text{tot}} = 4 \cdot 10^{20}$ m^{-3} and $x = 1$ in figure 2.2.

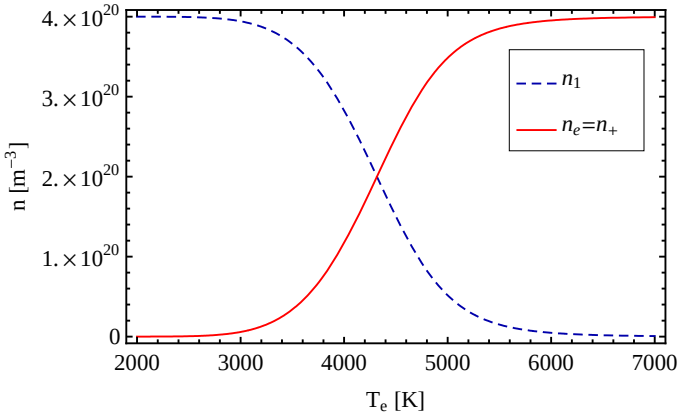

FIGURE 2.2: *Calcium ground state and ion densities for a closed system with total density $n_{\text{tot}} = 4 \cdot 10^{20}$ m^{-3} at temperature T_e, calculated using equations (2.37) and (2.38). A single ion species (calcium) is assumed,* i.e. *$x = 1$ (see text).*

2.3.2 Rate coefficients for reverse processes

The rate coefficients for electron impact excitation and ionization were discussed in section 2.2. By applying the Boltzmann and Saha balances the rate coefficients for the reverse processes can be calculated from them.

Electron impact deexcitation

In equilibrium the number of forward and backward reactions in equation (2.30) is equal, so it holds:

$$n_p n_e K_{pq} = n_q n_e K_{qp} \quad \text{or} \quad \frac{n_q}{n_p} = \frac{K_{pq}}{K_{qp}} \tag{2.39}$$

Comparing this with the Boltzmann balance, the rate coefficient K_{qp}^{deexc} for electron impact deexcitation follows from the coefficient for excitation by:

$$K_{qp}^{\text{deexc}}(T_e) = \frac{g_p}{g_q} \exp(\Delta E_{pq}/k_B T_e) K_{pq}^{\text{exc}}(T_e). \tag{2.40}$$

This relation, and the following derived analogously, also hold when there is no equilibrium, as long as the electron velocity distribution is Maxwellian.

Three-particle recombination

The rate coefficient for three particle recombination K_{+p}^{tpr} (from the ion ground state) follows from the coefficient for ionization if we apply the Saha balance to reaction (2.33):

$$n_{0,p} n_e K_{p+} = n_{+,0} n_e^2 K_{+p} \tag{2.41}$$

and

$$K_{+p}^{\text{tpr}}(T_e) = \frac{g_p}{2g_{+,0}} \frac{h^3}{(2\pi m_e k_B T_e)^{3/2}} \exp(\chi_p/T_e) K_{p+}^{\text{ion}}(T_e). \tag{2.42}$$

The total three body recombination rate is obtained by summing the above rates for the individual p, which results in approximately [22, 23]:

$$K_{+,\text{tot}}^{\text{tpr}} = \bar{g}(1.1 \cdot 10^{-49}) Z^3 \left(\frac{R_y}{k_B T_e}\right)^{9/2} \quad [\text{m}^6\text{s}^{-1}], \tag{2.43}$$

where $\bar{g} \approx 2$ and Z is the charge (in elementary units) of the ion.

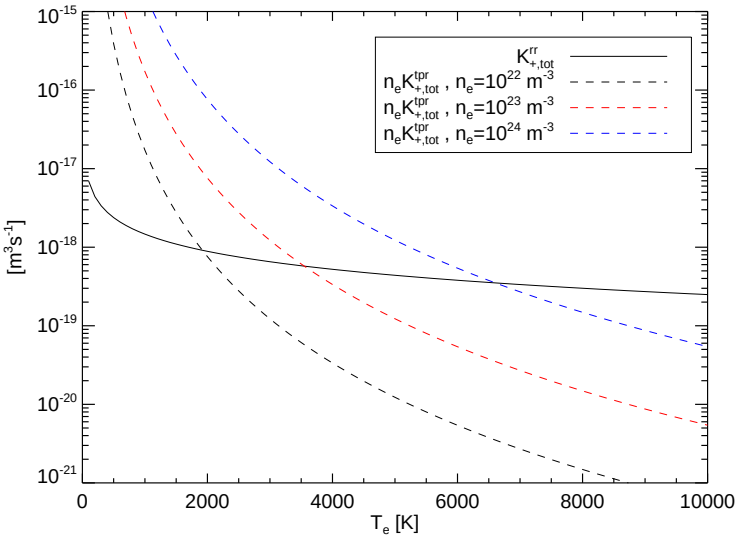

Figure 2.3: *Total radiative recombination rate coefficient $K^{rr}_{+,tot}$ (solid line) and total three-particle recombination coefficient $K^{tpr}_{+,tot}$ times n_e for three different electron densities (dashed lines) for atomic calcium, calculated using equation equations (2.29) and (2.43) respectively.*

An example is given in figure 2.3 for atomic calcium. The total recombination rate per unit of electron density and ion density is calculated using equations (2.29) and (2.43) for radiative and three-particle recombination respectively. The following values were used: $Z = 1$, $\chi = 6.1132$ eV, $n_0 = 3$, $\xi = 10$. One can see, *e.g.* that for electron temperatures of more than 2000 K, radiative recombination starts to dominate over three-particle recombination rapidly for $n_e < 10^{22}$ m^{-3}.

2.3.3 (Local) Thermal Equilibrium

In complete *Thermal Equilibrium (TE)* the occupation of all species is according to Saha- and Boltzmann distributions. Furthermore, the particle velocity distributions are Maxwellian:

$$f_v(\vec{v}) = \sqrt{\left(\frac{m}{2\pi k_B T}\right)^3} \exp\left(-\frac{m|\vec{v}|^2}{2k_B T}\right), \tag{2.44}$$

and the radiation intensity[1] is at the black body level, given by Planck's law:

$$B_\nu(\nu) = \frac{2h\nu^3}{c^2}\frac{1}{\exp(h\nu/k_B T) - 1} \quad \text{or} \quad B_\lambda(\lambda) = \frac{2hc^2}{\lambda^5}\frac{1}{\exp(hc/\lambda k_B T) - 1}. \tag{2.45}$$

All these distribution functions are completely determined by a single temperature. Complete thermal equilibrium requires high collision rates and complete radiation trapping, which is approached only in stellar interiors and never achieved in laboratory plasmas. Less restrictive is *Local Thermodynamic Equilibrium (LTE)* in which the radiation intensity distribution is not necessarily thermal but the Boltzmann, Saha, and Maxwell distributions still hold. In LTE the temperature is allowed to vary over a spatial scale that is large with respect to the mean free path of the particles: $|\nabla T/T| \gg \lambda_{\text{mfp}}$ and radiation can escape.

With decreasing collision rate it often occurs that the electron-, ion- and/or neutral temperatures in a plasma become different. The reason for this is that energy gain (*e.g.* through Ohmic heating) and loss (*e.g.* through radiation) rates for the different particles are usually different [13]. The energy transfer rate for collisions between like particles is much higher than that between particles of different mass. For example, the rate for ion-ion collisions is a factor $> \sqrt{m_p/m_e} \approx 43$ higher than that for ion-electron collisions; for electron-electron collisions, this

[1] In this report both I_λ [Wm^{-2}nm^{-1}Sr^{-1}] and I_ν [Wm^{-2}Hz^{-1}Sr^{-1}] are referred to as intensity. Moreover the term intensity and symbol I_λ [ph s^{-1}m^{-2}nm^{-1}] is also used in some of the experimental results in this report to describe the number of photons per unit of surface and interval of wavelength. In the latter definition the values are integrated over the whole (4π) solid angle.

factor is $> m_p/m_e \approx 1836$. This causes the velocity distributions within a class of particles to thermalize relatively fast, so that one can speak of $T_\mathrm{e}, T_\mathrm{i}, T_\mathrm{g}$, etc., whereas the kinetic energy distribution of the system as a whole is no longer according to Maxwell-Boltzmann.

Although this situation strictly contradicts the conditions for LTE, one often ignores this and still speaks of LTE, since the Saha and Boltzmann distributions are determined by the electron temperature T_e only.

2.4 Non-thermal populations

Sustaining LTE requires an (electron) density that is high enough for collisional processes to dominate the transitions between all energy levels in an atomic system. The state occupation distributions will then not be affected by the escaping radiation. A rule-of-thumb condition for collisional transitions to dominate over radiative (McWhirter 1965) may be written [10]:

$$n_e \gg 10^{19}\sqrt{T_\mathrm{e}}(\Delta E)^3 \ [\mathrm{m}^{-3}], \tag{2.46}$$

where T_e and ΔE are the electron temperature and energy level difference (both in eV). In an atomic system, this condition is satisfied first in the higher levels, where the energy differences ΔE are small. An example: for the lower lying electronic states of Ca I with typical ΔE ranging from 0.3 eV to a few eV (not including transitions between substates of the same multiplet) in a plasma with $T_e < 1$ eV, the critical electron densities are in the order of 10^{17}–$10^{21}\mathrm{m}^{-3}$.

2.4.1 pLSE and coronal equilibrium

The energy differences between electronic states and the energy differences between the electronic states and the ion ground state both converges to 0 near the series limit (with increasing principal quantum number). Thus, there is always a level, the *collision limit*, above which the states are in Boltzmann equilibrium with each other and Saha equilibrium with the ion ground state. If this energy level is significantly below the ionization energy, this situation is called *partial Local Saha Equilibrium (pLSE)*.

In the limit of very low electron densities, another equilibrium situation can occur, which is called *coronal equilibrium*, since it is applicable in the solar corona. A requirement for coronal equilibrium is that the plasma is *optically thin* (see section 2.5.1), so that nearly all photons escape the plasma. In this case all upward processes are collisional, since absorption is negligible and all downward transitions are radiative, since the electron density is low. The excitation/deexcitation and ionization/recombination balances now take a new form.

Coronal balances

Depopulation of excited states is dominated by spontaneous emission with coefficient A_{qp}. Since at low electron densities the excitation rates will be low compared to A_{qp}, most particles will be in their ground state (metastable states may form an exception). Electron impact will thus be dominated by transitions from the ground state, with rate coefficient $K_{1q}^\mathrm{exc} \equiv \langle \sigma_{1q}^\mathrm{exc} v \rangle$. The coronal balance for the excited states then becomes:

$$n_q = \frac{n_1 n_\mathrm{e} K_{1q}^\mathrm{exc}}{\sum_p A_{qp}}. \tag{2.47}$$

Collisional ionization will be balanced by radiative recombination, which will be the dominant recombination process at low electron densities. Again only the ground state is determining the ionization rate because of its dominant population. The ionization stage balance thus becomes:

$$n_{+,0} = \frac{n_{0,0} n_\mathrm{e} K_{0+}^\mathrm{ion}}{n_\mathrm{e} \sum_p K_{+p}^\mathrm{rr}} = \frac{n_{0,0} K_{0+}^\mathrm{ion}}{K_{+,\mathrm{tot}}^\mathrm{rr}}, \tag{2.48}$$

where $n_{0,0} \approx n_0$ and $n_{+,0} \approx n_+$ are the neutral and ion ground state density respectively; K^{ion}_{0+} is the ionization rate coefficient for the ground state, *e.g.* given by equation (2.24) and K^{rr}_{+p} is the radiative recombination rate coefficient to level p and K^{rr} is the rate coefficient for the total radiative recombination to all levels, which can be approximated using equation (2.29). An example is shown in figure 2.1, where equation (2.48) has been used to calculate the ionization degree in calcium in coronal equilibrium (dashed black line).

In practice, the coronal balance will never be applicable to all energy levels. There will always be energy levels high in the system (above the collision limit) that are in pLTE with the ion ground state.

2.4.2 Collisional radiative models

In situations where neither corona nor LTE are valid (usually at an intermediate electron density), the atomic state distribution function (*i.e.* the population of all energy levels in an atom) can be calculated by equating the rates of all processes leading increase or decrease of the population of every state in the system. This is done in a collisional radiative model. An example of a collisional radiative model for atomic calcium will be presented in chapter 4.

2.5 Radiation

Several processes can lead to the production of radiation in a plasma. In this work, only radiation originating from transitions between bound atomic or molecular states, *i.e.* atomic line and molecular band emission, is considered. The production of radiation in the plasma is described by the *emission coefficient* ϵ_λ [$\text{Wm}^{-3}\text{nm}^{-1}\text{Sr}^{-1}$]. Radiation losses, on the other hand, can be described by the *absorption coefficient* κ_λ [m^{-1}]. The absorption coefficient is defined by the relation $\text{d}I_\lambda = -\kappa_\lambda I_\lambda \text{d}l$, where I_λ is the intensity I_λ [$\text{Wm}^{-2}\text{nm}^{-1}\text{Sr}^{-1}$] of a beam traveling through the plasma over distance $\text{d}l$ and $\text{d}I_\lambda$ is the change in intensity *due to absorption only*. In general the absorption coefficient includes both true absorption processes (such as photo ionization) as well as scattering processes. In this report however, only true absorption for atomic line transitions (photo excitation, between bound states) is considered.

2.5.1 Radiation transport

When a beam of light with intensity I_λ passes through a slab of plasma of thickness $\text{d}l$, the intensity changes by an amount:

$$\text{d}I_\lambda = \epsilon_\lambda \text{d}l - I_\lambda \kappa_\lambda \text{d}l. \tag{2.49}$$

Using $\kappa_\lambda \text{d}l \equiv d\tau_\lambda$ the *optical thickness* is defined as:

$$\tau_\lambda = \tau_\lambda(l) = \int_0^l \kappa_\lambda \text{d}l'. \tag{2.50}$$

By dividing equation (2.49) through $\text{d}\tau_\lambda$, the one-dimensional radiation transport equation is obtained:

$$\frac{\text{d}I_\lambda}{\text{d}\tau_\lambda} + I_\lambda = \frac{\epsilon_\lambda}{\kappa_\lambda} \equiv S_\lambda, \tag{2.51}$$

where S_λ is called the *source function*. In case of thermodynamic equilibrium, it is equal to the black body intensity, given by Planck's law: $S_\lambda = B_\lambda$, equation (2.45). For atomic transitions $S_\lambda = B_\lambda$ is valid as long as the states are occupied according to Boltzmann (thus in LTE) [13]. Solving equation (2.51) using constant B_λ (*i.e.* at constant temperature) using the boundary condition $I_\lambda(l = 0) = 0$ then simply gives:

$$I_\lambda(l) = B_\lambda(1 - e^{-\tau_\lambda}). \tag{2.52}$$

Two extreme cases are:

$$I_\lambda(l) = B_\lambda \quad \text{for} \quad \tau_\lambda \gg 1 \quad \text{(optically thick)} \tag{2.53}$$

$$I_\lambda(l) = \tau_\lambda B_\lambda = \epsilon_\lambda l \quad \text{for} \quad \tau_\lambda \ll 1 \quad \text{(optically thin).} \tag{2.54}$$

Another special case that is interesting for practical purposes is that of two adjacent layers of plasma with different temperatures T_1 and T_2. When LTE occupation is assumed again and layer 1 is behind layer 2 with $T_1 > T_2$ the solution to the radiation transport equation becomes:

$$I_\lambda(l) = B_\lambda(T_2)(1 - e^{-\tau_{\lambda,2}}) + B_\lambda(T_1)(1 - e^{-\tau_{\lambda,1}})e^{-\tau_{\lambda,2}}. \tag{2.55}$$

For an atomic transition with lower level p, upper level q, transition wavelength λ_0 and Einstein coefficient for spontaneous emission A_{qp} the emission coefficients is given by [13]:

$$\epsilon_\lambda = n_q A_{qp} \frac{hc}{4\pi\lambda_0} P(\lambda) \equiv \epsilon_{qp} P(\lambda), \tag{2.56}$$

where ϵ_{qp} is the wavelength integrated emission coefficient and $P(\lambda)$ is the normalized lineshape function: $\int P(\lambda)\mathrm{d}\lambda = 1$. The lineshape function may be approximated by a Gaussian or another distribution, determined by the dominant line broadening mechanism. These mechanisms will be discussed in the following section 2.5.2. The absorption coefficient (only true absorption) is given by the Ladenburg relation [13]:

$$\kappa_\lambda = n_p \frac{g_q}{g_p} \frac{\lambda_0^4}{8\pi c} A_{qp} P(\lambda) \equiv \kappa_{pq} P(\lambda), \tag{2.57}$$

where κ_{pq} is the line integrated absorption coefficient.

Escape factors

The last concept that will be introduced in this section is that of the *escape factor*. The discussion here is based on that in [24]. A general introduction to the subject is written by Irons [25]. The radiation transport equation (2.51) is considered again, but now for a more general case where the emissivity $\epsilon_\lambda = \epsilon_\lambda(\vec{r}, \lambda)$ is no longer uniform (*e.g.* due to zones with different temperatures). For simplicity the absorption constant is still assumed to be (almost) uniform, *i.e.* replaced by its average value $\overline{\kappa_\lambda}(\lambda)$. In praxis the latter means that a constant absorber density is assumed, which is often justified for ground state (neutral) absorbers. Also the emission and absorption line shape functions $P(\lambda)$ are assumed to be the same and spatially constant. The solution of (2.51), again with $I_\lambda(l = 0) = 0$, is:

$$I_\lambda(l, \lambda) = \int_0^l \epsilon_\lambda(l', \lambda) \exp[(l' - l)\overline{\kappa_\lambda}(\lambda)]\mathrm{d}l'. \tag{2.58}$$

The line-of-sight integrated escape factor is now defined as the ratio of this intensity and that in the optically thin case, both integrated over the line profile:

$$\begin{aligned}\Theta_\mathrm{L}(l) = \frac{\int_\mathrm{line} I_\lambda(l, \lambda)\mathrm{d}\lambda}{\int_\mathrm{line} I_\lambda^\mathrm{thin}(l, \lambda)\mathrm{d}\lambda} &= \frac{\int_0^l \int_\mathrm{line} \epsilon_\lambda(l', \lambda) \exp[(l' - l)\overline{\kappa_\lambda}(\lambda)]\mathrm{d}\lambda\mathrm{d}l'}{\int_0^l \int_\mathrm{line} \epsilon_\lambda(l', \lambda)\mathrm{d}\lambda\mathrm{d}l'} \\ &= \frac{\int_0^l \epsilon_{pq}(l') \int_\mathrm{line} P(\lambda) \exp[(l' - l)\overline{\kappa_{pq}} P(\lambda)]\mathrm{d}\lambda\mathrm{d}l'}{\int_0^l \epsilon_{pq}(l')\mathrm{d}l'}.\end{aligned} \tag{2.59}$$

The line escape factor $\Theta_\mathrm{L}(l)$ describes the escaping radiance along a given line-of-sight and can be used for spectroscopic measurements. For a spatially constant emission coefficient, it reduces to:

$$\Theta_\mathrm{L}(l) = \frac{1}{\kappa_{pq} l} \int_\mathrm{line} (1 - \exp[-l\kappa_{pq} P(\lambda)])d\lambda, \tag{2.60}$$

which is nothing but the wavelength integral of equation (2.52), divided by $\kappa_{pq} l$.

In order to calculate the change in (excited) state population due to absorption, as is done in a collisional radiative model, another type of escape factor is required. This escape factor Θ_{P} describes the total fraction of escaping radiation from one point in the plasma. For a transition with lower level p and upper level q, the effect of absorption on the population of state q can be treated as negative spontaneous emission. This gives an *effective Einstein coefficient for spontaneous emission* $A_{pq}^{\mathrm{eff}} = \Theta_{\mathrm{P}} A_{pq}$. The *population escape factor* Θ_{P} is defined as the relative difference between the emitted and absorbed line radiation power (per unit volume):

$$\Theta_{\mathrm{P}} = \frac{P_{pq}^{\mathrm{em}} - P_{pq}^{\mathrm{abs}}}{P_{pq}^{\mathrm{em}}} = 1 - \frac{P_{pq}^{\mathrm{abs}}}{P_{pq}^{\mathrm{em}}}. \tag{2.61}$$

The emitted radiation power is simply the emission coefficient integrated over all (4π) solid angles:

$$P_{pq}^{\mathrm{em}} = \int_{\Omega} \epsilon_{pq} \mathrm{d}\Omega = 4\pi \epsilon_{pq}, \tag{2.62}$$

where isotropic emission is assumed. The absorbed power, however, depends on the (local) intensity $I_\lambda(l, \lambda)$ at position l given by equation (2.58). For simplicity the middle point $l = b$ of a point symmetric plasma sphere, extending from $l = 0$ to $l = 2b$, where $\epsilon_\lambda(0) = \epsilon_\lambda(2b) = 0$, is considered. The absorbed radiation power in this case can be written:

$$P_{pq}^{\mathrm{abs}} = \int_{\Omega} \int_{\mathrm{line}} \overline{\kappa_\lambda}(\lambda) I_\lambda(l, \lambda) \mathrm{d}\lambda \mathrm{d}\Omega = \int_{\Omega} \int_{\mathrm{line}} \overline{\kappa_\lambda}(\lambda) \int_0^b \epsilon_\lambda(l, \lambda) \exp[(l-b)\overline{\kappa_\lambda}(\lambda)] \mathrm{d}l(\Omega) \mathrm{d}\lambda \mathrm{d}\Omega =$$
$$4\pi \int_{\mathrm{line}} \overline{\kappa_\lambda}(\lambda) \int_0^b \epsilon_\lambda(l, \lambda) \exp[(l-b)\overline{\kappa_\lambda}(\lambda)] \mathrm{d}l \mathrm{d}\lambda \tag{2.63}$$

Finally, the escape factor is evaluated for the special case of a uniform emission coefficient ϵ_λ. The central intensity is found (by evaluating the integral in equation (2.58)) to be:

$$I_\lambda(b) = \frac{\epsilon_\lambda}{\overline{\kappa_\lambda}} \left(1 - \exp[-\tau_\lambda]\right) \tag{2.64}$$

where $\tau_\lambda = \tau_\lambda(b) = \overline{\kappa_\lambda} b$ is the optical thickness seen from the center. The absorbed power is found by substituting $I_\lambda(b)$ into equation (2.63):

$$P_{pq}^{\mathrm{abs}}(b) = 4\pi \int_{\mathrm{line}} \epsilon_\lambda \left(1 - \exp[-\tau_\lambda]\right) \mathrm{d}\lambda \tag{2.65}$$

The population escape factor thus becomes:

$$\Theta_{\mathrm{P}}(b) = 1 - \frac{\int_{\mathrm{line}} \epsilon_\lambda \left(1 - \exp[-\tau_\lambda]\right) \mathrm{d}\lambda}{\epsilon_{pq}} = \int_{\mathrm{line}} P(\lambda) \exp[-\tau_\lambda] \mathrm{d}\lambda, \tag{2.66}$$

where the last identity, which follows directly from substituting the definition of ϵ_{pq}, shows that this population escape factor in this example only depends on the optical thickness $\tau_\lambda = \overline{\kappa_\lambda} b = \overline{\kappa_{pq}} P(\lambda) b$ and the normalized line function $P(\lambda)$.

2.5.2 Spectral line broadening by plasmas

Photons emitted during a transition between bound states do not have a perfectly defined fixed energy. Instead, their energies vary and the lines in the spectrum thus have a finite width. This spectral line broadening is due to several mechanism; some of which are very useful for plasma diagnostics. Mechanisms that are considered relevant for the experiments presented here are discussed below. Stark broadening is discussed more elaborately than other mechanisms because of its complexity and relevance for plasma density measurements.

Natural line broadening

The lifetime τ of an isolated atom in an excited quantum state is finite due to the occurrence of spontaneous transitions to a lower state. For a transition from level k to i this leads to a Lorentz shaped line profile with a full width at half maximum (FWHM) [13]:

$$w_{\text{natural}} = \frac{\lambda^2}{2\pi c}(\sum_{j<k} A_{kj} + \sum_{j<i} A_{ij}), \tag{2.67}$$

with $A_{\alpha\beta}$ the Einstein coefficient for spontaneous emission from level α to level β. The natural line width is usually in the order of 0.1 pm or less and negligible compared to other broadening mechanisms for most plasmas.

Doppler broadening

The thermal motion of the emitting particles results in Doppler broadening. This gives a Gaussian line shape with a FWHM [13]:

$$w_{\text{D}} = 2\lambda\sqrt{\frac{kT}{mc^2}} = 7.16 \cdot 10^{-7}\lambda\sqrt{T[\text{K}]/M[\text{amu}]}, \tag{2.68}$$

where T is the temperature and m the mass of the radiating atom. In the latter part of the equation T is in K and M the mass in atomic mass units.

Pressure broadening

Pressure broadening is a general term used to refer to a collection of processes in which the presence of nearby particles affects the radiation emitted by an individual particle[2]. It can be classified into two limiting cases by which this occurs [26, 9]:

- *Impact broadening:* In this extreme the emitting particle is emitting undisturbed most of the time, but occasionally a collision with another particle interrupts the emission process. The duration of the collision (interaction) is much shorter than the time between collisions. This can be considered to result in a reduced effective lifetime for the states involved in the transition. The resulting line profile is Lorentzian, like in natural broadening. The amount of broadening depends on both density and temperature perturbing species.

- *Quasistatic broadening:* The presence of other particles that are interacting with the emitting particle shifts the energy levels in the emitting particle, thereby altering the wavelength of the emitted radiation. For this approximation to hold, the interaction time should be much longer than the effective lifetime of the excited states involved in the transition. The form of the line profile is determined by the functional form of the perturbing interaction potential with respect to the distance between the interacting particles. There may also be a shift of the line center (*e.g.* Stark shift), due to a different sensitivity of the upper and lower state to the interaction potential. This effect also depends on density of the perturbing species, but is less sensitive to temperature.

Due to the difference in velocities of the ions/neutrals and electrons, electron broadening is usually best described in the impact approximation, whereas the quasistatic broadening is more applicable to ions. Pressure broadening may also be classified by the nature of the perturbing force (particle). This approach will be followed below.

[2]Note that some authors exclude Stark broadening from pressure broadening. Here, the term is used to refer to the whole collection of broadening mechanisms, due to perturbing interactions, including Stark broadening.

Van der Waals broadening

Van der Waals broadening occurs when the emitting particle is being perturbed by Van der Waals forces, *i.e.* from the interaction between the dipole of the emitting atom and the induced dipole of a nearby neutral. Because of the weaker interaction potential ($\sim r^{-6}$), as compared to Coulomb forces, this effect is usually only relevant for plasmas with a low ionization degree. Van der Waals broadening theories lead to complex line profiles, that will not be discussed here (see *e.g.* [26]). However these can usually be approximated well with a Lorentz profile. The width increases linearly with the neutral density. An estimate of the proportionality constant follows.

The width $w_{\rm vdw}$ (FWHM) due to Van der Waals broadening by neutrals with density $n_{\rm n}$ and temperature $T_{\rm g}$ can be estimated using a formulae given by Griem [27] or Konjevic [28]:

$$w_{\rm vdw}\ [\rm nm] = 8.18 \cdot 10^{-25} \lambda^2 (\bar{\alpha}\overline{R^2})^{2/5} (T_{\rm g}/\mu)^{3/10} n_{\rm n}, \tag{2.69}$$

with $n_{\rm n}$ in $\rm m^{-3}$ and λ in nm. In this expression $\overline{R^2} = \overline{R_{\rm u}^2} - \overline{R_{\rm l}^2}$ is the difference of the squares of the coordinate vectors of the upper and lower level in a_0 units, μ is the reduced mass of the atom and perturber in a.m.u. and $\bar{\alpha}$ is the mean polarizability of the neutral perturber in $\rm cm^3$ (mind units), as tabulated *e.g.* in ref. [29]. $\overline{R_{\rm u}^2}$ and $\overline{R_{\rm l}^2}$ are calculated from:

$$\overline{R_j^2} = n_j^{*2}(5n_j^{*2} + 1 - 3l_j(l_j+1))/2, \tag{2.70}$$

where n_j^* is the effective quantum number of level j defined by:

$$n_j^{*2} = E_{\rm H}/(E_{\rm ion} - E_j), \tag{2.71}$$

with $E_{\rm ion}$ the ionization energy of the perturbed element, $E_{\rm H}$13.5984 eV that of hydrogen and E_j the energy of the upper or lower level. Van der Waals broadening results in a red shift that is about two third of the width: $d_{\rm vdw} = \frac{2}{3} w_{\rm vdw}$ [28].

Stark broadening

Stark broadening is the form of pressure broadening arising from perturbations by charged particles, *i.e.* ions and electrons, in the vicinity of a radiating atom or ion. The most complete treatment of Stark broadening is given by Griem [30, 27, 31]. Detailed calculations of Stark broadening are very complicated and generally result in complex formulae for line profiles. A distinction must be made between lines of hydrogen (and hydrogen like states in some other elements) and those of other elements, which show different behavior in the presence of an electric field E. In hydrogen the Stark effect is linear: $\Delta\nu \propto E$, whereas for non-hydrogenic atoms and ions there is a quadratic and much smaller stark effect: $\Delta\nu \propto E^2$.

Hydrogen Stark broadening Via simple arguments (nearest neighbor approximation, see *e.g.* [10]) one can show that for the intensity in the wings of the lines, determined by quasistatic ion broadening, is $I_\lambda \propto (\Delta\lambda)^{-5/2}$, as opposed to $I_\lambda \propto (\Delta\lambda)^{-2}$ for a Lorentz profile. The FWHM of hydrogen lines can approximated by[10]:

$$w_{\rm S} = 2.50 \cdot 10^{-9} \alpha_{1/2} n_{\rm e}^{2/3}, \tag{2.72}$$

where $n_{\rm e}$ is the electron density. The half-width parameter $\alpha_{1/2}$ for the $\rm H_\beta$ line at 486.1 nm, widely used for plasma diagnostics is approximately 0.08; it depends only weakly on temperature. However, more convenient and accurate are tabulations of $w_{\rm S}$ (for a wide range of electron temperatures and densities) based on more advanced theories, *e.g.* in [32]. When more accuracy is required, tabulated line profiles [33, 34] can be used for fitting the whole spectral line.

Non-hydrogen atomic Stark broadening Like in the case of hydrogen, precise calculations of the line profile are very complex (if not impossible). Quasistatic ion broadening due to the quadratic Stark effect results in a wing intensity decreasing as $I_\lambda \propto (\Delta\lambda)^{-7/4}$. In general, the line profile is affected by a combination of electron impact broadening and a smaller contribution due to quasistatic ion broadening effects. The latter usually also introduces a shift that is smeared out by the distribution of microfields in the plasma, resulting in asymmetry. The fraction of broadening due to ions can be described by the *ion broadening parameter* $A(T_\mathrm{e})$, tabulated by Griem [31] for many atomic species. For ionic lines the quasistatic ion contribution is smaller than for atoms so that it is often neglected. For Stark broadening of ionic lines the reader is referred to literature [31, 28].

Assuming only singly charged ions in a plasma, thus $n_\mathrm{e} = n_\mathrm{i}$, the total broadening w_S (FWHM) and shift d_S for atomic lines according to Griem [31] may can be written as:

$$w_\mathrm{S} = 2w_\mathrm{e}(T_\mathrm{e})[1 + 1.75 \cdot 10^{-4} n_\mathrm{e}^{1/4} A(T_\mathrm{e})(1 - 0.068 n_\mathrm{e}^{1/6} T_\mathrm{e}^{-1/2})]10^{-16} n_\mathrm{e} \tag{2.73}$$

$$d_\mathrm{S} = [d_\mathrm{e}(T_\mathrm{e}) \pm 2.0 \cdot 10^{-4} n_\mathrm{e}^{1/4} A(T_\mathrm{e}) w_\mathrm{e}(T_\mathrm{e})(1 - 0.068 n_\mathrm{e}^{1/6} T_\mathrm{e}^{-1/2})]10^{-16} n_\mathrm{e}. \tag{2.74}$$

In this expression n_e is the electron density in cm^{-3}, T_e is in K and w_e and d_e are reference half-width at half maximum (HWHM, the notation and units used by the reference sources is followed here and in the following paragraphs) and shift respectively, due to collisions with electrons. These parameters are tabulated for a standard density of $n_\mathrm{e} = 10^{16}$ cm^{-3} [31]. The sign of the ion quadratic contribution to the shift in equation (2.74) is equal to that of the low-temperature limit of d_e.

There are some criteria for the applicability of equations (2.73) and (2.74), namely:

$$R = 8.99 \cdot 10^{-2} n_\mathrm{i}^{1/6} T_\mathrm{e} \leq 0.8 \quad \text{and} \tag{2.75}$$

$$0.05 \leq A(T_\mathrm{e}) n_\mathrm{e}^{1/4} 10^{-4} \leq 0.5 \tag{2.76}$$

with R the *Debye shielding parameter*, equal to the ratio of the mean inter-ion distance $(n_\mathrm{e} 4\pi/3)^{1/3}$ and the Debye radius $\lambda_\mathrm{D}/\sqrt{4\pi}$ [30]. Table 2.1 contains examples of Stark broadening parameters w_e, d_e, and A calculated using Griem's approach for a number of spectral lines and various electron temperatures.

Other authors (*e.g.* Dimitrijević and Sahal-Bréchot, see [35] and the references therein) use the impact approximation for broadening due to both electrons and ions. The width and shift can then be written as:

$$w_\mathrm{S} = [2w_\mathrm{e}(T_\mathrm{e}) n_\mathrm{e} + 2w_\mathrm{i}(T_\mathrm{i}) n_\mathrm{i}]10^{-16} \tag{2.77}$$

$$d_\mathrm{S} = [d_\mathrm{e}(T_\mathrm{e}) n_\mathrm{e} \pm d_\mathrm{i}(T_\mathrm{i}) n_\mathrm{i}]10^{-16} \tag{2.78}$$

where $2w_\mathrm{e}$, $2w_\mathrm{i}$ and d_e and d_i are electron and ion impact FWHM and shifts respectively at $n_{e,i} = 10^{16}$ cm^{-3} [35]; n_i and T_i are the ion density and temperature respectively. The sign of the ion contribution to the shift in equation (2.78) depends on the ion species and is given in the same tables. Restrictions to the applicability of equations (2.77) and (2.78) can also be found in [35] and the references therein. Examples of Stark broadening parameters determined using this method can be found in table 2.2.

In general, an accuracy of 20% at best can be expected from theoretically determined Stark widths, of non-hydrogenic lines. The expected accuracy in the shifts is worse [36].

Finally, there are collections of experimental data on Stark broadening of many spectral lines. The most complete and well reviewed are those by Konjević and co-workers [36, 37, 38]. Listed are measured widths w_m (FWHM) and shifts d_m at a reference density n_Ref. These authors also make comparisons with theoretical values and introduce accuracy codes. The actual Stark width and Shift then follow from:

$$w_\mathrm{S} = w_\mathrm{m}(T_\mathrm{e}) n_\mathrm{e} / n_\mathrm{Ref} \tag{2.79}$$

$$d_\mathrm{S} = d_\mathrm{m}(T_\mathrm{e}) n_\mathrm{e} / n_\mathrm{Ref}. \tag{2.80}$$

Some examples of experimentally determined Stark broadening parameters are listed in table 2.3. In general the accuracy of experimentally determined widths is much better than that of the shifts. In cases where both are determined accurately, the compliance with theory is generally better for the widths [36]. Also shifts are more temperature dependent, making them less suitable for density measurements.

Table 2.1: *Stark parameters derived theoretically by Griem [31] using impact approximation for broadening by electrons and quasistatic approximation for the ion contribution. Listed are widths w_e (HWHM), shifts d_e due to electron perturbers at a density of 10^{22} m^{-3} and electron temperature T_e, and parameter A for the quasistatic ion contribution to the width, see equations (2.73) and (2.74).*

Element	States	Terms	λ_0 [nm]	T_e [K]	w_e [pm]	d_e [pm]	A
Ca I	4s–4p	^{1}S–^{1}P	422.673	5000	0.484	0.386	0.016
				10000	0.630	0.380	0.013
	4p–5d	^{1}P–^{1}D	518.885	5000	31.7	-22.5	0.078
				10000	39.7	-18.8	0.066

Table 2.2: *Stark parameters derived theoretically using impact approximation for both electron and ion contributions by Dimitrijević and Sahal-Bréchot [35]. Listed are widths w_e, w_p (FWHM) and shifts d_e d_p due to electron and proton perturbers respectively at a perturber density of 10^{22} m^{-3} and perturber temperature T.*

Element	States	Terms	λ_0 [nm]	T [K]	w_e [pm]	d_e [pm]	w_p [pm]	d_p [pm]	Ref.
Ca II	4s–4p	^{2}S–^{2}P	393.367	5000	2.96	-0.526	0.108	-0.0372	[39]
				10000	2.28	-0.425	0.174	-0.0663	[39]
Li I	2p–3d	^{2}P–^{2}D	610.354	2500	33.9	-14.9	7.41	-6.45	[40]
				5000	36.8	-9.89	8.19	7.25	[40]
				10000	37.5	-5.52	9.09	8.15	[40]
	2p–4d	^{2}P–^{2}D	460.283	2500	304	9.41	138	123	[40]
				5000	276	2.64	159	141	[40]
				10000	245	-3.60	182	164	[40]

Other broadening mechanisms

Resonance broadening Resonance broadening is another type of pressure broadening that occurs when the perturbing particle is of the same type as the emitting particle. This introduces the possibility of an energy exchange process. This broadening effect is described by a Lorentzian profile in both the impact and the quasistatic case and only relevant resonance lines when the (absolute and relative) concentration of the emitting element is high.

Opacity broadening This is a non-local effect, that is a consequence of the absorption of radiation, as discussed in section 2.5.1. Lines are broadened because photons at the line wings have a smaller reabsorption probability than photons at the line center. The broadening effect is most important for transitions to the ground state (resonance lines), which have the highest absorber concentrations. When temperature differences (or density) gradients exist along the line of sight (*e.g.* when a hot layer of plasma is behind a cooler one) the absorption near line center may be so strong that it causes *self-reversal*, in which the intensity at the center of the line is less than in the wings.

TABLE 2.3: *Some experimentally determined Stark widths w_m (FWHM) and shifts d_m at a nominal electron density of 10^{22} m^{-3}. A positive (resp. negative) shift is towards the red (resp. blue). References to the original literature and criteria used for the accuracy estimate can be found in the collections of Konjević et al, as indicated in the last column.*

Element	States	Terms	λ_0 [nm]	T_e [K]	w_m [pm]	d_m [pm]	Error	Ref.
Ca II	4s–4p	^{2}S–^{2}P	393.367	12240	1.14	-	$< 23\%$	[37]
				13350	1.36	-	$< 23\%$	[37]
				43000	1.63	-0.80	$< 30\%$	[38]
Cu I	$3d^9 4s^2$–$3d^{10}4p$	^{2}D–^{2}P	510.324	10000	4.3	0.67	$< 50\%$	[37]
Cu I	$3d^{10}4p^2$–$3d^{10}4d$	^{2}P–^{2}D	515.324	10000	19.0	-2.7	$< 50\%$	[37]
			521.820	10000	22.0	-3.0	$< 50\%$	[37]
			522.007	10000	22.0	-3.0	$< 50\%$	[37]
Cu I	$3d^{10}4p^2$–$3d^{10}5d$	^{2}P–^{2}D	402.263	10000	43.1	19.5	$< 50\%$	[37]
			406.264	10000	41.9	17.4	$< 50\%$	[37]

Apparatus broadening This (pseudo) broadening effect is caused by the finite resolving power $R \equiv \lambda/(\Delta\lambda)$ of the measurement device (*e.g.* spectrometer) used to record the line. The apparatus profile can usually be approximated using a Gaussian. Expressions for the resolving power are given in section 2.5.3.

Combination of broadening mechanisms

Any of the aforementioned broadening mechanisms can act by itself as well as in combination. Assuming each effect is independent of other effects, the combined line profile will be the convolution of the line profiles of each mechanism. For example, a combination of a Gaussian apparatus profile and Lorentzian impact pressure broadening will yield a so called Voigt profile. As a function of their FWHM and the distance from the line center $\Delta\lambda = \lambda - \lambda_0$ these normalized line profiles are:

$$P_{\text{Lorentz}}(\Delta\lambda, w_{\text{L}}) = \frac{1}{2\pi}\frac{w_{\text{L}}}{\Delta\lambda^2 + w_{\text{L}}^2/4} \tag{2.81}$$

$$P_{\text{Gauss}}(\Delta\lambda, w_{\text{G}}) = \frac{1}{(w_{\text{G}}/2.355)\sqrt{2\pi}} \exp\left(\frac{-\Delta\lambda^2}{2(w_{\text{G}}/2.355)^2}\right) \tag{2.82}$$

$$P_{\text{Voigt}}(\Delta\lambda) = P_{\text{Gauss}}(\Delta\lambda) * P_{\text{Lorentz}}(\Delta\lambda) = \int_{-\infty}^{\infty} P_{\text{Gauss}}(\Delta\lambda) P_{\text{Lorentz}}(\Delta\lambda - \lambda')\mathrm{d}\lambda', \tag{2.83}$$

where $2.335 \approx 2\sqrt{2\ln 2} = w_{\text{G}}/\sigma_{\text{G}}$ arises from the use of the FWHM instead of the standard deviation σ_{G} for the Gauss profile. For numerical applications, the Voigt profile above can be approximated by a so-called pseudo-Voigt profile, to avoid calculation of the convolution [41]:

$$P_{\text{PsdVoigt}}(\Delta\lambda) = (1-\eta)P_{\text{Gauss}}(\Delta\lambda, w_{\text{V}}) + \eta P_{\text{Lorentz}}(\Delta\lambda, w_{\text{V}}), \tag{2.84}$$

with:

$$w_{\text{V}} = \left(w_{\text{G}}^5 + 2.69269 w_{\text{G}}^4 w_{\text{L}} + 2.42843 w_{\text{G}}^3 w_{\text{L}}^2 + 4.47163 w_{\text{G}}^2 w_{\text{L}}^3 + 0.07842 w_{\text{G}} w_{\text{L}}^4 + w_{\text{L}}^5\right)^{1/5} \tag{2.85}$$

$$\eta = 1.36603(w_{\text{L}}/w_{\text{V}}) - 0.47719(w_{\text{L}}/w_{\text{V}})^2 + 0.11116(w_{\text{L}}/w_{\text{V}})^3, \tag{2.86}$$

the Voigt FWHM and mixing parameter respectively. Evaluated examples of these line profiles are given in figure 2.4.

Regarding the combination of broadening mechanisms it is noted that the convolution of two Gaussian with widths w_{G1} and w_{G2} results in another Gaussian with resulting width $w_{\text{GR}} = \sqrt{w_{\text{G1}}^2 + w_{\text{G2}}^2}$. The widths of two Lorentz-broadening mechanisms acting simultaneously can simply be added to obtain that of the resulting Lorentz curve: $w_{\text{LR}} = w_{\text{L1}} + w_{\text{L2}}$.

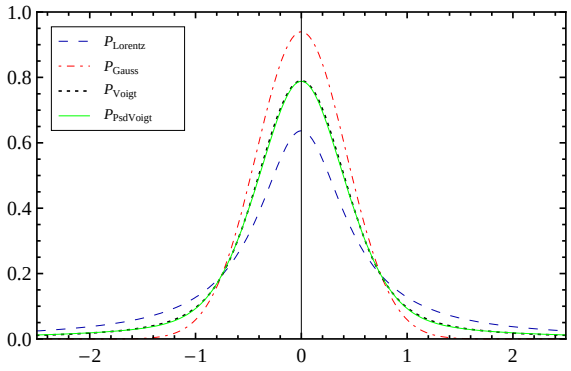

Figure 2.4: *Normalized Lorentz, Gauss, Voigt and pseudo-Voigt profiles, all with a FWHM of 1. Both Voigt profiles have* $w_{\text{L}} \approx 0.422$ *and* $w_{\text{G}} \approx 0.753$*, giving a mixing parameter* $\eta = 0.5$ *for the Pseudo Voigt case. For the convoluted Voigt profile, numeric integration from* $-150w_{\text{L}}$ *to* $150w_{\text{L}}$ *was used.*

2.5.3 Spectroscopy basics

Several spectrometers of different type were used in experiments, to analyze the emission from the plasmoid. This section does not discuss them in full detail. Instead, a short introduction to the basic equations describing a reflection gratin spectrometer and expressions for the resolving power are given. The concept of an échelle spectrometer is introduced at the end.

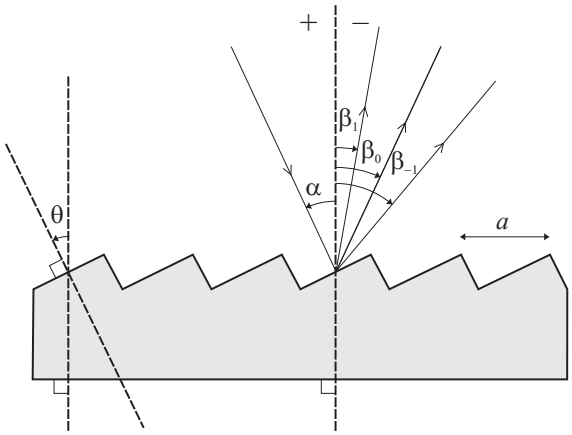

Figure 2.5: *Blazed reflection grating.* α *is the incident beam angle,* β_m *is the angle of the diffracted beam of order* m*.* θ *is the blaze angle and* a *is the grating constant or groove separation. Angles are measured with respect to the grating normal, where counter clockwise is positive.*

A reflection grating can be used as the dispersive element in a spectrometer, as shown schematically in figure 2.5. The grating equation, describing the condition for constructive interference, is [42]:

$$\sin\alpha + \sin\beta = \frac{m\lambda}{a} \tag{2.87}$$

with α and β the angles of the incident and diffracted beam respectively, m the order of diffraction, a the grating constant and λ the wavelength. Usually the grating is mounted on a rotation stage and the collimator-camera or spectrograph angle $\phi = \alpha - \beta$ is fixed by the design. Using this definition the grating equation can be rewritten as:

$$\sin(\phi + \beta) + \sin\beta = \frac{m\lambda}{a} \tag{2.88}$$

The angular dispersion is found by differentiating with respect to λ:

$$\frac{d\beta}{d\lambda} = \frac{m}{a\cos\beta}. \tag{2.89}$$

When a photographic plate (or CCD) is used in the focal plane of a lens of focal length f_2 to record the spectrum, the spread of wavelength on the plate can be described in terms of a linear

dispersion $\frac{dx}{d\lambda}$, where x is measured along the plate:

$$\frac{dx}{d\lambda} = f_2 \frac{d\beta}{d\lambda} = \frac{f_2 m}{a \cos\beta}. \tag{2.90}$$

Assuming the light covers the entire width W of the grating the theoretical (spectral) resolving power R^* is determined by the Rayleigh criterion and is given by:

$$R^* \equiv \lambda/(\Delta\lambda)_{min} = mN, \tag{2.91}$$

where $N = W/a$ is the number of rulings in the grating.

However, in practice the resolving power is limited more by the finite width of the image of the slit, s, projected on the detector, s' [43]. When a collimator lens of focal length f_1 and diameter D_1 is used with the previously mentioned camera lens with f_2 and D_2, the invariance of étendu between spectrograph slit and camera can be used to express s' in terms of s as:

$$s' = s \frac{F_2}{F_1}. \tag{2.92}$$

Here, $F_i = f_i/D_i$ are the collimator and camera focal ratios for $i = 1, 2$ respectively. The wavelength spread over the width of the image of the slit is thus (equation (2.90)):

$$\Delta\lambda_s = s' \frac{d\lambda}{dx} = s \frac{F_2}{F_1} \frac{a \cos\beta}{f_2 m} = \frac{sa \cos\beta}{F_1 m D_2}. \tag{2.93}$$

Assuming the grating is large enough, the width of the intersection of the plane of the grating and the collimated beam is given by $W = D_2/\cos\beta$ and thus $\Delta\lambda_s$ can also be expressed as:

$$\Delta\lambda_s = \frac{sa}{mWF_1}. \tag{2.94}$$

This is the spectral resolution determined by the width of the slit. The resolving power R of the spectrograph is thus

$$R \equiv \lambda/\Delta\lambda_s = \frac{\lambda m W F_1}{sa}. \tag{2.95}$$

For a normal grating the zeroth order or specular reflection has the highest intensity. To shift the peak of the intensity envelope or blaze function to a higher order, the facets of the grating can be tilted at an angle θ, the blaze angle, to the plane of the grating, as is the situation in figure 2.5. The maximum occurs for simple reflection from the facets at

$$\alpha - \beta = 2\theta, \tag{2.96}$$

the *blaze condition*. Using the identity $\sin x + \sin y = 2\sin(\frac{x+y}{2})\cos(\frac{x-y}{2})$ and (2.96) the grating equation at the blaze condition can be rewritten as:

$$2\sin\theta\cos(\frac{\phi}{2}) = \frac{m\lambda_B}{a}, \tag{2.97}$$

with ϕ again the spectrograph angle. Finally, two limitations to the useful wavelength range of the spectrograph are mentioned. The *free spectral range*, or the range of wavelengths that may be measured without overlap of different orders is given by [42]:

$$\Delta\lambda_{\mathrm{FSR}} = \frac{\lambda_m}{m}. \tag{2.98}$$

Also, for a blazed grating the efficiency decreases according to the blaze function when moving away from the blaze wavelength λ_B. An equivalent wavelength range is found for large m when

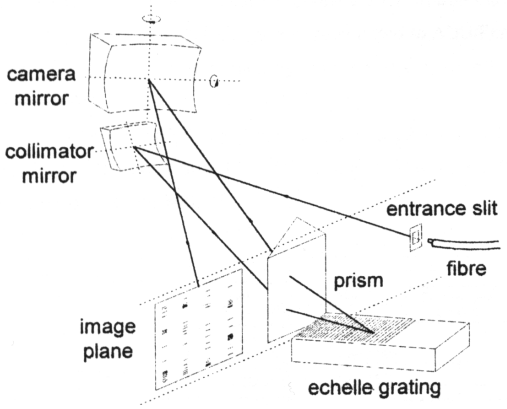

Figure 2.6: *Optical design of an échelle spectrometer.*

considering the wavelengths at which the grating efficiency drops to 40.5% of the peak intensity [43], the *blaze efficiency range*:

$$\Delta\lambda_{\text{eff}} = \frac{2m\lambda_B}{2m-1} - \frac{2m\lambda_B}{2m+1} \approx \frac{\lambda_B}{m}. \tag{2.99}$$

A special type of reflection grating spectrometer is the échelle spectrometer. It uses a (blazed) échelle grating, which is optimized for high order diffractions, under a flat angle of incidence resulting in a high spectral resolution at a relatively low number of grooves per mm. Échelle gratings are also used in 'normal' spectrometers (in combination with a narrow band filter) when a smaller spectral range is sufficient. In an échelle spectrometer however, this grating is used in combination with a second dispersing element, *e.g.* a quartz prism, placed in front of the grating. A typical optical design of this kind is sketched in figure 2.6. The échelle grating produces up to 100 overlapping diffraction orders. The quartz prism then separates these by splitting them perpendicular to the direction of the spectrum. A CCD camera records the many diffraction orders simultaneously as closely packed but separated parallel rows, of usually only a few pixels height. A big advantage of an échelle spectrometer is that it combines a high resolving power with a large spectral range. Also, it can be built compact and with no moving parts.

2.6 Molecules in plasmas

Besides atoms and ions, molecules are also present in many plasmas and contribute to the emission by means of molecular bands, on which the atomic lines are often superimposed. In the following section the processes leading to the production and destruction of molecules will be discussed shortly, from a thermodynamical viewpoint. The energy level structure and emission of diatomic molecules will be discussed afterwards. This particular class of molecules produces (in many cases well known) emission bands that can be used for plasma diagnostics purposes. The OH molecule is taken as an example, as it was present in the plasmoid spectra. Analyzing the emission from diatomic molecules can give information not only on the molecules themselves, but also on general plasma parameters such as the gas temperature.

2.6.1 Chemical equilibrium

The production and loss of molecules in a plasma is governed by chemical reactions. Exothermal reactions supply heat to the plasma, whereas endothermal reactions can be induced thermally or under the influence of (usually more energetic) charge carriers in the plasma. Examples of the processes in the latter category are electron impact dissociation, or dissociative recombination.

These chemical processes will not be discussed in detail. However, in analogy to the Saha equation for (atomic) ionization and recombination, an equation can be derived for the concentrations in chemical equilibrium. The equilibrium concentrations determine to which extent a reaction will take place. It is important to note however that these thermodynamical equilibrium equations do not give any information on the rate at which reactions take place. Though gas phase reactions are typically fast, equilibration times may be much longer than for ionization/recombination. For many reactions, temperature dependent rate coefficients, which can give an estimate of the time needed to reach equilibrium, can be found in literature [44].

A reaction of the following type is considered:

$$\alpha A + \beta B \leftrightarrows \gamma C + \delta D, \tag{2.100}$$

where A, B, C, D are different molecules and α, β, etc., the stoichiometric coefficients, are integer numbers ≥ 0.

Assuming the reaction is carried out under constant pressure and temperature conditions, equilibrium is attained when the Gibbs energy of the system is at its minimum value. The change in the Gibbs energy then is equal to the difference between the chemical potentials of the products and those of the reactants [45, 46]. Therefore, the sum of chemical potentials of the reactants must be equal to that of the products:

$$\alpha\mu_{\mathrm{A}} + \beta\mu_{\mathrm{B}} = \gamma\mu_{\mathrm{C}} + \delta\mu_{\mathrm{D}}. \tag{2.101}$$

At standard temperature T_0 (298.15 K=25 °C) and pressure p_0 (10^5 Pa) the chemical potentials are equal to the *standard molar Gibbs free energy of formation* $G_{\mathrm{f}}^{\ominus}(T_0)$:

$$\mu^{\ominus}(T_0) = G_{\mathrm{f}}^{\ominus}(T_0) = H_{\mathrm{f}}^{\ominus}(T_0) - T_0 S_{\mathrm{m}}^{\ominus}(T_0), \tag{2.102}$$

where the last equation introduces the *standard molar formation enthalpy* $H_{\mathrm{f}}^{\ominus}(T_0)$ and *standard molar entropy* $S_{\mathrm{m}}^{\ominus}(T_0)$. Values of $G_{\mathrm{f}}^{\ominus}(T_0)$, $H_{\mathrm{f}}^{\ominus}(T_0)$ and/or $S_{\mathrm{m}}^{\ominus}(T_0)$ for common chemical substances can be found in literature reference tables, such as *e.g.* in [44, 45]. The superscript $^{\ominus}$ indicates standard pressure. At different temperature and pressure the chemical potential is given by [45]:

$$\mu(p,T) = G_{\mathrm{f}}^{\ominus}(T_0) + (T - T_0)\left[C_p - S_{\mathrm{m}}^{\ominus}(T_0)\right] - C_p T \ln(\frac{T}{T_0}) + RT \ln(\frac{p}{p^{\ominus}}), \tag{2.103}$$

where $V = RT/p$ was used to eliminate the volume. Strictly, the latter equation is only valid for (ideal) gas phase substances. For a mixture of perfect gases with densities N_j, p is replaced by the partial pressure of each component p_j or in terms of mole fractions: $x_j p$, where $x_j = N_j / \sum_i N_i$:

$$\mu_j^{\ominus}(T) = G_{\mathrm{f}}^{\ominus}(T_0) + (T - T_0)\left[C_{p,j} - S_{\mathrm{m},j}^{\ominus}(T_0)\right] - C_{p,j} T \ln(\frac{T}{T_0}) + RT \ln(\frac{x_j p}{p^{\ominus}}). \tag{2.104}$$

At atmospheric (standard) pressure the last term in this equation simply equals $RT \ln x_j$. For liquids and solids, the same equation can be be applied if the last term is replaced by $\ln a_j = \ln \gamma_j x_j$, where a_j is called the activity and γ_j the activity coefficient. This will not be further discussed here. For molecules in the gas phase the molar heat capacity at constant pressure C_p depends on the number of degrees of freedom. In general,

$$C_p = C_v + R = \frac{f}{2}R + R = \frac{f+2}{2}R, \tag{2.105}$$

where C_v is the heat capacity at constant volume, and f is the number of degrees of freedom. So for atoms, with three translational degrees of freedom, $f = 3$ and $C_p = \frac{5}{2}R$, whereas for diatomic molecules two additional rotational degrees of freedom exist and $f = 5$, $C_p = \frac{7}{2}R$ and for polyatomic molecules $f = 6$, $C_p = 4R$. Here it is assumed that vibrational states are not occupied, which is only a good approximation if the temperature is not too high ($\lesssim 10^3$ K).

Equation (2.104) can be applied to find the equilibrium mole fractions of reaction (2.100) by substitution into the chemical potential balance (2.101). For compactness of notation four more quantities are defined first.

First the *reaction standard Gibbs free energy* for this reaction is defined as the difference in the standard molar Gibbs free energies of formation of the products and the reactants:

$$G^{\ominus}_{\mathrm{r}}(T_0) = \gamma G^{\ominus}_{\mathrm{f,C}}(T_0) + \delta G^{\ominus}_{\mathrm{f,D}}(T_0) - \alpha G^{\ominus}_{\mathrm{f,A}}(T_0) - \beta G^{\ominus}_{\mathrm{f,B}}(T_0). \tag{2.106}$$

Analogously, the reaction standard molar entropy is:

$$S^{\ominus}_{\mathrm{m,r}}(T_0) = \gamma S^{\ominus}_{\mathrm{m,C}}(T_0) + \delta S^{\ominus}_{\mathrm{m,D}}(T_0) - \alpha S^{\ominus}_{\mathrm{m,A}}(T_0) - \beta S^{\ominus}_{\mathrm{m,B}}(T_0), \tag{2.107}$$

and the difference in the heat capacities is written:

$$C_{p,\mathrm{r}} = \gamma C_{p,\mathrm{C}} + \delta C_{p,\mathrm{D}} - \alpha C_{p,\mathrm{A}} - \beta C_{p,\mathrm{D}}. \tag{2.108}$$

Fourthly, assuming standard pressure, the *reaction constant* is defined as:

$$K = \frac{x_{\mathrm{C}}^{\gamma} x_{\mathrm{D}}^{\delta}}{x_{\mathrm{A}}^{\alpha} x_{\mathrm{B}}^{\beta}}. \tag{2.109}$$

Substituting equation (2.104) for the chemical potentials into equation (2.101) and applying the four definitions just given, one obtains:

$$G^{\ominus}_{\mathrm{r}}(T_0) + (T - T_0)[C_{p,\mathrm{r}} - S^{\ominus}_{\mathrm{m,r}}(T_0)] - C_{p,\mathrm{r}} T \ln(\frac{T}{T_0}) + RT \ln K = 0, \tag{2.110}$$

The last two terms on the left hand side can be combined as follows:

$$- C_{p,\mathrm{r}} T \ln(\frac{T}{T_0}) + RT \ln K = RT \ln \left[\left(\frac{T}{T_0} \right)^{-C_{p,\mathrm{r}}/R} K \right] = RT \ln \left[\left(\frac{T}{T_0} \right)^{-f_r} K \right], \tag{2.111}$$

where in the last equation f_r is defined as:

$$f_r = \frac{C_{r,\mathrm{r}}}{R} = \frac{1}{2} \left[\gamma(f_{\mathrm{C}} + 2) + \delta(f_{\mathrm{D}} + 2) - \alpha(f_{\mathrm{A}} + 2) - \beta(f_{\mathrm{B}} + 2) \right]. \tag{2.112}$$

Finally, after rearranging:

$$K = \left(\frac{T}{T_0} \right)^{f_r} \exp \left(- \frac{G^{\ominus}_{\mathrm{r}}(T_0) + (T - T_0)[C_{p,\mathrm{r}} - S^{\ominus}_{\mathrm{m,r}}(T_0)]}{RT} \right). \tag{2.113}$$

To solve this equation and obtain the mole fractions at a particular temperature, it is useful to express the particle numbers in terms of the initial particle numbers $N_{\mathrm{A},0}$, etc. and the *reaction coordinate* or *extent* ξ of the reaction:

$$N_{\mathrm{A}} = N_{\mathrm{A},0} - \alpha\xi \tag{2.114}$$
$$N_{\mathrm{B}} = N_{\mathrm{B},0} - \beta\xi \tag{2.115}$$
$$N_{\mathrm{C}} = N_{\mathrm{C},0} + \gamma\xi \tag{2.116}$$
$$N_{\mathrm{D}} = N_{\mathrm{D},0} + \delta\xi. \tag{2.117}$$

Using $N_{\mathrm{tot}} = N_{\mathrm{A}} + N_{\mathrm{B}} + N_{\mathrm{C}} + N_{\mathrm{D}}$, one can also write the following set of equations for the mole fractions:

$$x_{\mathrm{A}} = (N_{\mathrm{A},0} - \alpha\xi)/N_{\mathrm{tot}} \tag{2.118}$$
$$x_{\mathrm{B}} = (N_{\mathrm{B},0} - \beta\xi)/N_{\mathrm{tot}} \tag{2.119}$$
$$x_{\mathrm{C}} = (N_{\mathrm{C},0} + \gamma\xi)/N_{\mathrm{tot}} \tag{2.120}$$
$$x_{\mathrm{D}} = (N_{\mathrm{D},0} + \delta\xi)/N_{\mathrm{tot}}. \tag{2.121}$$

These equations can then be substituted into the expression for K, equation (2.109) and what remains is a single equation that relates the temperature T to the extent ξ of the reaction and thus to the equilibrium concentrations.

Multiple reactions

This method to determine the equilibrium concentrations can be extended to a mixture of gases, in which multiple reactions can take place. The approach followed will be sketched shortly here and will be applied to the thermal decomposition of water in chapter 5.

A mixture of n different gases is considered (at total pressure $p^{\ominus}$) in which a total of m reactions can take place. A reaction coordinate ξ_j ($j = 1 \dots m$) is assigned to each of the reactions. In contrast to the example above, the equilibrium mole fractions x_i ($i = 1 \dots n$) are now a function of not one, but m reaction coordinates:

$$x_i = x_{i,0} + f(\xi_1, \dots, \xi_m) \quad (1 \leq i \leq n), \tag{2.122}$$

so that for each j the reaction constants can also be written as a function of the ξ_j:

$$K_j = K_j(\xi_1, \dots, \xi_m) \quad (1 \leq j \leq m). \tag{2.123}$$

The reactions are thus described by a system of m equilibrium equations of the type of (2.113):

$$K_j(\xi_1, \dots, \xi_m) = \left(\frac{T}{T_0}\right)^{f_{r,j}} \exp\left(-\frac{G^{\ominus}_{\mathrm{r},j}(T_0) + (T - T_0)[C_{p,\mathrm{r},j} - S^{\ominus}_{\mathrm{m,r},j}(T_0)]}{RT}\right) \quad (1 \leq j \leq m), \tag{2.124}$$

Given T and the initial mole fractions $x_{i,0}$, this system can then be solved to give the equilibrium ξ_j and thus the equilibrium mole fractions x_i.

2.6.2 Molecular spectra

An introduction to the subject of molecular spectroscopy can be found *e.g.* in [46]. A complete treatment of the spectra of diatomic molecules is written by Herzberg [47]. Here, some of the basics concepts will be shortly discussed, as background information for the molecular emission measurements and simulations presented in chapter 5.

States and energy levels

Unlike atoms, molecules have an internal structure that allows them to store energy in the form of vibrational movement of the constituting atoms, relative to another, or by rotation of the molecule as a whole around one of its axes. Apart from the translational kinetic energy (which gives a Doppler broadening/shift) the energy of the molecule is thus written as the sum of three energies:

$$E = E_{\mathrm{el}} + E_{\mathrm{vib}} + E_{\mathrm{rot}}, \tag{2.125}$$

the electronic, vibrational and rotational terms respectively. Rotational and vibrational energy levels can be expressed in terms of a number of molecular constants [47, 17]. Here, they are assumed to be known and this topic will not be discussed further.

The electronic term, like in atoms, is determined by the state of the bound electrons, which is described by a set of quantum numbers. In molecular spectroscopy, the following notation is often used for diatomic molecules [48]:

$$n\ell^w \;\; {}^{2S+1}\Lambda^{+,-}_{\Lambda+\Sigma\;\; g,u}. \tag{2.126}$$

In the first term, that describes the electrons in the outer shell, n is the principal quantum number, $\ell = s, p, d, f, \dots$ the angular momentum, w the number of electrons in the shell. Sometimes a preceding Greek letter $\lambda = \sigma, \pi, \delta, \phi, \dots$ is used to denote the component of angular momentum *in the direction of the molecular axis*, which is called the z-direction. In the second term, that describes the resulting term, $2S+1$ is the multiplicity with S the total spin quantum number, like in atoms. The total orbital angular momentum in the z-direction Λ is denoted by Greek letters $\Sigma, \Pi, \Delta, \dots$ where Σ ($\Lambda = 0$) denotes the ground state (analogous to $S, P, D, \dots$ for atoms). The leading term is usually replaced by a Latin letter $X, A, B, C, \dots$ or $X, a, b, c, \dots$ representing the

electronic states in order of increasing energy, so X is the ground state. For the excited states, capital letters are used when Λ and Σ are the same as in the ground state X. $^+$,$^-$ (for Σ-states) and $_g$,$_u$ denote the symmetry properties of the electronic wave function. Like in atoms (spontaneous) electronic transitions are possible as long as they satisfy a set of selection rules (see *e.g.* [47]).

Now, for each electronic state the rotational and vibrational energies, E_{rot} and E_{vib} can take on different (discrete) values, characterized by the vibrational quantum number v and rotational quantum number J. The vibrational energy increases with vibrational quantum number; the states are at a decreasing distance of typically less than 0.3 eV apart. In electronic transitions all changes of v are allowed, leading to a number of vibrational bands. The intensity of the vibrational bands however, is not the same, as they have different vibrational transition probabilities. These are depending on the internuclear distances in both states involved in the transition, via the so-called Franck-Condon factors. This will not be discussed here. A special class of vibrational states are formed by the *repulsive states*, that do not lead to a stable bond between the atoms. Molecules in a repulsive state eventually dissociate [11].

Unlike its vibrational counterpart, the rotational quantum number can not change arbitrarily in an electronic transition. It is bound to the selection rules: $\Delta J = 0, \pm 1$ and $J' = 0 \nleftrightarrow J'' = 0$, forming the so-called P-, Q- and R-branches (the notation J' and J'' for the upper and lower state is commonly used) [48]. The rotational states are at much smaller energy distances of typically < 0.01 eV, which are generally not the same in the upper and lower electronic state. This eventuates in the different rotational transitions occurring in closely packed series of lines, that make up the vibrational bands. The P-, Q- and R-branches can be further subdivided, depending on the coupling of the electronic spin with the molecular rotation. When the total angular momentum apart from spin is called N, J can be either $N+1/2$ or $N-1/2$. To distinguish between these cases, the corresponding branches are given a subscript 1 or 2 respectively, for both upper and lower state (in that order). So R_{12} is used for a transitions where $J = N + 1/2$ in the upper and $J = N - 1/2$ in the lower state. By convention duplicate subscripts are replaced with single ones: $R_{22} = R_2$.

With regard to the structure of the vibrational bands, the term *band head* is mentioned. When the moments of inertia of the upper and lower state differ, so does the increase in rotational energy with J. However, even in this case, at some particular pairs of values for J' and J'' this increase is approximately equal. This gives a point in the emission spectrum where the lines of this band are extremely close together (and the measured intensity is usually high), which is called the band head. Depending on whether the upper or lower state has the larger moment of inertia, the band head occurs in either the R- or the P-branch (see *e.g.* [46, 48]). An example is given in figure 2.7 for the R_2-branch of the $A^2\Sigma, v' = 0 \rightarrow X^2\Pi, v'' = 0$ electronic transition of the OH molecule.

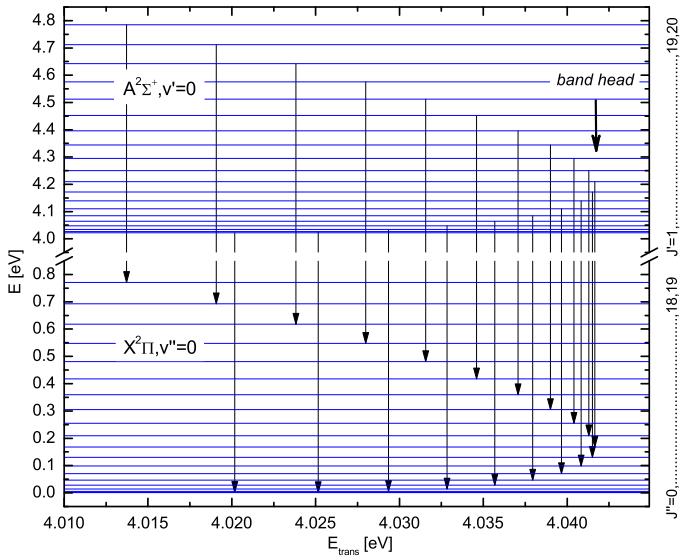

Figure 2.7: *Rotational energy term vs. transition energy for the first 20 transitions in the R_2 branch of the $A^2\,\Sigma, v' = 0 \rightarrow X^2\,\Pi, v'' = 0$ electronic transition of the OH molecule. The transition energy range on the lower axis corresponds to a wavelength range of 309.2 nm–306.5 nm. The band head is at 306.8 nm.*

Vibrational population, chemiluminescence reactions

Vibrationally excited states are often produced from chemical reactions (including dissociative ionization/recombination reactions), in which the excess reaction energy partly ends up in the vibrationally (and electronically) excited product states. The term *chemiluminescence reactions* is used to refer to reactions that produce electronically excited species, which cause visible luminescence on decay.

Besides chemical reactions, all kinds of other processes can affect the vibrational population: electron collisions (e-V energy transfer), vibrational-translational (V-T) transfer, vibrational-vibrational (V-V) transfer, as well as transitions between electronically and/or vibrationally excited states within the same molecule, just to name a few. For the case of N_2, these processes are discussed in detail *e.g.* in [49].

In cases where chemical processes play a dominant role, such as in chemiluminescence reactions, the vibrational population distribution of the excited state can be characteristic for a particular reaction [50]. The next section introduces two more quantities that are needed in order to determine this population distribution from the emission spectrum: the predissociation and quenching rates.

Predissociation, Quenching and Quantum yield

If there exists a finite transition probability between a (meta)stable state and a repulsive (unstable) state the molecule can perform a transition to the latter and subsequently dissociate. This process is called *predissociation*. The probability of this event is expressed in terms of a predissociation lifetime or the inverse predissociation rate K^{pred}.

The term (collisional) *quenching* refers to a variety of processes that can result in non-radiative deexcitation. In case of an excited molecule, this can be various types of energy transfer processes or *e.g.* excited state chemical reactions. As a consequence, quenching rates K^{quench} depend strongly on pressure and temperature, as well as on the type of quencher.

Quenching and predissociation both reduce the lifetime of the excited state. The term *quantum yield* Y_{qp} is often used in this context. It expresses the fraction of the molecules in a particular excited state q that decays through the observed radiative channel $q \rightarrow p$:

$$Y_q = \frac{A_{qp}}{\sum_{p'} A_{qp'} + K_q^{\text{quench}} + K_q^{\text{pred}}}, \tag{2.127}$$

with n_q the population of q, A_{pq} the Einstein emission coefficient and ν_{pq} the frequency of the transition. The emission coefficient is then given by:

$$\epsilon^{qp} = Y_q A_{qp} h\nu^{qp} n_q. \tag{2.128}$$

Rotational population

Because of the small energy difference between the rotational states, their population often quickly thermalizes. In such cases it is described by a Boltzmann population and characterized by a single *rotational temperature* T_{rot}. It can usually be assumed that the occupation is conserved in the excitation process (*e.g.* electron impact excitation) so that the rotational occupation of an excited state is the same as that of the ground state [11]. If in addition rotational levels of the ground state are occupied by heavy particle collisions, the rotational temperature in the excited state will be close to the gas temperature $T_{\text{rot}} \approx T_{\text{g}}$. The rotational temperature of the excited state can be determined from line ratios in the emission spectrum (*e.g.* with a Boltzmann plot). For this purpose, diatomic molecules are often used for gas temperature measurements in plasmas or flames (sometimes called a molecular pyrometer).

Sometimes, excited electronic states are predominantly occupied by other processes than electron impact excitation, *e.g.* by chemical (chemiluminescence) reactions involving the molecule. In these cases the excited state rotational population does not need to reflect the gas temperature

and is in many cases is non-thermal. As the chemical processes usually do not populate all vibrational (and electronic) states to the same extent and in the same way, each vibrational band can have a different rotational population distribution. These non-thermal rotational distributions can sometimes be described by multiple (two or three) rotational temperatures, for different ranges of rotational quantum numbers.

Modeling rotational spectra

Rotational spectra of diatomic molecules can be modeled accurately and many examples of this can be found in literature (see *e.g.* the simulation program LIFbase [51]). The most general approach is to calculate all relevant energy levels using the molecular constants, a model potential for the binding energy as well as calculated emission coefficients (from the Franck-Condon factors and the dipole transition moment).

Another, more pragmatic approach, that can only be used when sufficient measurement data is available, is described *e.g.* in [52]. This is followed here. The intensity of a spectral line corresponding to a transition from level q with density n_q to level p is given by:

$$I_{qp} = n_q A_{qp} h\nu_{qp} l, \tag{2.129}$$

with l the length of the (optically thin) plasma and all the usual symbols. Now when the rotational states are in thermal equilibrium at temperature T_{rot}, the population is Boltzmann distributed:

$$n_q = \frac{n_0 g_q}{Q(T_{\mathrm{rot}})} \exp\left(\frac{-E_q}{k_{\mathrm{B}} T_{\mathrm{rot}}}\right), \tag{2.130}$$

where n_0 is the total molecule density, g_q and E_q the excited state energy and statistical weight respectively and $Q(T_{\mathrm{rot}})$ the partition function, analogously to equation (2.36).

Using the definition $C_{qp} = n_0 A_{pq} h\nu_{pq} l$ (not a function of T) the intensity can also be expressed as:

$$I_{qp} = \frac{C_{qp}}{Q(T_{\mathrm{rot}})} \exp\left(\frac{-E_q}{k_{\mathrm{B}} T_{\mathrm{rot}}}\right). \tag{2.131}$$

Now when the intensity I_{qp}^{ref} of a particular transition is known at a certain reference (rotational) temperature T_{ref} the intensity at another temperature T_{rot} can be expressed as:

$$I_{qp}(T_{\mathrm{rot}}) = I_{qp}^{\mathrm{ref}} \frac{Q(T_{\mathrm{ref}})}{Q(T_{\mathrm{rot}})} \exp\left(\frac{E_q(T_{\mathrm{rot}} - T_{\mathrm{ref}})}{k_{\mathrm{B}} T_{\mathrm{rot}} T_{\mathrm{ref}}}\right). \tag{2.132}$$

Finally, it is assumed that the partition functions depend only weakly on temperature, as will be the case for not too high temperatures, so $Q(T_{\mathrm{ref}})/Q(T_{\mathrm{rot}}) \approx 1$. Thus the intensity of each line can be calculated based on the reference intensity and the energy of the state only. To complete the spectral simulation, the total intensity of all lines (delta peaks) is calculated as follows:

$$I_\delta(T_{\mathrm{rot}}, \lambda) = \sum_{q,p} I_{qp}(T_{\mathrm{rot}}) \delta_{\lambda\lambda_{qp}} \quad \text{with} \quad \delta_{\lambda\lambda_{qp}} = \begin{cases} 1 & \text{if } \lambda = \lambda_{qp} \\ 0 & \text{if } \lambda \neq \lambda_{qp} \end{cases} \tag{2.133}$$

with λ_{qp} is the transition wavelength. This should be convoluted with the appropriate line profile $P(\lambda)$, *e.g.* apparatus response, to obtain the intensity:

$$I_\lambda(T_{\mathrm{rot}}, \lambda) = I_\delta(T_{\mathrm{rot}}, \lambda) * P(\lambda). \tag{2.134}$$

A simulation program using this approach was written for a part of the OH molecular spectrum and examples of simulated OH spectra will be presented in chapter 5.

2.7 Transport and probes

Perhaps the most obvious way to study density and temperature of charged particles in a plasma is to use some kind of solid probe that can measure them directly inside the plasma. The experimental effort needed for such measurements is usually relatively small. Often in sharp contrast to the simplicity of the experimental procedure is the complexity of the theories needed to understand how the probe interacts with the plasma and disturbs the plasma locally. The plasma-probe interaction has been the subject of ongoing research since the first experiments carried out by Langmuir and forms an important subfield of plasma physics. Considering the complexity of the subject and the fact that Langmuir probe measurements form only a small part of the work presented here, no attempt is made to thoroughly introduce the subject. Instead, some basic concepts are introduced and equations that were used to arrive at the results in section 3.5 are given. Introductions to the subject can be found in most plasma physics books, *e.g.* [10, 45]. A recent review from a practical point of view is given in [53].

2.7.1 Plasma potential, floating potential and sheath

The *plasma potential* or space potential V_p, is the electric potential in the undisturbed plasma (in the absence of any probe). When the (position dependent) charge density is denoted by ρ and the electric field by $\vec{E}$, the plasma potential is described by the Poisson equation:

$$\nabla^2 V_\mathrm{p} = \nabla \cdot \vec{E} = -\frac{\rho}{\varepsilon}, \tag{2.135}$$

where ε is the permittivity of the medium, given by $\varepsilon = \varepsilon_0 \varepsilon_r$, where ε_0 is the vacuum permittivity and ε_r is the relative permittivity of the medium.

From gas-kinetic theory it follows that the number of particles of a particular species j crossing through a unit area per unit time (from one side only) is given by:

$$\Gamma = \frac{1}{4} n_j \overline{v_j}, \tag{2.136}$$

where n_j is the density and $\overline{v_j}$ the mean velocity of the particles. When a plasma containing only singly charged ions (i) and electrons (e) is considered, the current from a perfectly absorbing probe of area A is given by:

$$I = -eA\left(\frac{1}{4} n_i \overline{v_i} - \frac{1}{4} n_e \overline{v_e}\right). \tag{2.137}$$

Due their much smaller mass, the mean velocity of electrons in a plasma is usually much larger than that of the ions (at least a factor $\sqrt{m_\mathrm{p}/m_\mathrm{e}} \approx 40$, at comparable temperatures). Therefore, in an undisturbed plasma, the current flows are dominated by the electrons:

$$I \approx \frac{1}{4} eA n_e \overline{v_e} \equiv A J_\mathrm{e}, \tag{2.138}$$

where the electron current density J_e is defined. The probe thus emits a net positive current. Now if the probe is electrically isolated from the surroundings, *i.e.* in a *floating state*, the current will quickly build up a negative charge, that starts repelling more electrons coming from the plasma. The equilibrium potential, at which the ion and electron flows to the probe surface are equal, lies at a few times the electron temperature below the plasma potential and is called the *floating potential* V_f.

In practice, the floating potential is measured by using a probe connected to ground through a very high resistance, so that the probe currents are negligible. By using two such probes at a small separation Δz, and assuming the electron temperature does not vary over this distance, the potential difference is proportional to the electric field $E = \Delta V / \Delta z$.

In a plasma, the disturbing of the potential caused by the probe is compensated by the surrounding charge carriers (mainly electrons), as was the case for the test-particle in section 2.1. This Debye shielding of the probe potential occurs at a scale of a few times the Debye-length,

equation (2.6). This transition region from solid surface to plasma is therefore called the *Debye sheath* or simply sheath. In practice the distance over which the probe disturbs the plasma can be quite a bit larger than the Debye length and depends on both the plasma parameters and the probe geometry.

2.7.2 Saturation currents

When a probe is kept at the plasma potential, one can assume that the plasma is not disturbed, so that the current flowing from the probe is approximated by equation (2.138). Increasing the probe potential above the plasma potential does not change the electron current, as all electrons arriving at the probe are already absorbed. The ion current decreases as ions are repelled, but it was already small compared to the electron current. The corresponding value of I_e is called the *electron saturation current* and denoted as $I_\mathrm{e}^\mathrm{sat}$.

Oppositely, decreasing the potential to below V_p decreases the electron current. When the probe potential is equal to the floating potential, the electron and ion current densities will be equal. When it is decreased further, the electron current will become negligible at some point, at which the current flowing from the probe equals the *ion saturation current* $I_\mathrm{i}^\mathrm{sat}$. The current-voltage characteristic in the transition part between electron- and ion-saturation is determined by the electron energy (and sometimes ion-) energy distributions or temperatures.

In practice, the above discussion is only an approximation and the currents do not completely saturate. A clear bend in the IV-characteristic is often visible, however. An important effect that will allow for a continuing increase of the ion 'saturation' current is the increase of the sheath thickness with decreasing (negative) probe potential. As the probe collects ions from the sheath edge, this leads to an effective increase of the probe area. The effect is most relevant when the probe dimensions are comparable or smaller than the Debye length. Looking for example at a plasma with an electron temperature of 3000 K, the Debye length, given by equation (2.6), ranges from 0.4 μm at $n_\mathrm{e} = 10^{22}$ m^{-3} to 40 μm at $n_\mathrm{e} = 10^{16}$ m^{-3}, so that for most probes this effect should not play a major role.

2.7.3 Probes in collisional regime

The probe behavior described in the previous sections relies on a number of assumptions, which are certainly not always fulfilled. In general the probe IV-characteristic can provide information on (depends on) the electron and ion energy distributions and/or temperatures, densities of electrons and ions and even collision frequencies [53]. The densities are calculated from the saturation currents, whereas most other parameters follow from the transition region. However, not every quantity is always measurable and the way the probe characteristic should be interpreted depends on the plasma and probe parameters. In general, operating regimes (*e.g.* collisionless, non-local and hydrodynamic and various subregimes) can be introduced, based on characteristic length scales in the plasma. The probe behavior in each of these regimes can be very different. This is beyond the scope of this discussion; a review can be found in [53]. Here only a short argument will be made, why the standard collisionless probe theory sketched above, does not apply at atmospheric pressure and the estimated plasma parameters of the plasmoid. The argument is based on a more complete discussion in [10]. Using this, some basic probe measurements conducted, can be understood at least qualitatively.

As mentioned, the probe behavior sketched in the previous sections is only a good approximation in cases where collisions can be ignored and particles travel through the sheath in free flight. In situations where collisions can not be ignored, *e.g.* at high (atmospheric) pressure or at low ionization degree, the behavior can be quite different. In general, the effect of collisions is to reduce the currents to the probe as the particles have to diffuse to the probe, rather than arrive in free flight. An estimate can be made by treating the plasma around the probe as continuum, having a constant diffusion coefficient D. Assuming a spherical probe of radius R the flux of particles to

the probe is then given by [10]:

$$\Gamma_j = \frac{1}{4} n_j^{\infty} \overline{v_j} \frac{1}{1 + \overline{v_j} R/(4D_j)}, \tag{2.139}$$

where n_j^{∞} is the density far from the probe. By comparing with equation (2.136) one sees that the currents are reduced by a factor $[1 + \overline{v_j} R/(4D_j)]^{-1}$. For a 'random walk' the diffusion coefficient can be related by the mean free path λ_{mfp} by: $D = \lambda_{\mathrm{mfp}} \bar{v}/3$, so that this factor can also be written: $[1 + 3R/(4\lambda_{\mathrm{mfp},j})]^{-1}$. This shows that collisions can be ignored if $\lambda_{\mathrm{mfp}} \gg R$, whereas for $\lambda_{\mathrm{mfp}} \ll R$ the currents are reduced approximately by a factor $4\lambda_{\mathrm{mfp},j}/(3R)$. Of course, the perfectly spherical probe, assumed in equation (2.139) is not used in practice. Solving the diffusion equation with boundary conditions for other geometries is possible, but leads to much more complicated solutions. This will not be discussed here.

Taking as an example an atmospheric plasma with an ideal background gas at 1000 K ($n \approx 7 \cdot 10^{24}$ m^{-3}) and estimated 'hard sphere' collision cross section given by $\sigma = \pi a_0^2 \approx 9 \cdot 10^{-21}$ m^2, the collision mean free path is given by equation (2.11): $\lambda_{\mathrm{mfp}} = 1/(n\sigma) \approx 1.6 \cdot 10^{-5}$ m. So, when a probe with a characteristic dimension of 1 mm is used, the currents will be smaller by a factor 60 due to collisional effects, with respect to the collision-free case. Of course this is only a rough estimate that can not be used for precision measurements.

2.7.4 Ambipolar diffusion

As a final topic in this chapter, the concept of ambipolar diffusion is mentioned, as it might give some insight in the charge distribution in the boundary layer of the plasmoids. Starting with the general momentum conservation equation, assuming isotropic pressure $p = nk_{\mathrm{B}}T$ (and thus $\nabla p = k_{\mathrm{B}}T\nabla n$), ignoring magnetic forces and assuming a uniform (neutral) background gas at rest with no sources or sinks, the following diffusion equation for a single (free) species with density n in a plasma can be derived [45]:

$$\frac{\partial n}{\partial t} - D\nabla^2 n = 0. \tag{2.140}$$

Here D is again the diffusion coefficient. Now as the diffusion coefficient is proportional to the mean velocity $\bar{v}$ of the particle, this would suggest that the electrons diffuse much faster from the plasma than the ions. However, the resulting charge separation quickly builds up an electric field E that pulls back the electrons. The diffusion of the charged particles in a plasma is thus tied to the slower species, *i.e.* the ions. A more precise analysis leads to a so called *ambipolar diffusion coefficient* D_{a} that takes the place of D in equation (2.140). When it is assumed that the electrons are much more mobile than the ions, it can be approximated by:

$$D_{\mathrm{a}} \approx D_{\mathrm{i}}(1 + T_{\mathrm{e}}/T_{\mathrm{i}}), \tag{2.141}$$

where D_{i} is the ion diffusion coefficient. So, considering the example at the end of the previous section again, the ambipolar diffusion coefficient should have been used. When T_{i} is still 1000 K but $T_{\mathrm{e}} = 3000$, and the ion diffusion is still determined by the hard sphere collisions with the background gas, one finds: $D_{\mathrm{a}} \approx 4D_{\mathrm{i}}$ and the currents will thus be smaller by a of factor 15, due to collisions.

Chapter 3

Experiments

This chapter is devoted to the results of several experiments, conducted to obtain more insight into the atmospheric plasmoids. First a brief description of the discharge system and the different diagnostic tools is given. Following, the outcomes of the different experiments are discussed. The diagnostic tools and conducted experiments range from very simple to relatively complex. The structure of the sections concerned with each class of experiments is adapted, based on the complexity of the subject. Where the results speak for themselves, *e.g.* for the simple camera recordings, they are summarized in a single paragraph, whereas the sections describing the more complex spectroscopic measurements are divided into different sections for experimental procedure, results and conclusions.

3.1 Experimental setup, diagnostics overview

Figure 3.1 shows a schematic of the experimental setup. It is similar to that in refs. [1, 2, 3] as far as the discharge system is concerned. The cylindrical discharge vessel made of glass or plastics is filled with tap water or water with salt additives. A copper ring at the bottom of the vessel serves as an anode, while the cathode is the central electrode protruding some millimeters above the water surface. A capacitor bank of 1 mF charged to 4.8 kV is switched to the anode causing a discharge with currents between 10 and 100 A. After 100–150 ms the current is shut down by use of a mechanical switch to obtain an autonomous object without external energy supply. The following diagnostic equipment has been used:

- a high speed video camera (500 frames per second) with 1024x1024 pixel CMOS image sensor and 10 bit dynamic range,
- a triggered video camera with 12 bit dynamic range capable of recording a single frame per shot,
- various electric (Langmuir) probes, current and voltage meters and an oscilloscope for signal recording,
- thermocouples (Ni-Cr, up to 1200 K, response time 20 ms),
- pyroelectric sensors with high sensitivity ($> 97\%$) in the spectral range 0.2–20 μm,
- medium resolution ($\lambda/\Delta\lambda \approx 20,000$) absolutely calibrated échelle spectrometer with large spectral range (300–800 nm),
- high resolution ($\lambda/\Delta\lambda \approx 100,000$) spectrometer with a variable 0.1 nm–1 nm wide spectral range in the visible,
- thermometers and precision scales for calorimetric measurements.

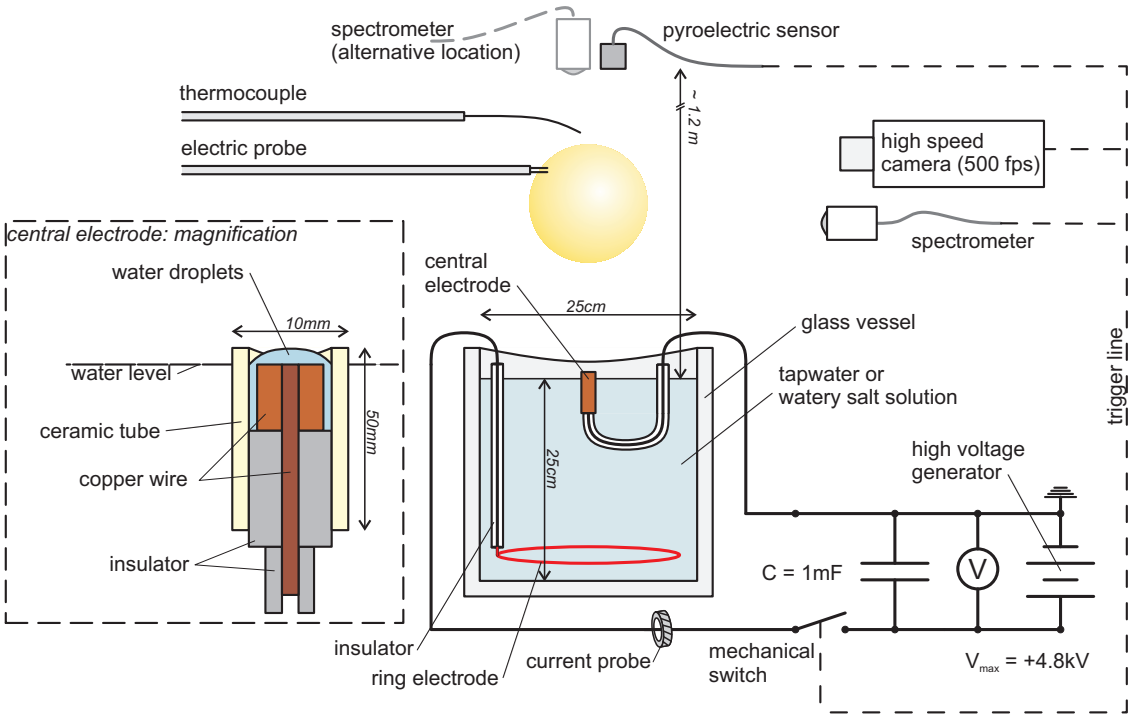

FIGURE 3.1: *Schematic of the experiment and overview of diagnostics. A magnification of the central electrode is pictured in the dashed box on the left.*

A trigger system consisting of (delayed) pulse generators was built to enable synchronized simultaneous measurements using the various diagnostics. As a convention throughout this report, the rising flank of the discharge current is defined as $t = 0$. The discharge switch is typically an oil filled high voltage electronic relay switch, controlled by a pulse generator via a secondary relay switch. For safety reasons, the discharge current was kept under about 100 A by limiting the amount of salt additives in the water. Typically, due to the switch design, the current could not be quenched earlier than $t \approx 130$ ms. In this report the 'lifetime' of the plasmoids is divided into an initial phase and an autonomous phase, corresponding to the period before and after quenching the current, respectively.

In appendix B, a few words are said about the way data from the different diagnostic tools was collected and organized.

3.2 Observations and camera recordings

Shape and dynamics

Figure 3.2 shows the plasmoid's appearance at various times after triggering the capacitor discharge. Initially, the 'streamers' form a spider-like pattern closely above the water-air interface. Above the central electrode the slowly expanding plasma ball emerges. Figure 3.3 (a) shows

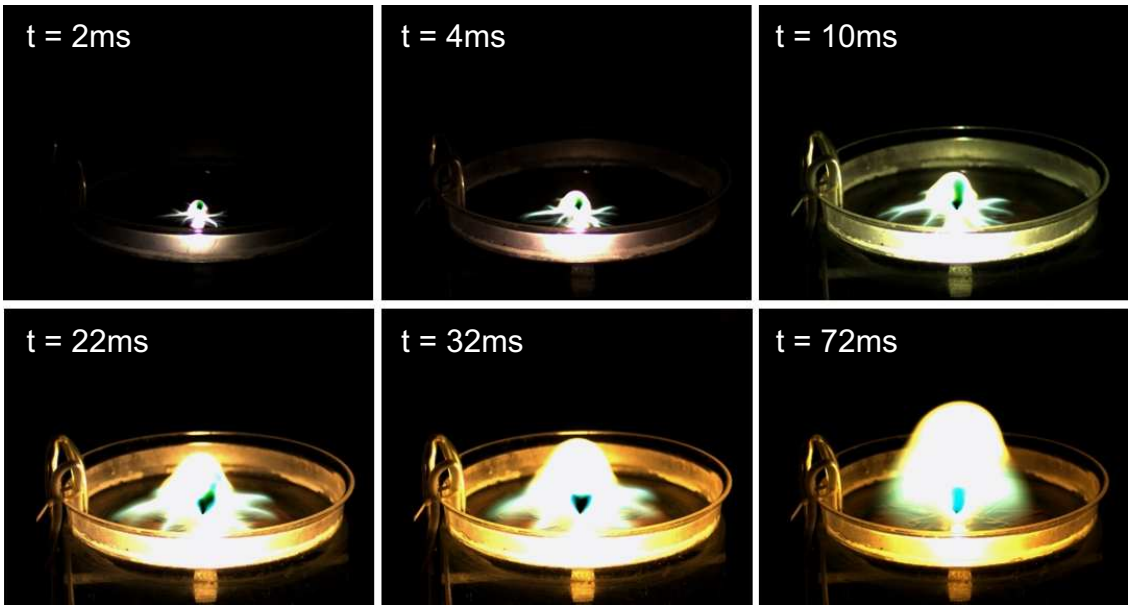

Figure 3.2: *Series of frames recorded using the high speed camera at different times t after triggering the discharge.*

the plasmoid 30 ms after current zero ($t \approx 160$ ms). The bright jet above the ball is due to a camera effect. At this high camera exposure one sees a distinct boundary of the ball. At lower exposure one can sometimes see inner structures which are brighter than the surrounding plasma and change their position rapidly inside the boundary (figure 3.3 (b)). It is clear that the plasma is highly non-homogeneous in this case.

Velocity and size of the plasmoids are determined as a function of time from the high speed camera recordings. This is shown in figure 3.7 (a), in the next section. The velocity (of the upper boundaray) reaches a constant value of 0.8 ± 0.1 m/s after about 50 ms and does not change at current zero. Knowing the velocity of the plasmoid, height over the central electrode can be converted into time of arrival of the ball at a certain position and vice versa. This was used for all diagnostic tools. The ball radius increases from about 4 cm at 30 ms up to 8 cm at 250 ms. Inner structures as shown in figure 3.3 (b) have a higher upward velocity up to 3 m/s until they reach the upper periphery where they are slowed down and bent to the sides to form a toroidal structure towards the end of the lifetime. Typically, the plasmoids have disappeared from the high-speed camera recordings at about 500 ms, though sometimes (non-radiating) toroidal clouds of aerosols or dust particles ("smoke rings") were observed rising up to 4 m or higher over 2–3 seconds.

Salt additives

Discharges were conducted using both ordinary tap water and water with salt additives. The type and amount of salts added to the water has a strong effect on the appearance of the plasmoids. This is illustrated for three different salts in figure 3.4, which shows a comparison of discharges using de-ionized water with various salt additives. Although the de-ionizing was incomplete, there are

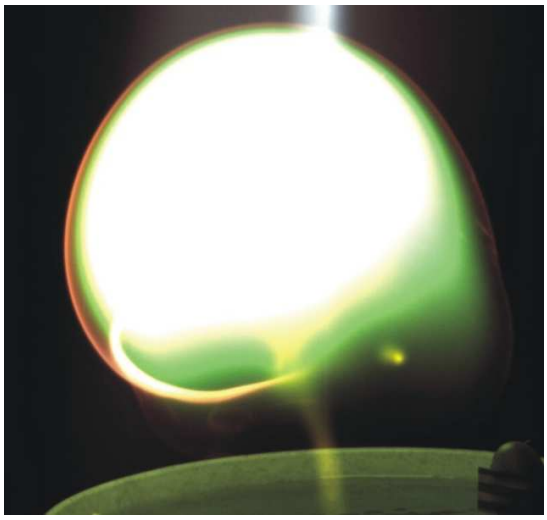

(a) High exposure video capture showing the distinct boundary layer.

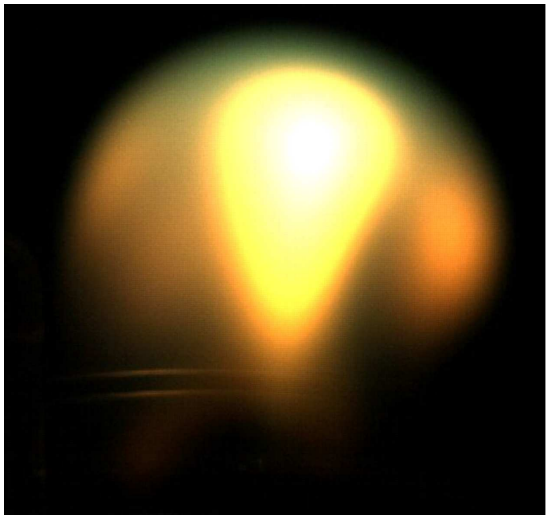

(b) Low exposure video capture showing inner structure of the plasma ball. In this example the effect is stronger than usual.

FIGURE 3.3: *Video captures taken at approximately 30 ms after current zero (t ≈160 ms). The diameter of the ball is ∼12 cm; the magnification in both images is approximately equal.*

distinct differences. Several salts were used, including NaCl, $CuSO_4$, $CaCl_2$ and LiI and it appeared that discharges with salts containing calcium were particularly bright. The characteristic colors of the plasmoids using tap-water are yellow-white in the center and red-green in the boundary layer. When using de-ionized water and pure salt additives, the color changed (at least partly) to that of the characteristic strong (resonance) lines of the anion, *e.g.* orange in the case of sodium (589 nm) or red for lithium (610 nm). When using salts added to normal tap-water yellow-white with red-green boundary mostly remain the dominant colors.

Boundary layer

The boundary layer clearly distinguishes itself from the bulk plasma by its color and its lower intensity. Two other observations seem to suggest that the temperature in the boundary layer may be much lower than in the central plasma:

- A piece of paper placed in the path of the discharge is not burned. The plasmoid deforms and expands to the sided and the boundary layer seems to shield the paper from the plasma.
- Sometimes small 'droplets' (or minor secondary discharges) shoot up from the electrode after plasmoid's formation. When one of these passes through the boundary layer, its intensity first decreases and then increases again when it enters the bulk plasma.

The existence of the cooler boundary layer is confirmed by spectroscopic measurements, as will be shown later.

Vortices

The formation of these torus shaped vortices starts during the discharge and appears to be analogous to other gas phase vortices such as mushroom clouds or smoke-rings. The flows in a mushroom cloud are illustrated in figure 3.5. Very similar vortices can also be found in liquids, *e.g.* in experiments using colored liquid ejected into water from a cylindrical tube (see *e.g.* [54], page

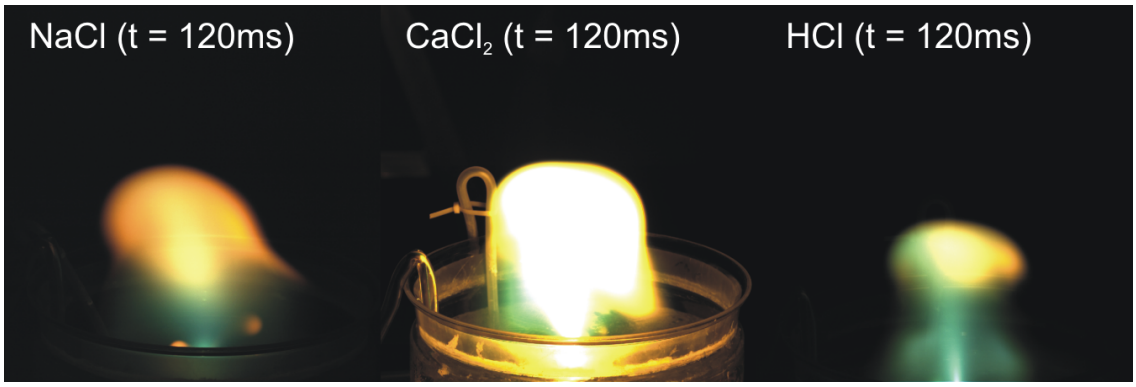

Figure 3.4: *Images recorded using the high speed camera at t=120 ms, using de-ionized tap water with different salt additives. In each case, approximately 4 g of salt was added. It must be noted that the de-ionizing was incomplete, as spectral lines of salts from the tap water remained even after de-ionizing.*

364–365). All of these vortices start with the expansion of material, of say medium B, into another medium, say A. Initially the expanding medium has the shape of (part of) a sphere. The friction of medium A on the outside of the sphere drives the rotational flow. The moving blob of B leaves a low-pressure void behind it. The resulting inward flow of A causes the characteristic mushroom shape. When the inward flowing material is bent upwards and accelerated, *e.g.* by convection it can penetrate the body of B and form a torus. Once a torus is formed, the larger surface area on the outside with respect to the inside of the torus, ensures that the friction of A continues to drive the rotation.

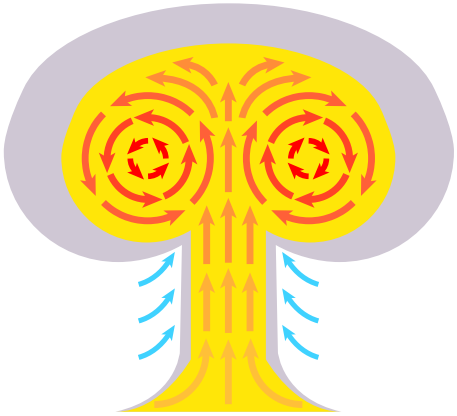

Figure 3.5: *Illustration of the flows in a so-called 'mushroom cloud'. The dark red arrows are hot gas, the blue arrows are cold air flowing into the low-pressure void, formed behind the rising cloud. Figure adapted from [55]. Similarly looking vortices in liquids are described in [54] (see text).*

Filtered camera recordings

Figure 3.6 shows a frames recorded using the high speed camera at different times t after triggering the discharge, using a band filter with maximum transmissivity (0.30) at 656±8 nm. The indicated margin of 8 nm is the Full Width at Half Maximum (FWHM) of the peak in the transmissivity. The hydrogen Balmer-α (H_α) line at 656.3 nm falls in this wavelength interval (there may be other lines and molecular band emission as well). The size of the plasmoid is approximately the same as before. However, the pictures recorded with the filter show a more distinct inner structure than without. It can *e.g.* be seen how a small 'secondary plasmoid' is formed, after the main one seems to have already detached from the electrode. Driven by convection this secondary blob of hot material rises faster than the main plasmoid, passing through it at about $t = 130$ ms.

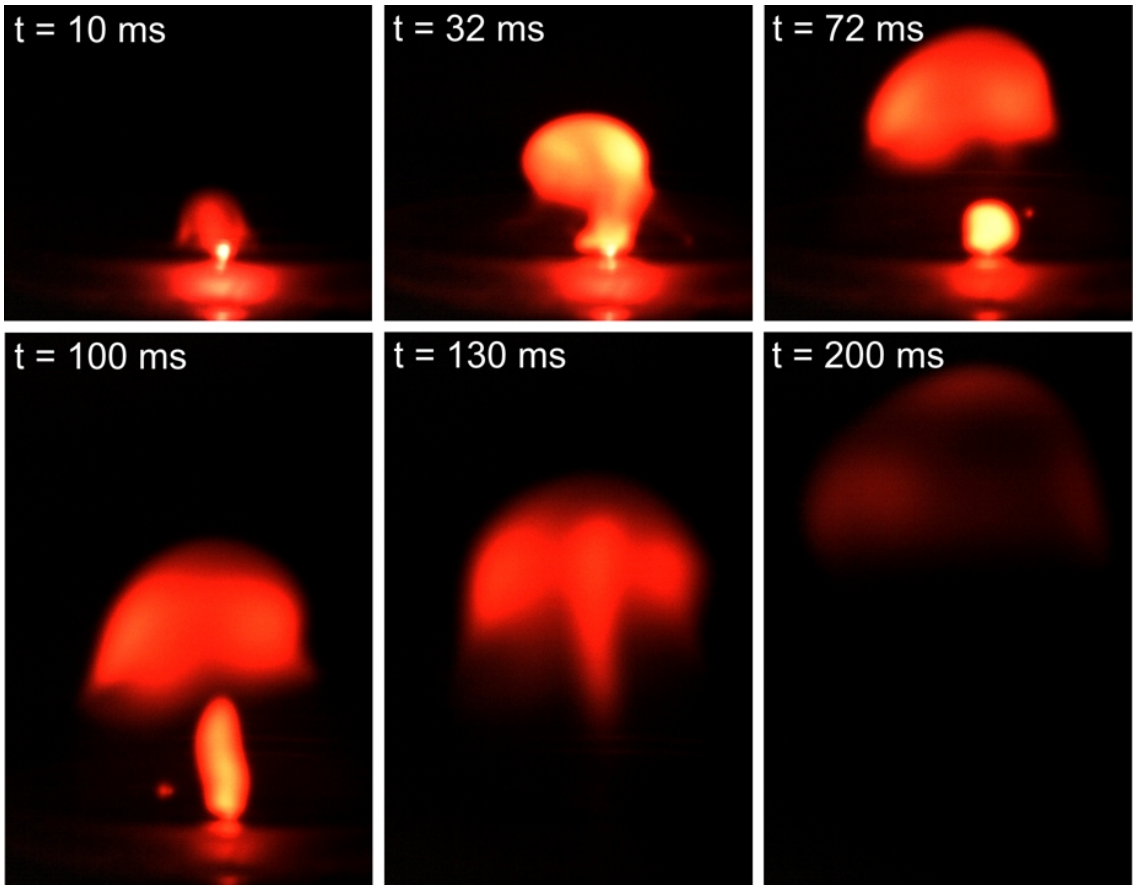

Figure 3.6: *Series of frames recorded using the high speed camera at different times t after triggering the discharge, using a band filter with maximum transmissivity (0.30) at 656 ± 8 nm (FWHM).*

3.3 Discharge, calorimetry and temperature

3.3.1 Experiments

Calorimetric measurements have been conducted, involving the following:

- Discharge current and voltage measurements: the ring electrode voltage V_{ring} and discharge current I_{dis} are measured using a simple high-voltage probe and a contactless current sensor (Rokowski coil) respectively.
- Scales with a precision of 0.1 mg and maximum load of 1 kg were used to measure the mass decrease (evaporation) of the water in the vessel. Limited by the maximum load of the precision scales, this measurement was done using a small version of the vessel with a volume of 1 l.
- To estimate the energy loss due to Ohmic heating, the water temperature was measured using a digital thermometer with a precision of 0.1 K, simultaneous with the weight measurements. Since temperature gradients were observed, the temperature was measured both near the water surface and near the bottom. These temperatures were averaged using of 1/3 and 2/3 respectively; an estimate based on temperature measurements at various heights.
- A pyroelectric sensor was used to measure the time-dependent radiation power emitted by the plasmoid over a large spectral range. The sensitivity of the sensor is above 97 % in the wavelength range of 0.2–20 μm. A short description of this sensor and the conducted calibration can be found in appendix A.
- Extremely thin thermocouples (0.25 mm diameter, Ni-Cr, estimated response time 20 ms) were placed at several heights above the vessel to measure the gas temperature in the plasmoid, in its autonomous phase. The thermocouples use an isolated hot-junction, *i.e.* not in electrical contact with the surrounding steel, connected to a scope. The outer steel shielding is in an electrically floating state to prevent heating due to current flows.

The goal of these measurements is to gain insight in the main energy conversions, involved in the formation of the atmospheric plasmoids. As most measurements showed considerable statistical fluctuations and no attempt was made to optimize the precision of the calorimetric measurements, the results should be seen as estimates.

3.3.2 Results

Discharge

Discharge current and voltage measurements are shown for a discharge with tap water in figure 3.7 (b). As mentioned, the maximum discharge current (as well as the brightness of the plasma balls) can be increased by adding salts to the water, increasing the conductivity. The standard voltage and capacity used for all other experiments are 4.8 kV and 1 mF, unless explicitly stated differently. For such a typical shot the energy delivered from the capacitor bank to the discharge is about 8 kJ, determined from the difference between the initial and remaining voltage over the capacitor.

Water heating and evaporation

The amount of water evaporated per shot and the increase in temperature of the water in the vessel with a volume of 1 l are shown in figure 3.8 (a) and (b). These measurements yield that using a 4.8 kV, 1 mF discharge, on average about 0.1 g water is evaporated per shot. Using the standard molar enthalpy of vaporization of water (40.7 kJ/mol), one finds that this requires an energy of about 0.2 kJ. The water temperature increase is around 1.2 degree, with large uncertainty due to temperature gradients in the water. From the specific heat capacity of water ($C_p = 75.3$ Jmol^{-1}K^{-1}) this corresponds to an energy of approximately 5 kJ.

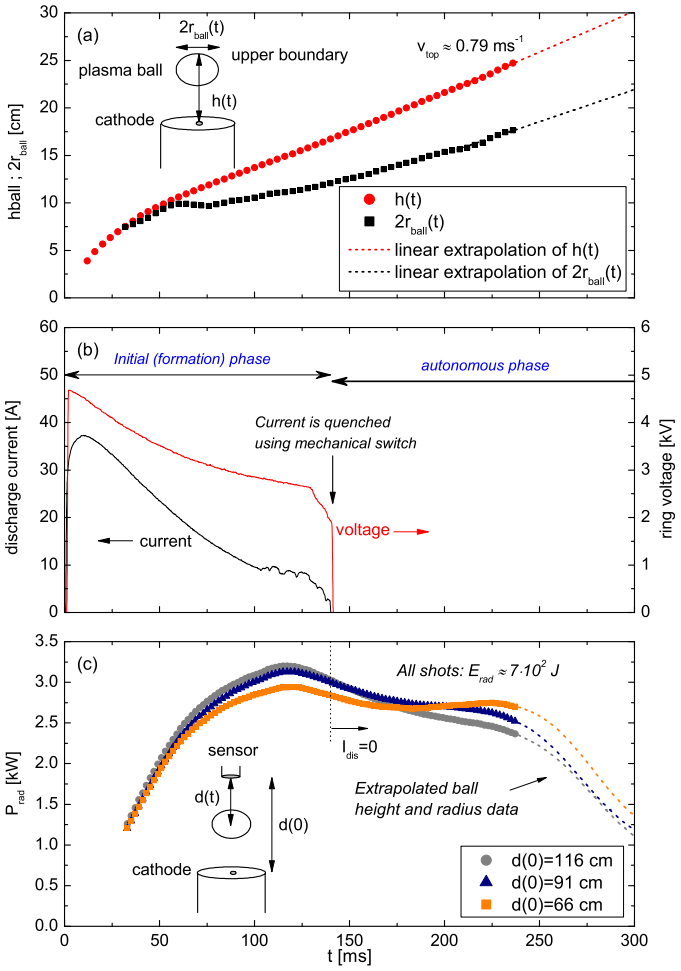

FIGURE 3.7: *Time-dependent parameters of the plasmoid: (a) height and diameter measured using the high-speed camera; (b) discharge current and voltage; (c) radiation power measured using a pyroelectric sensor with high sensitivity in the range of 0.2–20 µm. The lifetime is divided in an initial (formation) phase and an autonomous phase based on the discharge current value.*

Radiation power

The (wavelength integrated) radiation intensity (in Wm^{-2}) measured using the pyroelectric sensor was converted to radiated power, shown in figure 3.7 (c). For this, the distance $d(t)$ from the sensor to the center of the plasma ball was used, as indicated in the drawing inside figure 3.7 (c). The plasmoid is thus considered a point source for the radiation power calculation. This is a good approximation at the relatively large distances used; confirmed by the fact that the curves measured at different distances deviate only slightly. At times $\gtrsim 250$ ms, the position of the plasmoid was extrapolated linearly, as it could no longer be determined accurately from the video recordings. The total emitted radiation energy E_{rad}, determined by integrating the power, is found to be about 0.7 kJ for a standard discharge with tap water.

Gas temperature

The results of the thermocouple measurements are shown in figure 3.9. Temperatures of about 900 K at $t \approx 235$ ms and 600 K at $t \approx 260$ ms were measured. For $t \approx 200$ ms thermocouples indicated 1300 K and more, but were damaged during the measurements, so that the results are no longer reliable. The gas temperature for $t < 200$ ms may thus be considerably higher.

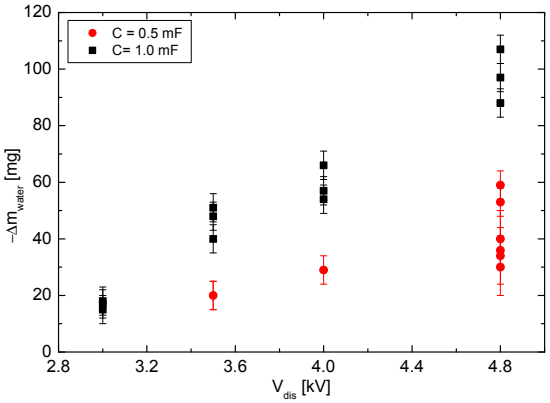

(a) Water mass decrease per shot, depending on discharge voltage and capacity. The error bars indicate the readout uncertainty, mainly due to continuous 'background' evaporation.

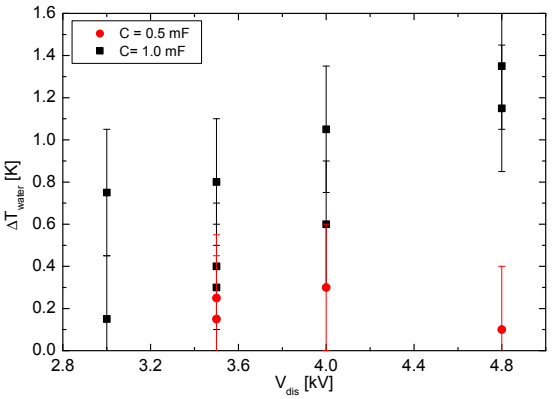

(b) Water temperature increase, depending on voltage and capacity. Each plotted values is the weighted average of one measurement near the surface and one near the bottom of the vessel, using weights of 1/3 and 2/3 respectively.

Figure 3.8: *Results of calorimetric measurements, using precision scales and thermometer, on the water in the 1 l vessel.*

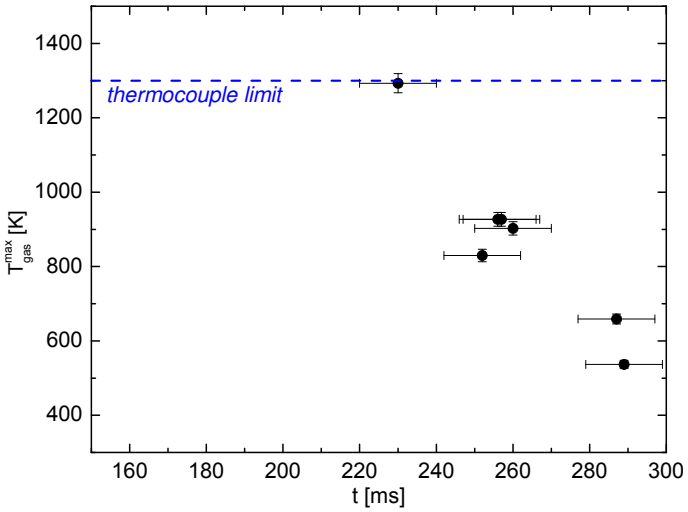

Figure 3.9: *Results of gas temperature measurements using 0.1 mm diameter Ni-Cr thermocouples with a response time of less than 20 ms. The vertical error bars are the thermocouple specified measurement uncertainty and do not include other possible sources of error. The maximum measurable temperature of about 1300 K is also indicated.*

3.3.3 Discussion and conclusions

Calorimetric measurements yield that of the 8 kJ released in the discharge, on average about 5 kJ is spent on ohmic heating of water and only a small fraction of this is used of evaporation. Thus about 3 kJ is available for the formation of the plasma ball.

It is noted that these values may depend on the salt concentration, *i.e.* on the conductivity of the water. It was observed that the discharges in the small vessel with a volume of 1 liter were somewhat smaller and appeared less intense than in the regular vessel. Therefore, these results can only be considered rough estimates. Nevertheless the results are thought to give a reasonable insight into the main energy conversions in the discharges, as intended.

The maximum radiation power measured using the pyroelectric sensor is approximately 3.2 kW, at $t \approx 120$ ms. Using the Stefan-Boltzmann law $4\pi r_{\text{ball}}^2 \sigma T^4$ with $r_{\text{ball}} \approx 5$ cm, this corresponds to the radiation power of a black body at a temperature of about 1200 K. At this temperature the bulk of the black-body radiation is in the infrared (maximum at 2.4 μm according to Wien's law) and well in the range of high-sensor sensitivity.

The black-body temperature of 1200 K is consistent with the gas temperature, measured at $t \approx 200$ ms. As mentioned in the previous section, the existence of gradients, *i.e.* a hot core surrounded by cooler plasma, is likely and can explain the destructed thermocouples at earlier times.

3.4 Emission spectroscopy

Emission spectroscopy in the visible wavelength range is the main plasma diagnostic technique used in this research. As the applications of spectroscopy are so diverse, so is the level of complexity of the data interpretation. In this chapter, measurements are presented from an experimental point of view. The specifications and applications of the various spectrometers are discussed and examples of measurements, providing new information about the plasmoids, are given. This includes measurements of overview spectra and their time-development, broadening of single lines as well as the measurement of atomic line intensity ratios. Two topics that are based on results of emission spectroscopy, but require more complex models to interpret the data, are the study of the line spectrum of atomic calcium and OH emission bands. Results specifically related to those topics are not presented here, but in chapters 4 and 5, from a conceptual point of view.

3.4.1 Spectrometers and experimental procedures

Two different spectrometers were used, each with their own merits and applications. In the following they are briefly described.

- *Échelle spectrometer* The concept of the échelle spectrometer was introduced in section 2.5.3. The spectrometer used is a commercial built LLA Instruments ESA 3000, with a spectral range of 200 to 800 nm using diffraction orders between 30 and 120. Due to the design, some blind spots in the spectral range are present at the red end of the spectrum (above 550 nm), where the image falls outside of the camera chip. The resolving power is $\lambda/\Delta\lambda \approx 20,000$, based on FWHM, corresponding to a spectral resolution ranging from 10 pm to 39 pm. The spectrometer uses a water cooled 1024x1024 pixel Kodak KAF 1001 CCD camera and a Proxitronic image intensifier with microchannel plate (MCP). The CCD camera readout time is approximately 3 s, limiting the measurements to a single frame per shot. The spectrometer was absolutely calibrated over almost the complete spectral range, as is described in appendix C. The sensitivity of the intensified CCD camera is controlled by adjusting the voltage over the MCP, enabling measurements over a wide range of intensities with short exposure time. This high, flexible sensitivity in combination with the large spectral range and good resolving power made the échelle the most versatile and powerful diagnostic tool that was used. It should be noted that the échelle was only available for limited time, much of which was consumed by technical issues, so that for some measurements only limited data is available.

- *High resolution spectrometer* This is a 3 m focal length double-pass spectrometer, using a small spectrograph as input monochromator. The resolving power achieved was in the order of 100,000, clearly lower than the estimated theoretical maximum resolving power of about 10^6, for various technical reasons. The spectral range varied between 0.1 nm and 1 nm, depending on the wavelength (*i.e.* diffraction order) and the magnification of the camera objective. The 1024x512 pixel water cooled intensified CCD camera generated considerable background noise (also due to a broken pixel), depending on the exposure time and multichannel plate voltage. The measurements can be characterized as photon-starved, especially at longer wavelengths, making it a challenge to obtain good signal-to-noise ratios for all but the strongest lines. As no (white) reference light source with sufficiently high and known intensity was available, no absolute calibration was conducted. Resolving power and linear dispersion are determined from known lines measured from various types of low pressure hollow-cathode lamps.

As pictured in figure 3.1 two measurement positions, a top- and a side-view, were used. As it turned out, though the top-view made timing easier, it had the disadvantage that the electrode is in the field of view (at least for a central radial position, $r = o$). Especially towards the end of the lifetime the frequent 'after burning' (*e.g.* due to incomplete opening of the switch) could easily be confused with emission from the plasmoid. Furthermore, larger gradients in the plasma

parameters can be expected to exist vertically than horizontally. Therefore, and as as triggering (assisted by the high speed camera) worked reliably, only the side view was used with the high-resolution spectrometer. The spectra recorded with the échelle all use the top-view. In both cases, the spectrometer's line-of-sight is a tightly collimated beam of 1 cm to 2 cm in diameter. Dark correction is applied to all data and and flat-fielding (correction for the apparatus response) is only applied to the échelle data. For the high resolution spectrometer, no flat-fielding was applied, as stated before. Further details concerning the various spectroscopic experiments will be mentioned with their results in the following section.

3.4.2 Spectroscopy results

This section discusses the results of the various spectroscopic measurements: overview spectra and line intensity ratios recorded with the échelle spectrometer and line-broadening measurements using both the échelle and the high-resolution spectrometer.

Overview spectra

Emission spectra recorded using the échelle spectrometer at different times after the start of the discharge can be seen in figure 3.10, for a series of shots with approximately 0.3 g/l calcium chloride added to the water in the vessel. It should be noted that the spectral resolution in this figure is reduced for clarity. Most of the atomic lines and molecular bands could be identified; only some of them are indicated in this figure.

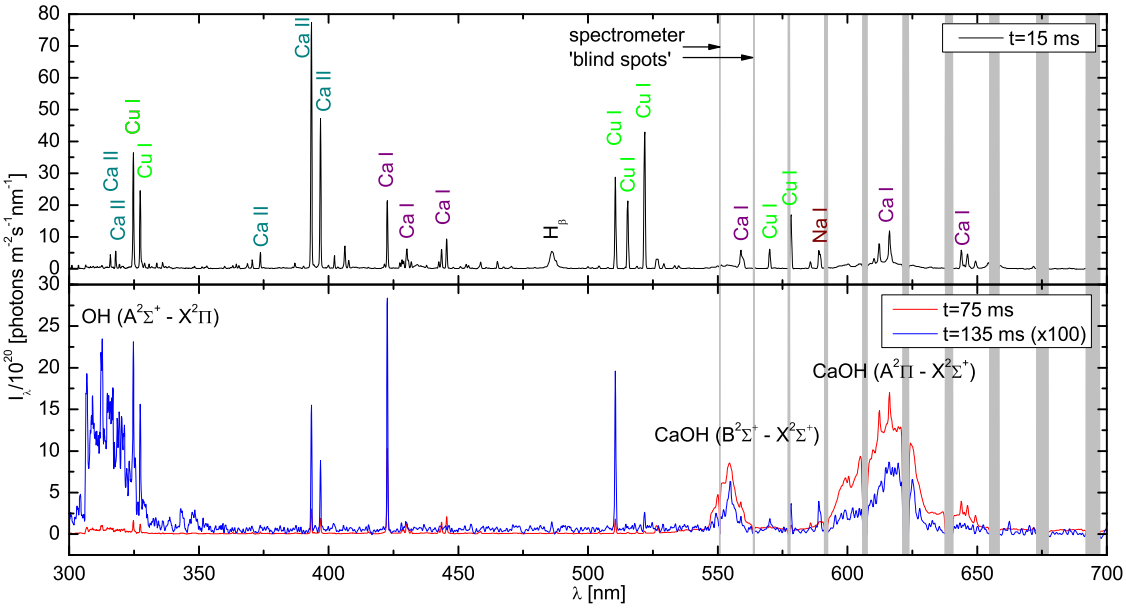

FIGURE 3.10: *Overview spectra recorded with échelle spectrometer (top view) at different times, with approximately 0.3 g/l $CaCl_2$ added to the water. The resolution has been decreased artificially by convolution with a 40 pixel FWHM Gaussian, to increase the visibility. The resulting resolving power is roughly 1000. The calibration is absolute and the measurement at t=135 ms has been scaled by a factor 100. Peaks corresponding with those in the measured spectrum are indicated by the capital letters.*

In these and other spectra recorded from discharges with tap water alone, lines of the following atomic species were observed: Ca, Cu, Na, Al, K, Sr, Mg, Fe, Mn and H. Lines of Ca II, Cu II, Fe II, Sr II and Mg II ions were also seen, as well as weak lines of the twofold ionized Sr III. Besides

atomic and ionic lines, molecular bands of OH (A-X) and CaOH (A-X) and (B-X) electronic transitions have been identified.

The strongest lines in all of the spectra are the resonance lines of Ca, Ca II, Na and Cu. Looking in more detail, it can be seen that these resonance lines are mostly optically thick, whereas radiative transitions from higher excited states seem mostly optically thin (from the line shape and intensity ratios of lines from the same multiplet). Also the transitions between higher excited states decrease in intensity much more rapidly than the resonance lines.

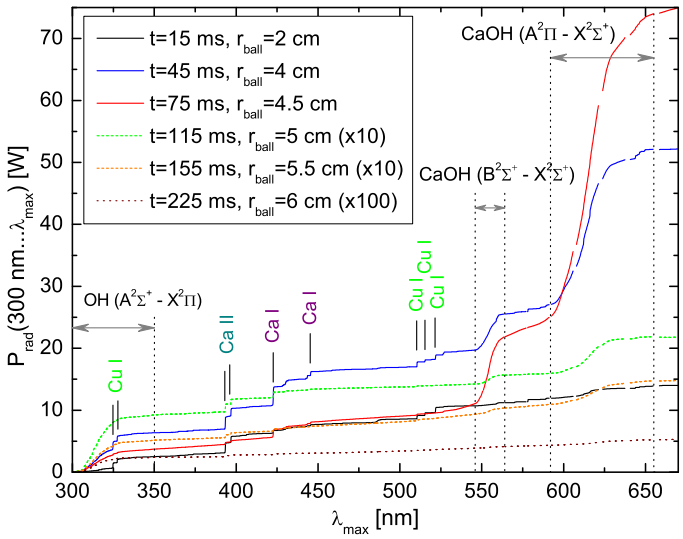

Figure 3.11: *Radiation power between 300 nm and $\lambda_{\max}$ at various times, for the same measurement series as in figure 3.10. The power is calculated using equation (3.1). Note that the data of t=115 ms and t=155 ms have been scaled by a factor 10 and that of t=225 by a factor 100.*

The total radiation power in the range between 300 nm and $\lambda_{\max}$, shown in figure 3.11, is calculated using:

$$P_{\mathrm{rad}}(300\ \mathrm{nm}\ldots\lambda_{\max}) = \frac{1}{2r_{\mathrm{ball}}}\frac{4}{3}\pi r_{\mathrm{ball}}^3 \int_{300\ \mathrm{nm}}^{\lambda_{\max}} I_\lambda \mathrm{d}\lambda, \tag{3.1}$$

with r_{ball} the plasma ball radius, determined from figure 3.7, I_λ in $\mathrm{Wm^{-2}nm^{-1}}$ and $\mathrm{d}\lambda$ in nm. The integral was calculated numerically using a trapezoidal rule so that the spectrometers 'blind spots' were automatically interpolated. From this figure it is clear that, during most of the plasmoid's lifetime, the bulk of the visible radiation belongs to the green and orange/red CaOH molecular bands, determining its characteristic color. UV emission of the OH molecular band is also relatively strong. The total radiation power in the range between 300 nm and 670 nm emitted by the plasmoid increases up to about 75 W (an amount of light about 15 times that 100 W light bulb) at $t = 75$ ms and then decays again. The radiation power of the atomic lines on the other hand, reaches its maximum earlier, between 15 ms and 45 ms, and has already significantly decreased at $t = 75$ ms.

From these simple observations, some preliminary conclusions can already be drawn. The atomic lines in the spectrum all belong to species with relatively low lying excited states < 5 eV (except for H; its lines rapidly disappear). Lines of other elements with higher excited states which are likely to be present in the plasmoids, such as Cl or O, do not occur. Therefore the electron temperature is expected to be less than 1 eV. From the more rapidly the decreasing intensity of the lines between higher excited states it is clear that the electron temperature decreases. The presence of CaOH and OH molecular bands suggests that water is dissociated. Both bands are known to occur in flames where they are produced from chemiluminescence reactions. The molecular processes and emission will be elaborated on in chapter 5.

Resonance lines

Figure 3.13 shows the strongest atomic resonance lines (transitions to the ground state) present in the spectra, at $t = 55$ ms and $t = 145$ ms. The vessel is filled with tap water, in which 0.2 g/l

HCl is solved.

The appearance and size of the plasmoids is illustrated in figure 3.12. The approximate width of the apparatus profile can be seen *e.g.* from the iron line at 323.4 nm. The Cu I resonance lines (324.8 nm, 327.4 nm) are extremely optically thick throughout most of the lifetime, whereas the initially comparably thick Ca I resonance line (422.7 nm) decreases more rapidly in optical thickness. For both species clear self-reversal is visible, due to absorption in the cooler boundary layer. Ca II resonance lines (393.4 nm and 396.9 nm) are optically thick initially but seem close to optically thin at $t \simeq 150$ ms, having a ratio of nearly 2 to 1, determined by their statistical weights. The situation for sodium and strontium lines is similar though their optical thickness is lower overall, due to a lower concentration of these elements. The calcium ion lines show clear opacity broadening (*i.e.* high optical thickness) but no self-reversal, suggesting a lower ion density in the outer region.

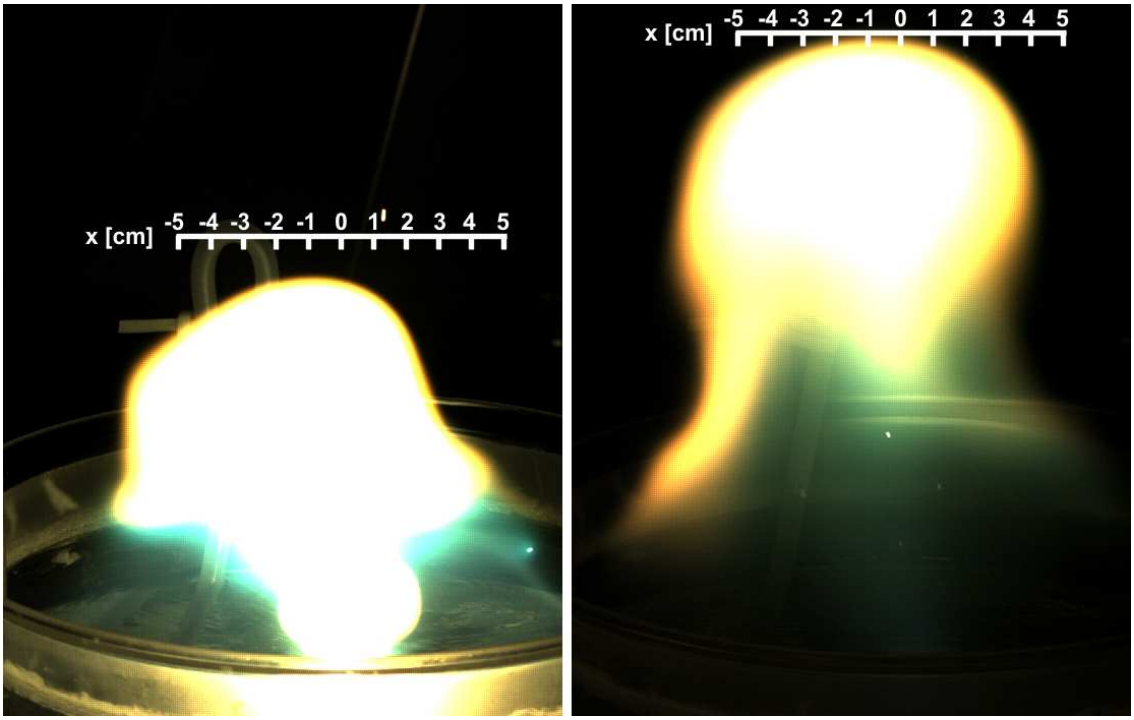

FIGURE 3.12: *High speed camera frames at t=55 ms (left) and 145 ms of discharge using tap water with 0.2 g/l HCl.*

Also in figure 3.13 are three curves indicating the black body intensity calculated using Planck's law, equation (2.45), at temperatures of 3000, 3100 and 3200 K. At $t = 55$ ms (black lines) the resonance lines of Cu, Ca I and Ca II all fall in the range of the black body intensity between 3000 K and 3200 K. The sodium and strontium lines with lower optical thickness have an intensity that is a factor 5 to 10 lower. As some of the lines are partially self-reversed, the electron temperature in the center of the plasmoid is expected to be higher than these values, whereas T_e in the boundary layer may be lower.

This argument can be quantified using the solution of the radiation transport equation. This can also be used to obtain estimates for the (ground state) densities, as will be shown using a simple model in the following paragraph.

The light is assumed to originate from two layers of plasma: a center and a boundary, with thicknesses d_c and d_b, ground state densities n_c and n_b and electron temperatures $T_{e,c}$ and $T_{e,b}$ respectively. The center is shielded by the boundary (as introduced in 2.5.1). The states involved in the transition are assumed to be in LTE, so that the intensity is given by equation (2.55). It

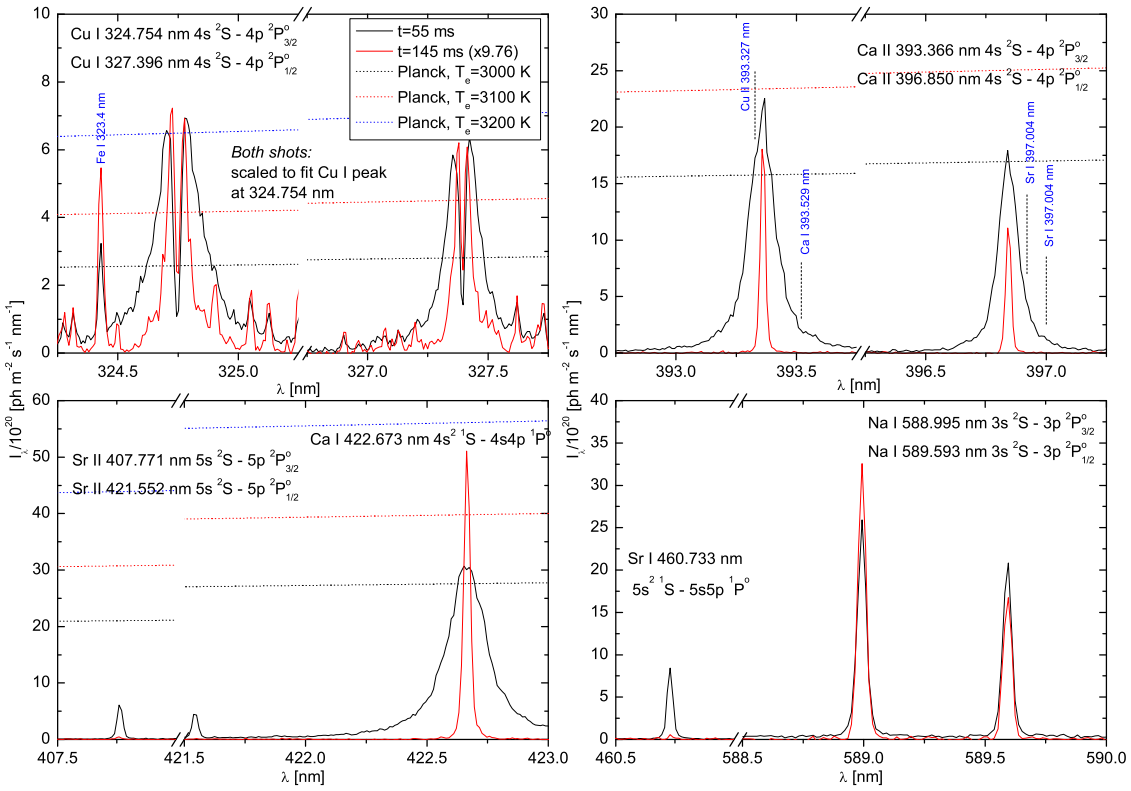

Figure 3.13: *Resonance lines of Cu I, Ca I, Ca II, Sr I, Sr II and Na I, recorded with échelle spectrometer from above, at x=1 cm, t=55 ms and t=145 ms for shots with tap water with 0.2 g/l HCl. The spectrum at t=145 ms is scaled to match the height of the Cu resonance lines (same factor in all graphs). Also shown in the graph is the black-body intensity at temperatures of 3000, 3100 and 3200 K (dotted lines), calculated using equation (2.45), showing that at t=55 ms the Cu I, Ca II and Ca I resonance line intensities lie close to the Planck curve at these temperatures. Some identified neighboring lines are indicated in blue. In the case of Ca II these lines affect the line profile of the resonance lines.*

will be shown later that this will not necessarily be correct at later times ($t \gtrsim 75$ ms), but this is ignored for now. The two layers are assumed to be uniform, so that the optical thicknesses are given by $\tau_{\lambda,i} = \kappa_{\lambda,i} d_i$. The absorption coefficients $\kappa_{\lambda,i}$ are given by the Ladenburg relation (2.57). To evaluate this relation, next to atomic parameters an expression for the line profiles $P_i(\lambda)$ is needed. The line profile is determined by a combination of broadening mechanisms, as discussed in section 2.5.2. Some estimates for the Ca I line at 422.7 nm are made:

- The natural line width is about 0.02 pm (all widths in this section are FWHM) and can be neglected.
- Doppler broadening is determined by the gas temperature. Using the atomic mass of calcium $M = 40$ and an estimated $T_g = 2000$ K in equation (2.68) one finds $w_D \approx 2.1$ pm.
- Van der Waals broadening depends on the perturber type (polarizability) and density. Assuming H_2O perturbers ($\bar{\alpha} = 1.45 \cdot 10^{-24}$ cm^{-3}) and the density of an ideal gas at 2000 K, using equations (2.69)–(2.71) a Lorentz width $w_{vdw} \approx 2.4$ pm is found.
- The resonance lines are relatively Stark-insensitive, as can be seen for the Ca I line at 422.7 nm in table 2.1. Stark broadening can be neglected with respect to Van der Waals broadening for $n_e \ll 10^{22}$ m^{-3}, as will turn out to be mostly the case.

The line profile can thus be approximated by the pseudo-Voigt profile, with Gauss width w_{D} and Lorentz width w_{vdw}. As the observed opacity broadening is much larger than all of these widths, the far-wing behavior of the lines is most important, *i.e.* the Lorentz part. Estimates for w_{vdw} and w_{D} for other resonance lines, obtained in the same way, are shown in table 3.1.

TABLE 3.1: *Parameters of resonance transitions, shown in figure 3.13. The atomic data is taken from [15]. The Van der Waals width w_{vdw} [pm] is calculated using equations (2.69)–(2.71), assuming H_2O perturbers ($\bar{\alpha} = 1.45 \cdot 10^{-24}$ cm^{-3}) and the density of an ideal gas at 2000 K. The last column is the Doppler width at $T_g = 2000$ K.*

Species	λ_0 [nm]	g_p	g_q	A_{qp} [s^{-1}]	w_{vdw} [pm]	w_{D} [pm]
Cu I	324.4	2	4	$1.39 \cdot 10^8$	1.1	1.3
Cu I	327.4	2	2	$1.37 \cdot 10^8$	1.1	1.3
Ca II	393.4	2	4	$1.47 \cdot 10^8$	0.76	2.0
Ca II	396.9	2	2	$1.4 \cdot 10^8$	0.77	2.0
Sr II	407.8	2	4	$1.42 \cdot 10^8$	2.7	1.4
Sr II	421.6	2	2	$1.27 \cdot 10^8$	2.7	1.4
Ca I	422.7	1	3	$2.18 \cdot 10^8$	2.4	2.1
Sr I	460.7	1	3	$2.01 \cdot 10^8$	2.9	1.6
Na I	589.0	2	4	$6.16 \cdot 10^7$	4.9	3.9
Na I	589.6	2	2	$6.14 \cdot 10^7$	4.9	3.9

The line profile resulting from this model for the Ca I resonance line is shown together with measured data at $t = 55$ ms and $t = 145$ ms in figure 3.14 (a). The model parameters are shown in the middle row of table 3.2. The measured line profile can be reproduced reasonably well using this simple model, though the broadening near the top of the line profile is overestimated in the calculations at $t = 55$ ms.

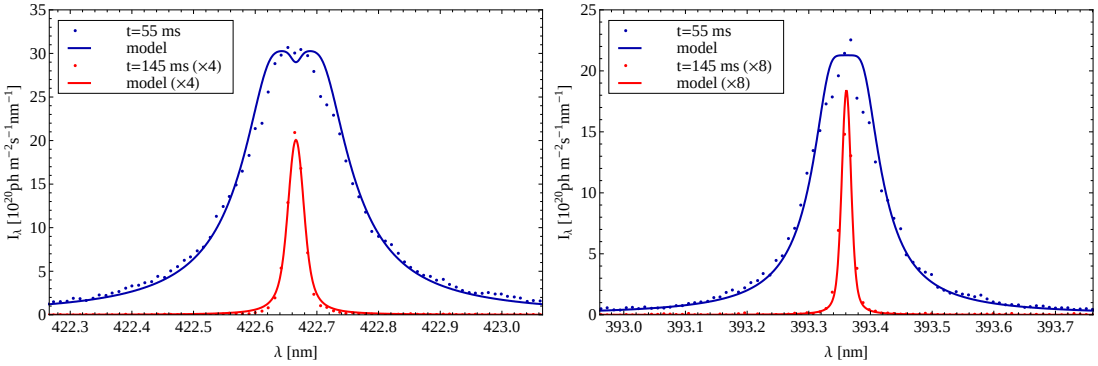

(a) Ca I resonance line. (b) Ca II resonance line.

FIGURE 3.14: *Optically thick calcium atom and ion resonance lines: measurement and calculation at t=55 ms and t=145 ms. The data at t=145 ms has been multiplied by 4 and 8 in (a) and (b) respectively. The model parameters are the same for both resonance lines and given in table 3.2.*

Simulated and measured line profiles for the Ca II and Cu I resonance lines are shown in figures 3.14 (b) and 3.15 respectively. The simulation parameters can be found in table 3.2 again. For the copper lines the same model parameters were used for both lines; the profile was fitted for the line at 324.8 nm. The copper line profiles seem to agree better with measurements than those for Ca I and Ca II. The latter shows similar deviations deviations as for Ca I near the top of the profile. These can partly be attributed to the contributions of neighboring lines (see

Table 3.2: *Parameters used for resonance line simulations fitted to measurements recorded at 1 cm from the ball center using tap water with 0.2 g/l HCl. Listed are: central plasma length and density d_c and n_c, boundary density n_b, center and boundary electron temperature $T_{e,c}$ and $T_{e,b}$. The length (thickness) of the boundary layer was kept fixed at d_b=2 mm.*

	$t = 55$ ms					$t = 145$ ms				
	d_c [cm]	n_c [m^{-3}]	n_b [m^{-3}]	$T_{e,c}$ [K]	$T_{e,b}$ [K]	d_c [cm]	n_c [m^{-3}]	n_b [m^{-3}]	$T_{e,c}$ [K]	$T_{e,b}$ [K]
Cu I	8	$1 \cdot 10^{21}$	$1 \cdot 10^{21}$	3230	2800	12	$1.5 \cdot 10^{20}$	$1.5 \cdot 10^{20}$	2770	2550
Ca I	8	$7 \cdot 10^{19}$	$3 \cdot 10^{17}$	3020	2630	12	$8 \cdot 10^{17}$	$3.5 \cdot 10^{15}$	2800	2400
Ca II	8	$1.8 \cdot 10^{20}$	0	3070	–	12	$8 \cdot 10^{17}$	0	2670	–

figure 3.13) for which no correction was applied. This means the simulation results likely somewhat overestimate the Ca II density at t =55 ms. Note that all experimental data is from the same pair of measurements, so that the densities and temperatures can be compared.

The electron temperatures determined from the resonance line simulations (table 3.2) agree within 200 K, and show a decrease from about 3100 K at $t = 55$ ms to around 2750 K at $t = 145$ ms in the center. The temperatures obtained for the boundary layer for Cu I and Ca I lie 200–400 K below this. Copper has the highest ground state densities; decreasing from approximately $1 \cdot 10^{21}$ m^{-3} at $t = 55$ ms to $1.5 \cdot 10^{20}$ m^{-3} at $t = 145$ ms. The concentration in the center and in the boundary are the same (as the boundary thickness of 2 mm is chosen this way). This decrease in concentration (factor 6.7) is about twice the factor by which the volume of the plasmoid increases (factor 3.4). For both Ca I and Ca II the decrease in concentration is much larger: approximately a factor 100. This may be an indication that atomic calcium is lost via chemical reactions.

Furthermore, there is no self-reversal visible for Ca II, so that the concentration in the boundary seems to be much lower than in the center: $n_b \ll 1 \cdot 10^{17}$ m^{-3} for $t = 55$ ms and $n_b \ll 1 \cdot 10^{15}$ m^{-3} at $t = 55$ ms, suggesting a lower ionization degree in the cooler boundary. The ionization degree of calcium, determined from the values for n_c decreases from 0.7 at $t = 55$ ms to 0.5 at $t = 145$ ms. It is stressed once more that these results depend on the assumption of LTE occupation of the excited states with respect to the ground state, which may not be fulfilled for $t > 145$ ms.

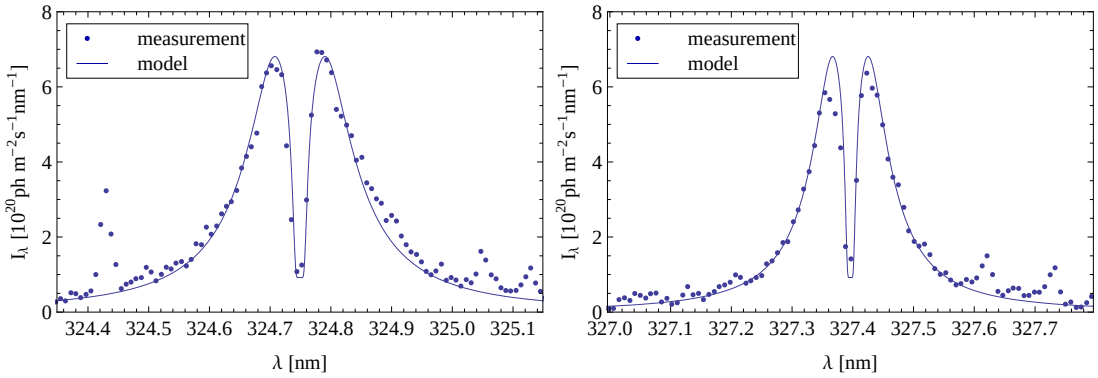

(a) Cu I 324.8 nm, t=55 ms.

(b) Cu I 327.4 nm, t=55 ms.

(c) Cu I 324.8 nm, t=145 ms.

(d) Cu I 327.4 nm, t=145 ms.

FIGURE 3.15: *Measurement and simulation of the optically thick copper resonance lines at t=55 ms and t=145 ms. The model parameters are the same for both resonance lines and given in table 3.2.*

Emission line ratios

Intensity ratios of different spectral lines are commonly used for plasma diagnostics purposes [9, 10]. They are often employed for determining the electron temperature in LTE, which is straightforward for an optically thin plasma. Here this technique is applied to a set of copper lines at 510.6 nm 515.3 nm and 578.2 nm, which can be found in the Grotrian diagram given in figure 3.16. As radiation trapping will turn out to play an important role, their optical thickness is investigated.

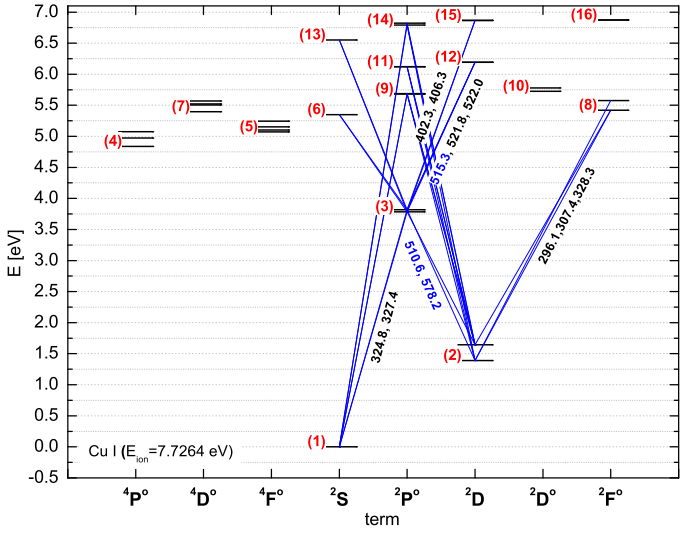

FIGURE 3.16: *Simplified Grotrian diagram for Cu I. Note that not all (optically allowed) transitions are included. Some lines that were used for LTE line-ratio (or Stark broadening) measurements are using blue wavelength values (in nm). Many other lines could not be used because insufficient atomic data is available [15].*

Two transitions $q_1 \rightarrow p_1$ and $q_2 \rightarrow p_2$ are considered. The wavelength-integrated intensity ratio in the optically thin case is obtained simply by substituting the ratio of the Boltzmann populations n_{q1} and n_{q2}, equation (2.32), into the ratio of the line-emission coefficients ϵ_{qp1} and ϵ_{qp2}, equation (2.56):

$$\frac{I_{qp1}}{I_{qp2}} = \frac{\epsilon_{qp1}}{\epsilon_{qp2}} = \frac{g_{q1}}{g_{q2}} \exp\left(\frac{E_{q2} - E_{q1}}{k_\mathrm{B} T_\mathrm{e}}\right) \frac{A_{qp1}}{A_{qp2}} \tag{3.2}$$

This can be solved for T_e and, if the atomic data is available, it can be obtained directly from the line-ratio. In order for this approach to be applicable the excited state densities n_{q1} and n_{q2} must be low enough for absorption to be negligible. In other words, the line-integrated escape factors should be close to one. When a spatially constant emission coefficient is assumed, the latter is given by equation (2.60).

To calculate the line escape factors Θ_L for the copper lines at 510.6 nm, 515.3 nm, and 578.2 nm, the following set of assumptions is used:

- Line broadening is the result of Van der Waals and Doppler broadening. The widths have been estimated using equations (2.68) and (2.69)–(2.71) respectively, again assuming H_2O perturbers and the density of an ideal gas at 2000 K. The Lorentz and Gaussian components obtained are given in the appropriate figure captions. Stark broadening may play a role for the line at 515.3 initially, as will become clear from density measurements later, but this is ignored.

- The emission coefficients are uniform and the effects of a boundary layer are ignored.

- The plasma ball diameter is constant and equal to 8 cm.

- States are populated as in LTE. Excited state densities are obtained from the ground state density n_1 and T_e using the Boltzmann equation (2.32). The consequences of this assumption are discussed in some more detail in section3.4.2

The resulting Θ_L for Cu I 510.6 nm and 515.3 nm are plotted as a function of T_e in figure 3.17, and different values of the ground state density n_1. The expected copper ground state density equals $n_1 = 10^{21}$ m^{-3}, as obtained in the previous section. It is clear that the line at 510.6 nm can suffer from considerable absorption, with an escape factor below 0.5 for $T_\mathrm{e} \gtrsim 3200$ K.

From the definition of the escape factor, the integrated line intensity ratio can be written analogue to equation (3.2):

$$\frac{I_{qp1}}{I_{qp2}} = \frac{g_{q1}}{g_{q2}} \exp\left(\frac{E_{q2} - E_{q1}}{k_\mathrm{B} T_\mathrm{e}}\right) \frac{A_{qp1}}{A_{qp2}} \frac{\Theta_\mathrm{L}^{qp1}}{\Theta_\mathrm{L}^{qp2}} \tag{3.3}$$

Values for this ratio obtained for the line pair 515.3 nm / 510.6 nm are shown in figure 3.18. The ratio for the lines at 515.3 nm / 578.2 nm are shown in figure 3.19. For comparison, the ratio in the optically thin case, as in equation (3.2), is also shown in these figures (dashed lines). The effect of the escape factor is largest for the first line pair, as the line at 510.6 nm has the highest absorption coefficient.

Now that the effect of radiation trapping has been estimated, the calculated line ratios are compared to measurements. A series of measurements recorded with the échelle spectrometer (top view) at different times is considered. The water mixture in the vessel consists of tap water with 0.4 g/l additional $CaCl_2$. This was used as it resulted in strong, bright discharges and enhanced the signal-to-noise ratios. The copper ground state density is assumed to be $n_1 = 10^{21}$ m^{-3}, as obtained in the previous section. All other assumptions are the same as listed above. Although the constant ball diameter is not very realistic, the errors due to this assumption are partly compensated by the decrease of the ground state density. The electron temperatures are then obtained by comparing the measured line ratios with those in figures 3.18 and 3.19 and shown in figure 3.20 for both line pairs (red and blue symbols).

In the same figure, the temperatures obtained when assuming an optically thin plasma are shown (grey symbols). These are not equal for the two line pairs and too high. The use of escape factors makes the result of both line ratios consistent within about 50 K and lowers the temperatures obtained by 500–2000 K. Of course, these results rely on the LTE assumption, which will only be valid above a certain electron density. This lower limit for n_e is estimated using equation (2.46) to be of the order of 10^{20} m^{-3} for the observed transitions. The density may drop below this value for $t > 75$ ms, as will be shown in the next section. Temperatures obtained here for later times need no longer be correct and the increase in temperature seen for $t > 100$ ms may indeed be the consequence of a non-LTE occupation.

Another series of measurements is recorded at the same time $t = 55$ ms but at different radial distances from the central electrode (top view). It should be noted that this measurement uses a different water composition: tap water with 0.2 g/l HCl, like in section 3.4.2. The resulting temperatures (obtained using the same set of assumptions as before) are shown in figure 3.21. The values at $r = 0$ agree with those in figure 3.21. The ball radius is about 6 cm, as visible in figure 3.12. However, the electron temperature drops about 1000 K over a distance of 2 cm. This confirms the existence of a hot core of about half the diameter of the plasmoid, comparable to the structure in figure 3.3. The difference in the order of 200 K between the two line pairs may be due to the wrong assumption of a constant absorption coefficient (*i.e.* ground state density $n_1 = 10^{21}$ m^{-3} and constant line widths). A higher value for n_1 in the center could bring both lines in agreement, at a slightly lower temperature. This was not further investigated.

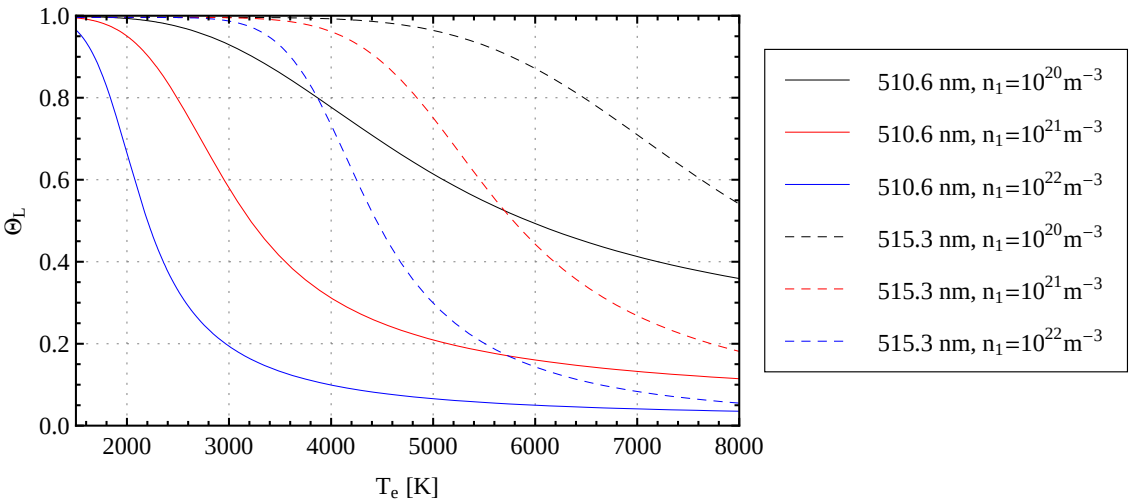

Figure 3.17: *Wavelength integrated line-escape factors at LTE population for copper lines at 510.6 nm and 515.5 nm, at various ground state densities n_1. The ball diameter is kept fixed at d=8 cm and a uniform emission coefficient is assumed. The escape factors have been evaluated using a pseudo-Voigt profile with widths w_L=2.4 pm and w_G=2.0 pm for Cu I 510.6 nm and w_L=6.1 pm and w_G=2.1 pm for Cu I 515.3 nm, estimates of Van der Waals and Doppler broadening respectively at a gas temperature of 2000 K.*

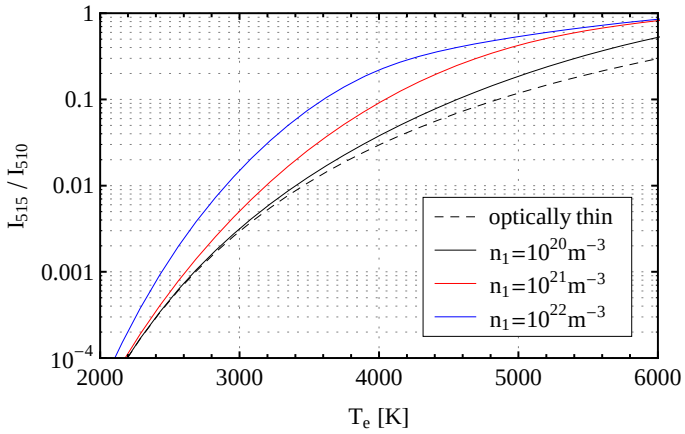

Figure 3.18: *Integrated line intensity ratio for the Cu I 515.3 nm / 510.6 nm line pair. The (dashed) line is the normal LTE line-ratio, determined without using escape factors. For the other three lines, this ratio has been multiplied with the ratio of the escape factors: $\Theta_L^{515}/\Theta_L^{510}$, as shown in figure 3.17, at ground state densities n_1.*

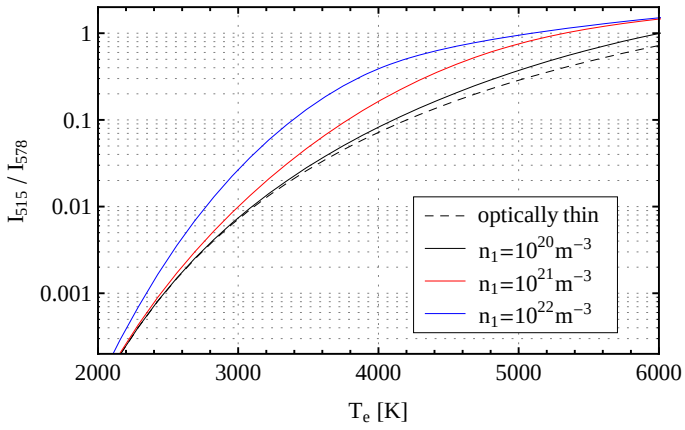

Figure 3.19: *Integrated line intensity ratio for the Cu I 515.3 nm / 578.2 nm line pair. The procedure used is the same as for figure 3.18; for the escape factor evaluation of Cu I 578.2 nm, the Lorentz and Gauss components of the line width are w_L=3.1 pm and w_G=2.3 pm respectively.*

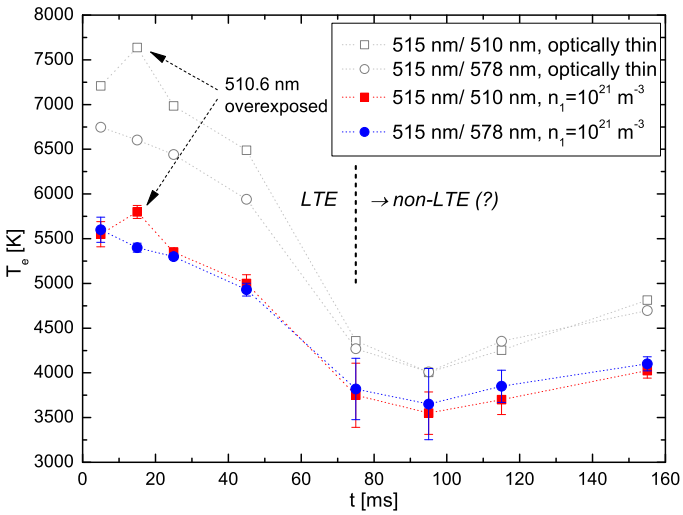

FIGURE 3.20: *Electron temperature determined from measured (integrated) line-ratios of the 510.6 nm / 578.2 nm (red) and 515.3 nm / 578.2 nm (blue) line pairs at different times. The light grey open symbols represent the temperatures obtained when assuming an optically thin plasma. The use of escape factors lowers the measured temperatures and the results of different line-pairs converge.*

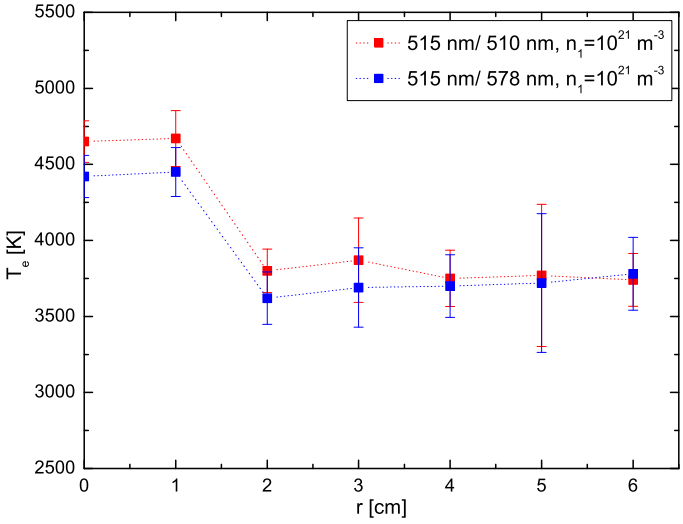

FIGURE 3.21: *Electron temperature determined from measured (integrated) line-ratios of the 510.6 nm / 578.2 nm (red) and 515.3 nm / 578.2 nm (blue) line pairs at different distances from central electrode r (top view) at t=55 ms.*

Initial Phase - Atomic Line Broadening

For $t \lesssim 75$ ms the high charge carrier density causes a measurable broadening in some Stark sensitive lines. Measurements of Stark broadening were conducted using both the échelle spectrometer, for the weak but broad hydrogen H_β (481.1 nm) line as well as using the high-resolution spectrometer for stronger but narrower copper and lithium lines as well as for H_α (656.3 nm). Note that H_α could not be measured using the échelle because its falls in one of the 'blind spots', determined by the optical design of the spectrometer[1] (see figure 3.10). Spectra recorded using the échelle use the top-view again, whereas for the high resolution spectrometer, they were recorded from the side.

An example of Stark broadening is shown in figure 3.22, for H_β. The lower part of this figure clearly shows how the line width rapidly decreases. By fitting the measurement data with a Lorentz profile it is determined that the line width decreases from about 2.3 nm at $t = 5$ ms to less than 0.5 nm at $t = 55$ ms; this is shown in appendix D.

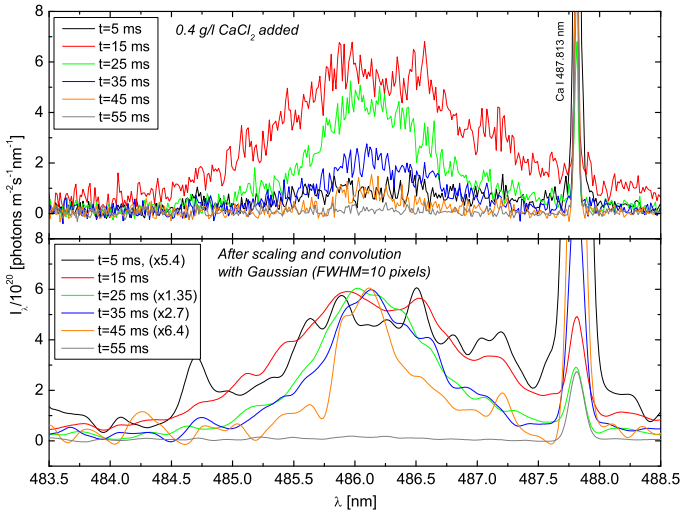

Figure 3.22: *H_β line recorded using the échelle (top view) at various times. In the lower portion of the graph the data has been scaled to the same peak-height and convoluted with a 10 pixel FWHM Gaussian, to visualize the rapid decrease in line width. The original data was fitted to determine the line width (see appendix D).*

Before proceeding to calculate the electron density, the influence of other broadening mechanisms is estimated.

- The apparatus profile has a width of about 25 pm and is neglected.
- Doppler widths for H_β range from 11 pm to 25 pm for gas temperatures between 1000 K and 5000 K. The reference widths used include Doppler broadening at 5000 K [32].
- Van der Waals broadening is calculated again from equations (2.69)–(2.71). For H_2O perturbers between 1000 K and 5000 K and standard pressure this ranges from 41 pm to 13 pm. An average value of 25 pm is subtracted from the measured Lorentz widths.
- Opacity broadening (self absorption) is assessed by calculating the optical thickness τ_λ at LTE occupation, using the same assumptions as for the calculation of Θ_L in section 3.4.2. Even at a hydrogen density of $4 \cdot 10^{24}$ m^{-3} (ideal gas at $T = 2000$ K) and $w_\mathrm{L} = 0.5$ nm, τ_λ remains below 0.01 for $T_\mathrm{e} < 7500$ K (and lower for larger w_L). Thus absorption is neglected.

The reference source [32] for H_β lists line widths (FWHM) at a broad range of electron densities and temperatures between 5000 K and 40,000 K. The table for 5000 K is interpolated and the fitted Lorentz width w_L minus 25 pm was used to directly look up n_e. The resulting densities are plotted in figure 3.23 (green filled circles). The same figure shows the results of another series of

[1] In fact, this is not the case in the standard version of this spectrometer. It was customized in this way for application at the Asdex upgrade experiment at IPP Garching, to prevent overexposure due to the strong H_α emission in the tokamak plasma.

measurements using 0.3 g/l $CaCl_2$ in stead of 0.4 g/l (brown filled diamonds). These results were obtained completely analogously; the fits are also shown in appendix D.

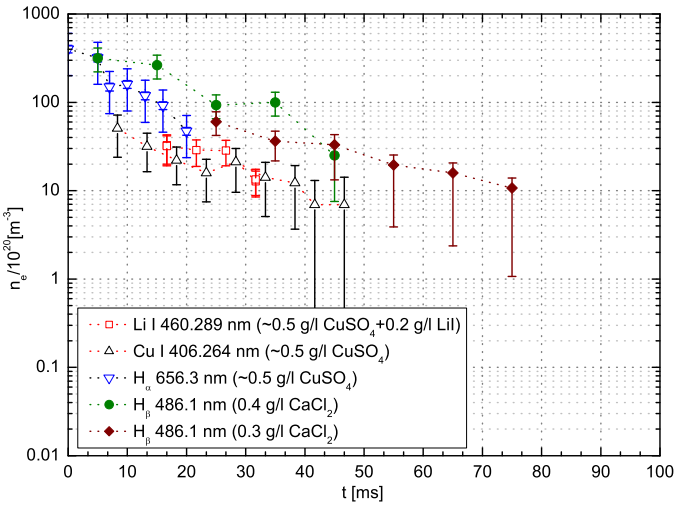

FIGURE 3.23: *Electron density derived from Stark widths w_S of several spectral lines, using various salt additives. The H_β measurements (filled symbols) are recorded from above, using the échelle. All other measurements (open symbols) are recorded from the side, using the high resolution spectrometer.*

Both measurements follow the same trend: an approximately exponential decrease of n_e in time, up to the detection limit. With the higher calcium concentration, the initial densities are higher and it also appears as if the density drops faster in this case. It is likely that this is related to the discharge current development. With more salt, the water conductivity is higher and so is the initial current. As the capacitor discharges faster, the current decrease is faster as well.

Note that the fits in appendix D also indicate a decreasing red shift of the line center λ_0. This shift can also be used to estimate the electron density. A reference shift $d_{ref} = 92.4$ pm at $n_e = 10^{23}$ m^{-3} and $T_e = 7900$ K is given by Griem [56]. Using equation (2.80) for the shift of 8 pm at $t = 15$ ms (0.4 g/l $CaCl_2$), this gives a density of $0.9 \cdot 10^{23}$ m^{-3}, a factor 3 higher than determined from the width. It is likely that this difference is caused by the influence of Van der Waals broadening, with $d_{vdw} = \frac{2}{3} w_{vdw}$ [28]. As shifts are generally harder to measure and less reference data exists, they are not used for any density measurements here.

As the signal-to-noise ratios are low, the fits are not always good and there is a rather large uncertainty in n_e in these results. Also, no information for $T_e > 75$ ms was obtained. Therefore an attempt was made to measure Stark broadening from different spectral lines using the high-resolution spectrometer.

Based on available reference data and observed spectral lines, a number of lines were considered and measured, see tables 2.3, 2.1 and 2.2. Unfortunately the lines with the largest Stark widths were also the weakest, and the sensitivity of the high-resolution spectrometer is much lower than that of the échelle. Measurement results for a Cu I line at 406.3 nm (also see the Grotrian diagram 3.16), with relatively strong Stark broadening, is shown in figure 3.24. Also in this figure is the same line recorded from a CuNe hollow cathode lamp, which is narrower than all measured lines. The measured peaks are fitted with a pseudo-Voigt profile, with a fixed Gaussian width w_G (estimated apparatus width, from the reference lamp) and variable Lorentz width w_L, as indicated in the legend.

To assess the effects of other broadening mechanisms, the Cu I line at 515.3 nm was also measured, as shown in figure 3.25. The Van der Waals and Doppler widths were calculated as a function of gas temperature, assuming constant pressure; see figure 3.26. w_{vdw} was calculated for H_2O as well as N_2 perturbers, the latter giving slightly lower values.

From figures 3.25 and 3.26 it is estimated that $T_g \gtrsim 3000\ K$, for the times considered (20 ms $< t <$ 50 ms) or the measured Lorentz widths of the Cu I line at 515.3 nm should have been larger, due to Van der Waals broadening. It can also be estimated that the effect of Van der Waals broadening is small from the fact that the measured Lorentz widths of 406.3 nm are roughly twice as big as those of Cu I 515.3 nm, like the Stark reference widths in table 2.3. An estimated value

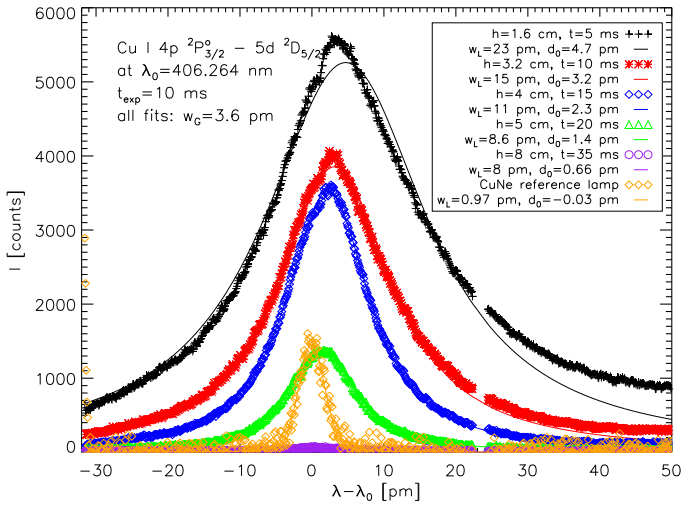

Figure 3.24: *Copper line at 406.3 nm at various heights h above the electrode. The symbols are measured data; the solid lines are fits of a Voigt profile with a Gaussian width $w_G = 3.6$ pm, Lorentz widths w_L and shift d_0 (see legend). The exposure time for all shots is 20 ms, the measurement starting time t is indicated in the legend.*

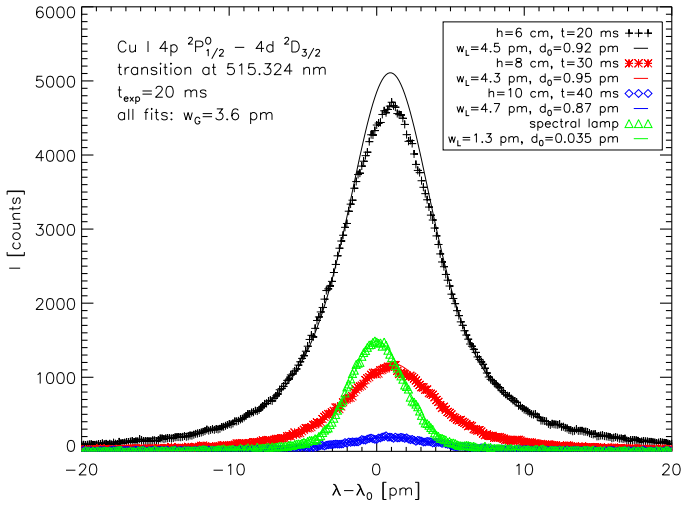

Figure 3.25: *Same as figure 3.24, but now for copper line at 515.3 nm. The exposure time for all shots is 20 ms. The peak of the line at t=20 ms deviates from a Voigt profile, which is a possible sign for self-absorption. Therefore, only the wings of the lines are fitted.*

of (3 ± 2) pm for w_{vdw} is subtracted from the measured w_{L}, to calculate n_{e} using equation (2.79).

The electron densities resulting from the width of Cu I 406.3 nm are shown in figure 3.23, where the height has been converted to time of arrival. Also in this figure are results of measurements of an atomic lithium line at 460.3 (after adding LiI-salt) and H_α. For these lines, reference data from table 2.2 and [32] was used. The results are consistent with the results of Cu I 406.3 nm within the error margins, however the intensities decreased even faster than that of the copper lines so that the measurement range could not be extended. The densities obtained from all these lines lie a factor 2 to 10 below those from H_β, recorded using the échelle from above. An exception is the density determined from of H_α at $h = 0$, $t = 0$. In this measurement, the electrode was in the field of view of the spectrometer, like for the échelle measurements. Thus it is conjectured that during the discharge, there is a large vertical density gradient very close to the electrode.

Spectroscopy - discussion and conclusions

Finally, the most important conclusions that can be drawn from the spectroscopic measurements so far are given. Some remaining points of discussion related to each of them will also be mentioned.

Spectra of the atmospheric plasmoids contain many atomic and ionic lines. All of them can be attributed to species that are present in the water or the electrode material (copper). The atomic lines all belong to species with relatively low lying excited states (< 5 eV).

The presence of CaOH and OH molecular bands indicates that water is dissociated and chem-

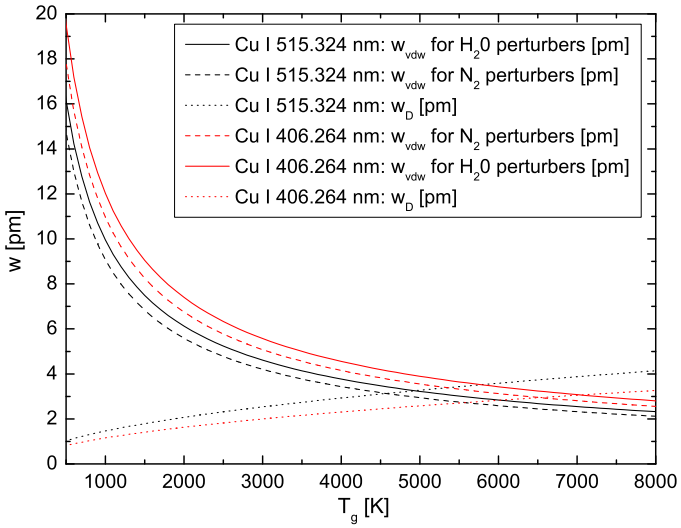

FIGURE 3.26: *Calculated Van der Waals w_{vdw} and Doppler w_{D} (dotted lines) widths of Cu I lines at 515.3 nm and 406.3 nm at atmospheric pressure, depending on gas temperature T_{g}. The perturber density for Van der Waals broadening is calculated from T_{g} using the ideal gas law. w_{vdw} is plotted for both H_2O (solid lines) and N_2 (dashed lines) perturbers; the latter have a larger mass and thus lower w_{vdw}, see equation (2.69).*

ical reactions take place. The overview spectra also show that this molecular radiation is the dominant radiation source in the visible wavelength range during most of the initial phase and in the autonomous phase $t \gtrsim 130$ ms. This topic is further investigated in chapter 5

Estimates of the ground state densities of Cu I, Ca I, and Ca II were obtained from their resonance lines using the solution of the radiation transport equation for a simple two-layer model at $t = 55$ ms and $t = 145$ ms, under the assumption of LTE. A much faster decrease in calcium concentration than that of copper may suggest that calcium is lost via chemical reactions[2]. It follows from quasineutrality that the Ca II ground state concentration can be seen as a lower bound for the electron density. The value for the ground state density $n_1 \approx n_{\mathrm{CaII}} = 1.8 \cdot 10^{20}$ m^{-3} at $t = 55$ ms is indeed in the range of electron densities determined from Stark broadening at this time.

The obtained atomic calcium density can be compared with that in 0.1 g of water from the vessel (see section 3.3.2) dispersed over the volume of the plasmoid. It is assumed that tap water with an average calcium concentration[3] of 2.75 mmol/l is used and that the mole fraction in the vapor is the same as in the liquid. At t=55 ms we have a ball radius of approximately 4.8 cm, resulting in a calcium density:

$$n_{\mathrm{Ca}} = \frac{2.75 \cdot 10^{-3} \cdot N_{\mathrm{A}} \cdot 0.1 \cdot 10^{-3}}{4/3\pi(4.8 \cdot 10^{-2})^3} \approx 3.6 \cdot 10^{20}\ \mathrm{m}^{-3}, \tag{3.4}$$

where $N_{\mathrm{A}} \approx 6.02 \cdot 10^{23}$ is Avogadro's number. This agrees well with the total concentration of Ca I and Ca II of $2.5 \cdot 10^{20}$ m^{-3} at $t = 55$ in table 3.1.

The Stark broadening measurements yield an approximately exponential decrease of electron density $1 \cdot 10^{20}$ m$^{-3} \lesssim n_{\mathrm{e}} \lesssim 5 \cdot 10^{22}$ m^{-3} in the first 75 ms of the discharge. A remarkable feature of figure 3.24, the Stark broadening of Cu I 406.3 nm, is the asymmetry in the line profile at $t = 5$ ms. This may be caused by a narrow and unshifted contribution from the plasma edge, with lower n_e. Another possibility is an ion-broadening effect, that also leads to a higher wing in the direction of the shift [9] (also see paragraph 2.5.2). It is also possible that this is a consequence of a variation of the spectrometer sensitivity over the spectral range, as no correction for this was applied.

Again under LTE assumption, electron temperatures were determined from intensity ratios for two different line pairs of Cu I, giving consistent results when corrected for optical thickness. As

[2]It will be shown in chapter 4 that the calcium ground state density at t=145, is most likely higher than the value obtained here.

[3]Value obtained from the web site of 'Berliner Wasserbetriebe' `http://www.bwb.de/content/language1/html/3255.php`, for the postal code of the HU Berlin Institut für Physik, Arbeitsgruppe Plasmaphysik (PLZ 12487, on November 8th, 2007).

mentioned before, the minimum electron density for the LTE assumption to be justified is in the order of 10^{20} m^{-3}, following from equation (2.46). The results in figure 3.20 can thus be expected to be accurate up to about 75 ms. Note that the effect of Stark broadening on the Cu I line at 515.3 nm was neglected for the escape factor calculation, which used w_{L}=6.1 pm and w_{G}=2.1 pm. Figure 3.25 shows that this in fact overestimates the initial w_{L} by 1–2 pm, presumably due to higher gas temperatures than 2000 K. w_{vdw} is expected to increase at later time though, so that the estimate of 6.1 pm should become better at those times.

The electron temperatures determined from the resonance lines are about 1000 K lower than those determined from the Cu I line ratios. This can be explained by the existence of a radial temperature gradient, like it is shown in figure 3.21. The optical thickness of the resonance lines is so large that the hot core is completely shielded by the surrounding plasma. The temperature determined from absolute resonance line intensities can therefore not give information on the electron temperature in the center of the plasmoids. Of course, this difference in T_{e} shows that the simple two-layer model used for the resonance lines is not realistic. Its results should therefore be used with caution.

Finally a remark is made regarding the ionization balance. It was estimated from table 3.1 that the ionization degree of calcium is 0.7 at $t = 55$ ms. Taking the electron temperature at this time from figure 3.20, $T_{\mathrm{e}} \approx 4400$ K, this agrees perfectly with the calculated ionization fraction in figure 2.2. This suggests that the closed-system approach to calculating the ionization degree is realistic and that calcium may indeed provide a large portion of the ions and thus that the assumption $x = 1$ in section 2.3.1 is justified, at least at $t = 55$ ms.

The equilibrium ionization for a mixture of atoms, positive and possibly negative ions (*e.g.* O^-, Cl^-) was studied in more detail by Fussmann [private communication]. It was found by Fussmann that, for estimated initial concentrations as in tap water, calcium may indeed provide the bulk of the electrons (due to its low ionization energy), for electron temperatures in the range of roughly 2000 K to 5000 K. At higher temperatures, hydrogen is expected to be more important, due to its much higher concentration (in dissociated water, see chapter 5). Negative ions are not expected to play a large role, except maybe at very low temperatures $T_{\mathrm{e}} < 2000$ K, as their binding energies are relatively small.

3.5 Probe measurements

3.5.1 Floating potential and space charge

Single (and double) Langmuir probes used to measure the floating potential (difference) consisted of wires with 0.1 mm diameter and a length of about 2 mm. They were connected to a scope via resistors of 50 MΩ, thus in a nearly floating state. In the initial phase ($I_{\mathrm{dis}} > 0$) single probes show signals reaching up to 200 V. The polarity is positive when applying positive high voltage to the ring electrode and negative for negative high voltage.

As the discharge current reaches zero, the voltage drops sharply to values < 1 V. An example of a floating potential measurement in the autonomous phase is shown in figure 3.27 (a). The polarity is then positive, irrespectively of the polarity of the high voltage. By measuring at several heights the maximum (central) floating potential as a function of time can be deduced. This shows a roughly linear decrease from values around 0.5 V at 250 ms to 0.05 V at 600 ms, as shown in figure 3.27 (b).

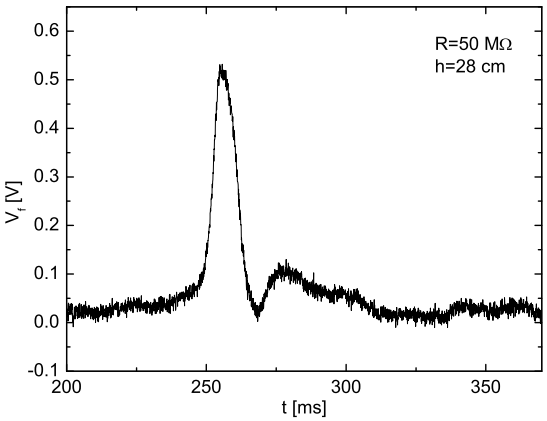

(a) Floating potential in the autonomous phase, as the ball passes through the probe at a height of 28 cm above the electrode.

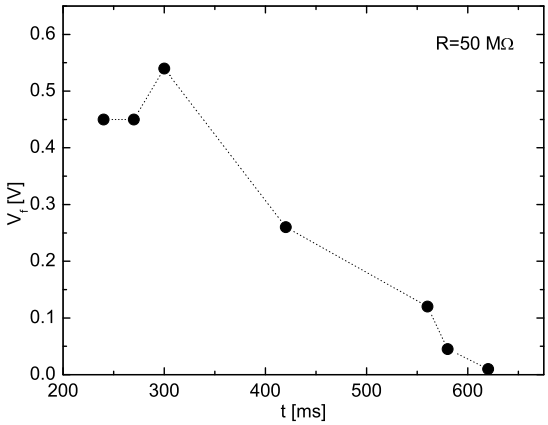

(b) Maximum floating potential at various times in the autonomous phase, measured at different heights above the electrode.

FIGURE 3.27: *Floating potential measurement results, measured using a single probe connected to a scope via 50 MΩ.*

Small double probes at a separation $\Delta z = 0.2$ mm (aligned vertically) were used to measure the floating potential difference ΔV, as pictured schematically in figure 3.28 (a). This showed in some cases sharp peaks with duration < 1 ms, as the rising ball passed through the probes. These peaks can be attributed to electric double layers within the ball or at its boundary. Ignoring gradients in T_{e} on this small scale, the electric field can be obtained from this difference as $E = \Delta V/\Delta x$. This function can be differentiated and converted to $\mathrm{d}E/\mathrm{d}x$ using the known velocity v_{ball} of the ball:

$$\mathrm{d}E/\mathrm{d}x = v_{\mathrm{ball}}^{-1}\mathrm{d}E/\mathrm{d}t. \tag{3.5}$$

The Poisson-equation (2.135) then yields the space charge density $\rho = \varepsilon \mathrm{d}E/\mathrm{d}x$. Figure 3.28 (b) shows the vertical space charge distribution deduced in this way at three different measurement heights, assuming $\varepsilon = \varepsilon_0$.

3.5.2 Other probe measurements

Biased flat approximately square probes with an area of 2.6 cm^2 were used to measure saturation currents in the autonomous phase. At voltages of ± 12 V, current densities in the order of 0.01 to 0.1 Am^{-2} were measured at a height of 18 cm ($t \approx 180$ ms). The currents were found to be lower

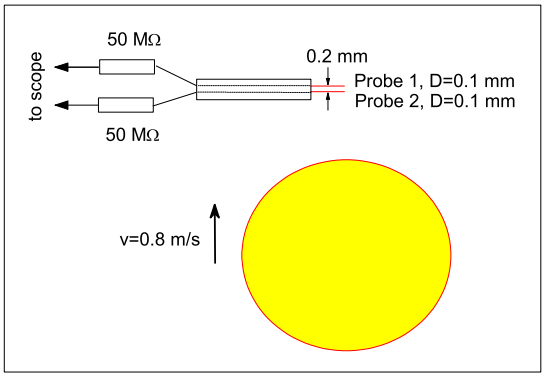

(a) Schematic of the floating potential difference measurements using small double probes.

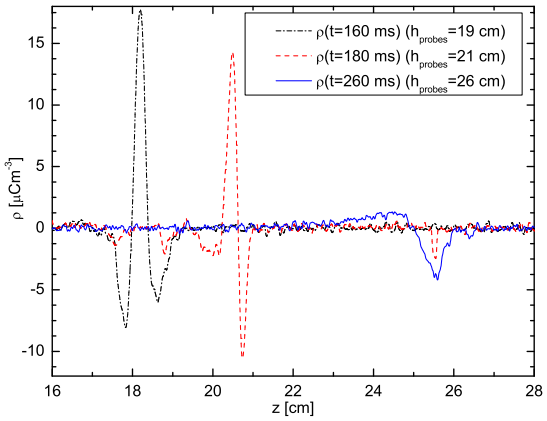

(b) Space charge density as a function of the height z above the electrode at three different times, assuming $\varepsilon = \varepsilon_0$.

Figure 3.28: *The change in the floating potential difference measured by probes at small separation (left), is used to find the variation of the space charge density (right).*

at smaller bias voltages (roughly proportional) with the magnitude of the current depending only weakly on the polarity.

Also in the autonomous phase, sweeping double probes at various distances (in the range of 4–20 mm) show incomplete saturation at voltages in the range of -10 V to 10 V.

Probe measurements - discussion and conclusions

When the collisionless probe theory, *e.g.* equation (2.136) would be applied to the ion saturation current densities mentioned in 3.5.2, densities in the order of 10^{14} m^{-3} to 10^{15} m^{-3} are found (with an estimated mean ion velocity of 1000 ms^{-1}). However, with an estimated neutral density of $7 \cdot 10^{24}$ m-3 (ideal gas density at 1000 K) and collision mean free path of 10^{-5} m, much smaller than the probe dimensions, the transport is determined by collisions with neutrals. This leads to much lower currents than in the collisionless case, as was pointed out in section 2.7.3. Therefore, the currents dot not provide information on the plasma densities directly. The saturation currents were not investigated further.

Because for floating voltage measurements in section 3.5.1 the currents are small neutral collisions (the resistance of the sheath) will have less influence.
Positive floating potentials were measured up to about 650 ms after the discharge current; see figure 3.27 (b). From this figure an estimated lower bound for the electron temperature can be deduced as follows: going back from 600 ms to 300 ms, the voltage increases by about a factor 10. Assuming an approximate proportionality between floating voltage and electron temperature as in the case of non-collisional sheaths, in the beginning the temperature will be at least ten times higher than room temperature, *i.e.* 0.3 eV.
A final remark is made concerning the finite measurement resistance in the floating potential measurements. Though the measuring resistance is high, the probes are not perfectly floating. This results in a deviation of the measured potentials of the true floating potential. The size of this deviation is dependent on the plasma resistance, *i.e.* on the current I_p flowing through the probe, and will be estimated here. The measuring resistance R_m is parallel to the plasma resistance R_p. Thus, the measured voltage difference ΔV_m is:

$$\Delta V_\mathrm{m} = I_\mathrm{p} R_\mathrm{p} \frac{R_\mathrm{m}}{R_\mathrm{m} + R_\mathrm{p}} = \Delta V_\mathrm{f} \frac{R_\mathrm{m}}{R_\mathrm{m} + R_\mathrm{p}}. \tag{3.6}$$

With double probes the resistance R_m in the probe circuit amounts to 100 MΩ. When adding a shunt of 10 MΩ, *i.e.* $R_\mathrm{m} = 9.1$ MΩ, the measured voltage reduces by about a factor 3, yielding $R_\mathrm{p} \approx 25$ MΩ. The floating potential difference is thus given by $\Delta V_\mathrm{f} \approx 1.25 \Delta V_\mathrm{f}$. This correction was applied to all results above.
Concluding, the conducted probe measurements yield data on the plasma potential and the fluctuations therein. In the boundary layer the charge distribution can be characterized as a double layer, with negative charge on the outside; see figure 3.28 (b). At $t = 180$ ms the charge fluctuations occur over a distance of about 1 cm. As the charge distribution is smeared out at later times, the boundary layer is expected to be thinner than 1 cm at earlier times.

Chapter 4

A Collisional Radiative Model for calcium

4.1 Introduction

Many lines of neutral calcium are present in almost all of the recorded spectra, making the element a logical candidate for an attempt to determine plasma parameters from (absolute and relative) line intensities. Spectra recorded with the échelle spectrometer are particularly suitable for this purpose: the spectrometer's resolving power of approximately 20,000 is sufficient to resolve almost all lines, it has a large usable spectral range (300–700 nm) and relatively high sensitivity due to the intensified CCD camera. Since the sensitivity is adjustable by changing the multichannel plate voltage, measurements could be made with good signal to noise ratio throughout a large part of the plasmoid's lifetime.

Without prior knowledge of the electron density from Stark broadening measurements, a first attempt was made to determine the electron temperature T_e by comparison with LTE simulations from NIST [15]. This showed significant deviations in relative intensities of several lines. The assumption was made that the electron density n_e is too low to sustain thermal equilibrium, in particular for the lower energy levels.

Using equation (2.46) one can estimate the minimal electron density for collisional transitions to dominate over radiative. For the lower lying electronic states of Ca I with typical ΔE ranging from 0.3 eV to a few eV (not including transitions between multiplet substates) and the expected electron temperature less than 1 eV, the critical electron densities are in the order of 10^{17}–$10^{21}\mathrm{m}^{-3}$.

Stark broadening measurements have shown that the electron density may drop below 10^{20} for $t > 75$ ms which explains why the LTE simulation fails at this point. A coronal equilibrium may be reached for a large part of the system towards the end of the lifetime. However, it is desired to obtain information on the plasma parameters throughout the lifetime. Moreover, for spectroscopic measurements at $t > 150$ ms it proved difficult to obtain good signal-to-noise ratios, especially for transitions between states higher in the system that do not suffer too much from absorption.

Therefore, an attempt is made to model the radiation production of the bound electrons away from LTE or coronal equilibrium using a collisional radiative model (CRM). This means that all collisional and radiative processes that are considered relevant for the expected plasma parameter ranges need to be taken into account. Using the rate coefficients for these processes the occupation of the excited states (atomic state distribution function, ASDF) is calculated after which the Einstein coefficients for spontaneous emission A are used to calculate the line intensities. Line broadening (due to apparatus profile) is included in the output of the model so results can be directly compared to measured spectra, making data processing relatively easy.

A simplified energy level (Grotrian) diagram for Ca I is shown in figure 4.1. To limit the number of states and transitions in the diagram, states from the same multiplet (*i.e.* states with the same total spin angular momentum quantum number S and total orbital angular momentum

quantum number L, which differ in energy only on account of spin-orbit coupling) are grouped together. As can be seen, the Ca system is relatively complex. The atom has two partially filled shells (with principal quantum numbers 3 and 4) and *e.g.* all triplets with $L > 0$ appear twice, once with the 4s and once with the 3d state occupied. The complexity of the Ca I system, and the resulting difficulty to obtain enough accurate rate coefficients, is one likely reason why no collisional radiative model has been found in literature.

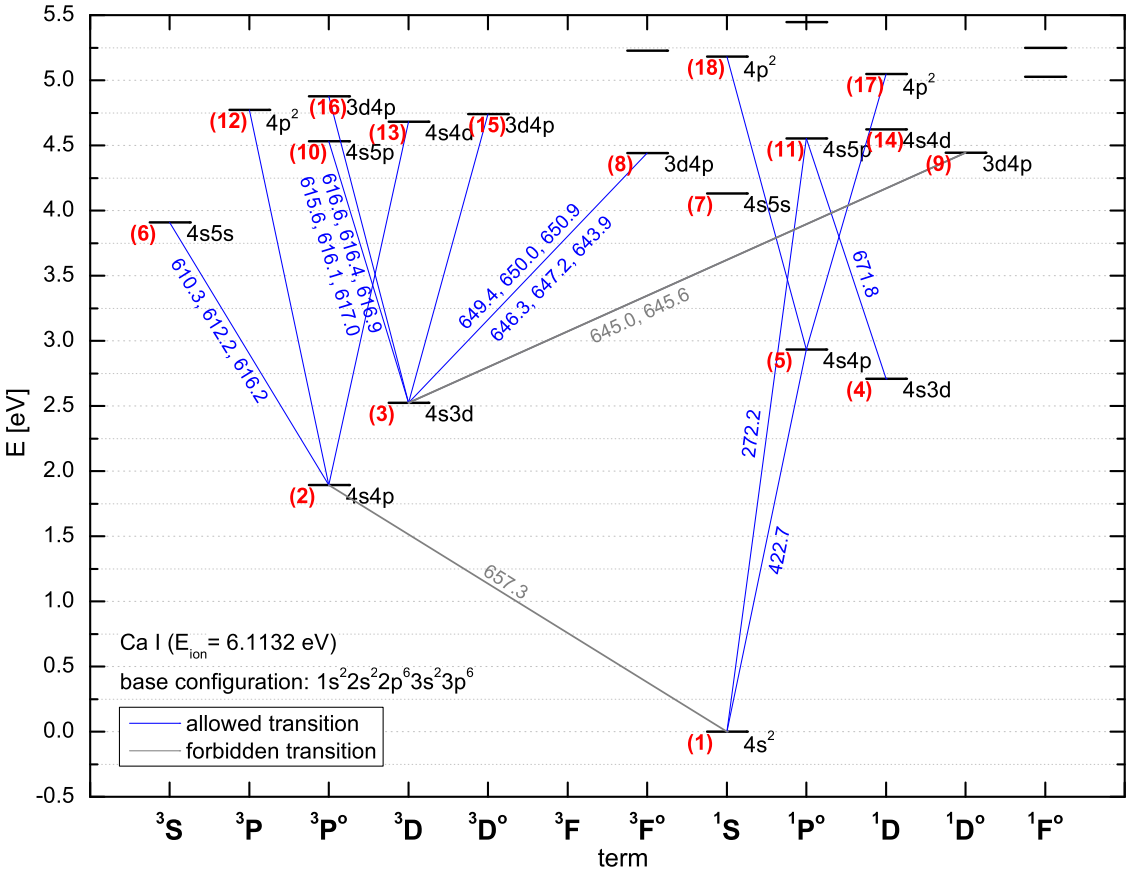

FIGURE 4.1: *Simplified Grotrian diagram for Calcium I. The horizontal ordering is according to the total orbital angular momentum (indicated by S,P,D,F,...) and the total spin (singlet ${}^1X$ for $S = 0$ or triplet ${}^3X$ for $S = 1$) of the two valence electrons in Russel-Saunders coupling. Also, states with even and odd parity are separated (indicated by ° for "odd", the ^{e} for "even" is omitted.). The fine structure is not included in the diagram, e.g. multiplet substates with different J values are grouped together (although they have slightly different energies) as is the case in the implementation of the collisional radiative model. The red labels are the state index numbers used in the CRM. Wavelengths in nm for transitions between the first 11 multiplets are indicated, the others are omitted for clarity.*

4.2 Model description

In the collisional radiative model (CRM), the atomic state distribution function is calculated by equating the rates of all processes leading to increase or decrease of the population, of every state in the system. This leads to a system of first order linear ordinary differential equations. In general this reads [10, 16]:

$$\frac{dn_p}{dt} + \nabla \cdot n_p \vec{w} = S_p, \tag{4.1}$$

where n_p is the density of level p, $\vec{w}$ is the drift velocity and the source term S_p is the net of all production and destruction processes for level p. It can be written as:

$$S_p = P_p - n_p D_p, \tag{4.2}$$

where P_p is the production term and D_p the so-called destruction factor for level p. The processes that make up these terms will be discussed in the following sections. First, a number of simplifications is made:

- It is assumed that the processes that (de)populate the levels are fast with respect to the characteristic transport time. Thus, $\nabla \cdot n_p \vec{w} = 0$ for all levels.
- Similarly, it is assumed the time scale for relaxation to equilibrium between the excited states and the ground stage is very much shorter than the time scale for equilibration of the neutral and ionized stage(s). The validity of this approximation can be verified by comparing the order of magnitude of the rates of ionization/recombination and those of (de)excitation and spontaneous emission. In the solution method, the (calcium) ion density n_+ and the ground state density n_1 are taken as an independent (constant) input parameter. In other words, the ground states of the atom and ion act as large particle reservoirs, that populate the excited states 'instantaneously'. This is called the quasi steady state solution (QSSS) [16].
- Production and destruction due to heavy particle interactions or molecular processes are not considered in detail. Instead, a single collisional quenching rate $K^{\mathrm{Q}}_{p,1}$ [s^{-1}] (scaled with the statistical weight) for all levels will be introduced. Collisional quenching is assumed to cause non-radiative transitions to the ground state only. All other production and destruction processes are due to electron collisions and radiative decay only.
- For population calculations, absorption is only considered for dipole allowed transitions with the ground state as the lower state. In other words, the plasma is assumed to be optically thin for all transitions, except for the resonance line at 422.7 nm, which is known to be optically thick. For the latter, the effect of absorption on the occupations is approximated by means of a population escape factor $\Theta_{\mathrm{P}} < 1$, that effectively decreases the decay probability from A_{q1} to $\Theta^{q1}_{\mathrm{P}} A_{q1}$. For all other transitions, $\Theta^{qp}_{\mathrm{P}} = 1$ is used.
- Stimulated emission and photo-ionization are ignored.
- The number of states in the model is limited to the first 18 multiplets. Transitions to and from all higher lying states are ignored. This approach is only justified if the production from (and destruction to) states above the highest, so-called cut-off level, is small. This need not always be the case as three-particle recombination rates are highest for the states closest to the continuum, which may cause a significant population flow from the highest excited states. This effect of levels above the cut-off level on the populations can be included by means of a cut-off procedure, as discussed in *e.g.* in [16]. Here, no such procedure is used, under the assumption that the contribution from the atomic ground state (direct or indirect, via other excited states) or the direct contribution from the ion stage, to the population of excited states are dominant, for the states that are used for line intensity measurements (*i.e.* the lower states). The collisional quenching by neutrals at atmospheric pressure may be favorable for this assumption. As the atomic radius is roughly inversely proportional to the ionization energy (equation (2.70)) it is expected that the quenching rate increases with state energy and effectively depopulates the highest states.

The following processes are taken into account:

(a) Spontaneous emission between all levels for transitions with known A values

(b) Absorption, for optically allowed transitions from the ground state

(c) Electron impact (de)excitation (to) from the ground state

(d) Collisional (de)excitation from excited states to other excited states

(e) Electron-impact ionization

(f) Three-particle recombination

(g) Radiative recombination.

Processes (c) and (d) are mentioned separately because a different set of rate coefficients is used. As stated before, ionization and recombination are taken into account for the calculation of the excited state populations but not for determining the ionization balance.

Including the processes mentioned above, the production term is given by:

$$P_p = \underbrace{n_e \sum_{q \neq p} n_q K_{qp}}_{\text{(de)exc to}} + \underbrace{\sum_{q>p} n_q \Theta_{\mathrm{P}}^{qp} A_{qp}}_{\text{cascade}} + \underbrace{n_{\mathrm{e}}^2 n_+ K_{+p}^{\mathrm{tpr}}}_{\text{three part. rec.}} + \underbrace{n_{\mathrm{e}} n_+ K_{+p}^{\mathrm{rr}}}_{\text{rad. rec.}} \tag{4.3}$$

and the destruction factor is:

$$D_p = \underbrace{n_{\mathrm{e}} \sum_{q \neq p} K_{pq}}_{\text{(de)exc. from}} + \underbrace{\sum_{q<p} \Theta_{\mathrm{P}}^{pq} A_{pq}}_{\text{sp. emission}} + \underbrace{n_{\mathrm{e}} K_{p+}^{\mathrm{ion}}}_{\text{coll. ion.}} + \underbrace{K_{p,1}^{\mathrm{Q}}}_{\text{quenching}} \quad . \tag{4.4}$$

The term "cascade" is used to indicate production due to radiative decay from higher states [16]. The sources of the various rate coefficients will be discussed in the next section, but first the solution method will be explained.

As mentioned, the model is limited to the first 18 multiplets. This includes 36 substates and 48 radiative transitions. The multiplet substates are grouped together and treated as a single level with a (weighed) average energy $E_p^{\mathrm{avg}} = \sum_J (g_{p,J}/g_{p,\mathrm{tot}}) E_{p,J}$ in the calculation of the population densities. Since the substate energies are close together, the occupation of the individual substates is taken to be proportional to their statistical weight:

$$n_{p,J} = \frac{g_J}{g_{p,\mathrm{tot}}} n_p. \tag{4.5}$$

Since the emission coefficients $A_{qp,J}$ are also given for the individual substates, averaged values must be calculated here, too:

$$A_{qp} = \sum_J \frac{g_{q,J}}{g_{q,\mathrm{tot}}} A_{qp,J}. \tag{4.6}$$

In general, the population escape factor should be replaced by a weighed average value as well. But as $\Theta_{\mathrm{P}}^{pq} A_{pq} = 1$ for all but the (singlet) resonance line, this is not important. A list of of the first 11 states included in the model, and all radiative transitions between them, can be found in table 4.1.

4.2.1 Solution method

With all the assumptions applied, equation (4.1) can be simply written as:

$$P_p - n_p D_p = 0 \quad \text{(for all } p\text{)}, \tag{4.7}$$

The production and destruction term contain linear terms in all n_q, as well as in the ground and ion stage density n_1 and n_+. The latter two will serve as input parameters to the model, so they are taken out of the system of equations. For this, the vector notation $\vec{n}_{\text{exc}} = (n_2, n_3, \dots n_{18})^T$ is introduced to write the system as (also see [16] and the references therein):

$$\mathbf{M}\vec{n}_{\text{exc}} + \vec{\Pi}_1 + \vec{\Pi}_+ = 0 \tag{4.8}$$

where the matrix $\mathbf{M}$ includes coefficients for all transitions to and from other excited states:

$$\mathbf{M}_{pq} = \begin{cases} n_e K_{qp} + \Theta_{pq} A_{\text{P}}^{qp} & (p < q) \\ -D_p = -n_{\text{e}} \sum_{q \neq p} K_{pq} - \sum_{q<p} \Theta_{\text{P}}^{pq} A_{pq} - n_{\text{e}} K_{p+}^{\text{ion}} - K_{p,1}^{\text{Q}} & (p = q) \\ n_e K_{qp} & (p > q) \end{cases} . \tag{4.9}$$

and the vectors $\vec{\Pi}_1$ and $\vec{\Pi}_+$ represent the production from the ground- and ion stage respectively:

$$\vec{\Pi}_1 = n_1 n_e \sum_{1 \neq p} K_{1p} \tag{4.10}$$

$$\vec{\Pi}_+ = n_+ (n_{\text{e}}^2 K_{+p}^{\text{tpr}} + n_{\text{e}} K_{+p}^{\text{rr}}) \tag{4.11}$$

The solution is then simply given by:

$$\vec{n}_{\text{exc}} = \mathbf{M}^{-1}(-\vec{\Pi}_1 - \vec{\Pi}_+). \tag{4.12}$$

Recalling the substates are grouped together in the population calculation, it holds: $n_q = \sum_J g_{q,J} n_{q,J}$. Thus, the number of photons emitted per unit of time and volume for a transition at wavelength $\lambda_{qp,JJ'} = hc/(E_{q,J} - E_{p,J'})$ is finally given by:

$$I_{qp,JJ'} = \frac{g_{q,J}}{g_{q,\text{tot}}} \Theta_{\text{L}}^{qp,JJ'} A_{qp,JJ'} n_q, \tag{4.13}$$

where $\Theta_{\text{L}}^{qp,JJ'}$ is an optional line-escape factor, defined by equation (2.59), that can be used to include the effect of optical thickness on the measured intensity.

Analogue to equation (2.133), the total intensity is given by

$$I_\delta(\lambda) = \sum_{q,p,J,J'} I_{qp,JJ'} \delta_{\lambda\lambda_{qp,JJ'}} \quad \text{with} \quad \delta_{\lambda\lambda_{qp,JJ'}} = \begin{cases} 1 & \text{if } \lambda = \lambda_{qp,JJ'} \\ 0 & \text{if } \lambda \neq \lambda_{qp,JJ'} \end{cases} \tag{4.14}$$

where $\lambda_{qp,JJ'}$ represent the transition wavelengths. Including pseudo-Voigt the line profile $P_{\text{App}}(\lambda)$ due to the apparatus response, the intensity is finally given by:

$$I_\lambda(\lambda) = I_\delta(\lambda) * P_{\text{App}}(\lambda), \tag{4.15}$$

with $*$ the convolution operator. The complete solution method, including the calculation of the rate coefficients, was implemented in `IDL`.

TABLE 4.1: *List of the first 11 multiplets included in the model and radiative transitions (from q, J to p, J') between them. The top line for each index contains the properties of this multiplet. The following lines (if any) contain the parameters of the radiative transitions having one of the substates of this multiplet as its upper level.*

index	state	term	E_q^{avg} [eV]	$\lambda_{qp,JJ'}$ [nm]	J_q	J'_p	$g_{q,J}$	$g_{p,J'}$	$g_{q,\mathrm{tot}}$	$A_{qp,JJ'}$ [s^{-1}]	to index
1	$4s^2$	$1S^e$	0	-	0	-	1	-	1	-	-
2	4s4p	$3P^o$	1.892	-	0,1,2	-	1,3,5	-	9	-	1
				657.278	1	0	3	1	-	2.60E+03	1
3	4s3d	$3D^e$	2.524	-	1,2,3	-	3,5,7	-	15	-	-
4	4s3d	$1D^e$	2.709	-	2	-	5	-	5	-	-
5	4s4p	$1P^o$	2.932	-	1	-	3	-	3	-	1
				422.673	1	0	3	1	-	2.18E+08	1
6	4s5s	$3S^e$	3.91	-	1	-	3	-	3	-	2
				610.272	1	0	3	1	-	9.60E+06	2
				612.222	1	1	3	3	-	2.87E+07	2
				616.217	1	2	3	5	-	4.77E+07	2
7	4s5s	$1S^e$	4.131	-	0	-	1	-	1	-	-
8	3d4p	$3F^o$	4.442	-	2,3,4	-	5,7,9	-	21	-	3
				649.378	2	1	5	3	-	4.40E+07	3
				649.965	2	2	5	5	-	8.10E+06	3
				650.885	2	3	5	7	-	2.40E+05	3
				646.257	3	2	7	5	-	4.70E+07	3
				647.166	3	3	7	7	-	5.90E+06	3
				643.907	4	3	9	7	-	5.30E+07	3
9	3d4p	$1D^o$	4.443	-	2	-	5	-	5	-	3
				644.981	2	1	5	3	-	9.00E+06	3
				645.56	2	2	5	5	-	1.40E+06	3
10	4s5p	$3P^o$	4.533	-	0,1,2	-	1,2,5	-	9	-	3
				616.644	0	1	1	3	-	2.20E+07	3
				616.376	1	1	3	3	-	5.60E+06	3
				616.906	1	2	3	5	-	1.70E+07	3
				615.602	2	1	5	3	-	2.30E+05	3
				616.129	2	2	5	5	-	3.30E+06	3
				616.956	2	3	5	7	-	1.90E+07	3
11	4s5p	$1P^o$	4.554	-	1	-	3	-	3	-	1,4
				272.165	1	0	3	1	-	2.70E+05	1
				671.769	1	2	3	5	-	1.20E+07	4

4.3 CR processes and rate coefficients

4.3.1 Spontaneous emission and absorption

Experimentally determined spontaneous emission coefficients required for process (a) can easily be obtained from NIST [15], be it with sometimes considerable error margin (*e.g.* 60%) especially for the weaker transitions.

Escape factors

The effect of absorption on population is included by means of a population escape factor for the resonance line. The population escape factor for this line depends only on the ground state density n_1 and the line width. Estimates for different n_1 are shown in figure 4.2 (a). The ground state density is estimated to be in the order of $4 \cdot 10^{20}$ m^{-3}, from section 3.4.2. Using the assumptions given in figure 4.2, this results in a population escape factor $\Theta_\mathrm{P} \approx 0.001$ for the resonance line at 422.7 nm. This value was used for all presented results. Also shown in this figure is the population escape factor for a line at 612.3 nm, one of the stronger transitions towards the first excited state. At $n_1 = 10^{20}$ m^{-3} or higher, and $T_\mathrm{e} \gtrsim 3000$ K, this escape factor is also considerably below 1 (for LTE population). Nevertheless, population escape factors for transitions between excited states are not included in the model. This may be partly justified by the fact that when T_e is high (in the initial phase), so is n_e. This reduces Θ_P, due to Stark broadening, which is not considered in the calculation of figure 4.2 (a).

As mentioned, optional line-escape factors, defined by equation (2.59), were added to the model to include the effect of optical thickness on the measured intensity. For the evaluation of the line escape factors in the model, the line width of every spectral line is required. For this, a Lorentz width determined by Van der Waals broadening was assumed initially. The widths $w_\mathrm{L} = w_\mathrm{vdw}$ are calculated as before, using equations (2.69)–(2.71) and assuming H_2O perturbers at a temperature of 2000 K and atmospheric pressure. The obtained values of w_vdw (FWHM) are all in the range of 2 to 15 pm. For the resonance line and the line at 612.3 nm resulting Θ_L are shown in figure 4.2 (b). It appeared that for early times (high n_e), these assumptions results in a severe overestimating of the optical thickness, as Stark broadening is important. Therefore a simple correction factor was applied to the line widths as follows:

$$w_\mathrm{L} = w_\mathrm{vdw}(1 + 1\frac{n_\mathrm{e}}{10^{21}\ \mathrm{m}^{-3}}). \tag{4.16}$$

This estimate is based on the experience that lines with the largest Van der Waals width, are usually also the ones that are most sensitive to Stark broadening. In a more complete model, a better estimate should be used.

4.3.2 Electron impact (de)excitation from the ground state

For process (b), accurate rate coefficients K_{pq}^exc to the first 10 excited states (multiplets $p = 2 \ldots 11$ in figure 4.1) are available in literature. These are the results of quantum mechanical R-matrix calculations, conducted for applications in astronomy. In [57] electron impact excitation cross sections are listed for transitions from ground to the first 10 excited states for incident electron energies < 3 eV. Thermally averaged values are calculated by integrating over a Maxwellian velocity distribution and tabulated in terms of an effective collision strength Υ_{ij} for temperatures in the range of 1000 to 10,000 K (in steps of 1000 K). The excitation rate coefficient is calculated from Υ_{pq} using equation (2.23), with evaluated constants:

$$K_{pq} = K_{pq}^\mathrm{exc} = 8.6291 \cdot 10^{-12} \frac{\Upsilon_{pq}}{g_q\sqrt{T_\mathrm{e}}} \exp(-E_{pq}/k_\mathrm{B}T_\mathrm{e})\ [\mathrm{m}^3\mathrm{s}^{-1}]. \tag{4.17}$$

For the resonance transition $4s^2$–$4s4p\ ^1P$ (one of the rare cases where good experimental data exist) these values are in good agreement with experimentally derived rates [58, 59] and an estimated

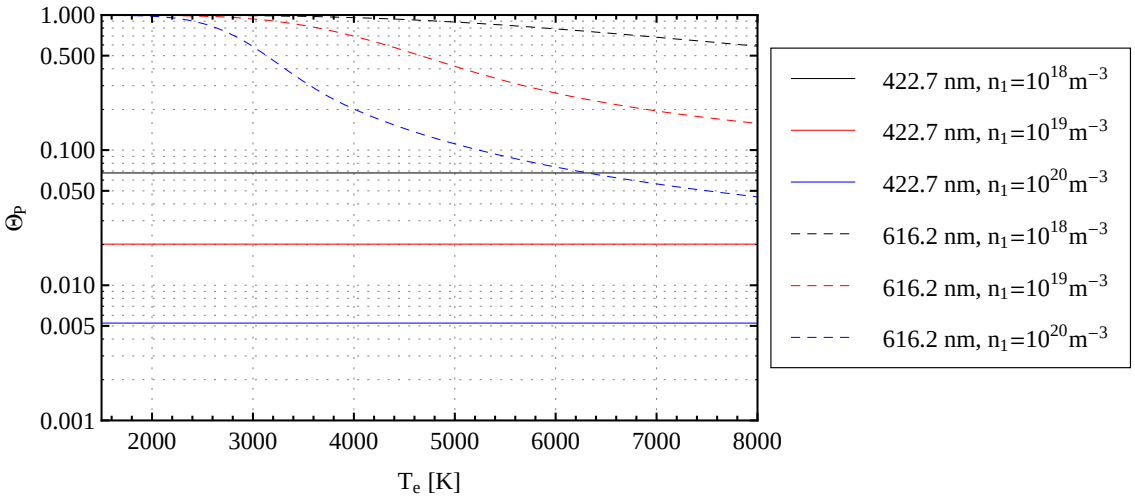

(a) Population escape factors $\Theta_P(r)$. Parameter used: r=5 cm, $w_L = w_{vdw} = 2.4$ pm and $w_G = w_D = 2.1$ pm for Ca I 422.7 nm and $w_L = w_{vdw} = 8.7$ pm and $w_G = w_D = 3.1$ pm for Ca I 616.2 nm.

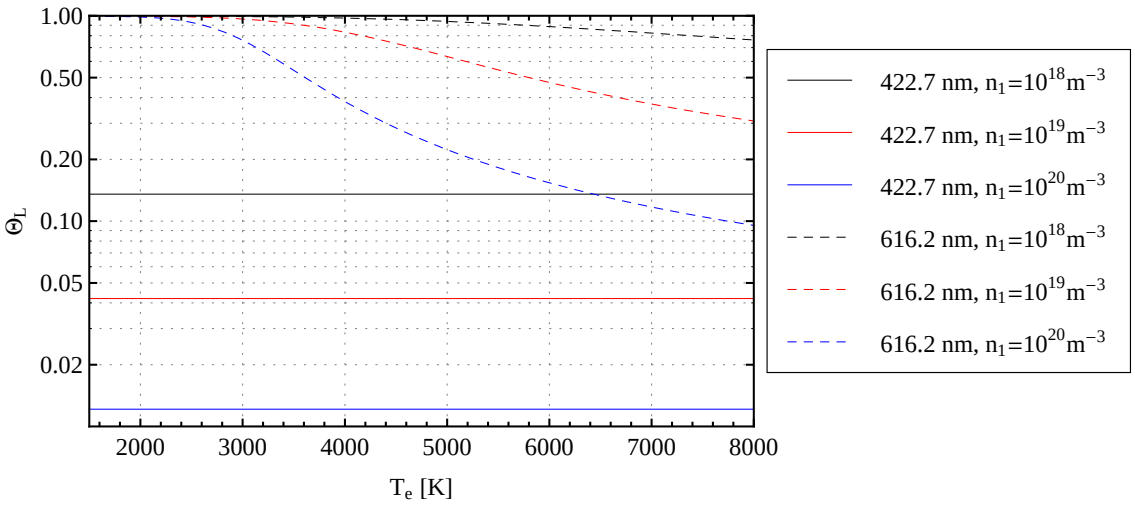

(b) Line escape factors $\Theta_L(d)$. Parameters used: $d = 10$ cm and the line widths as above.

FIGURE 4.2: *Population escape factor and wavelength integrated line-escape factor and at LTE population for calcium lines at 422.7 nm and 616.2 nm, at various (uniform) ground state densities n_1. The escape factors have bee calculated using equations 2.66 and 2.60 respectively. A uniform emission coefficient is assumed. The escape factors have been evaluated using numeric integration of a pseudo-Voigt profile with widths w_L and w_G as indicated near each figure (estimates of Van der Waals and Doppler broadening respectively at a gas temperature of 2000 K). Note the different ranges on the vertical axes.*

accuracy of 5% for the transitions used in this model is reported [57]. For temperatures not listed in the table, linear interpolation of the effective collision strengths is used.

Electron impact deexcitation is the reverse process of excitation and the rate coefficients K_{qp}^{deexc} can be easily calculated using detailed balancing, equation (2.40).

4.3.3 Electron impact (de)excitation between excited states

The three lowest excited states in the calcium system are metastables, that can reach considerable occupations even at relatively low electron temperature and density. The cross section for 'through-excitation' from the metastables is larger than that for excitation from ground, because of the smaller energy difference. Though not directly measurable, their occupation thus influences that of the higher lying states with radiative transitions of interest.

So, the (de)excitation rate coefficients between excited states are an essential ingredient of the model. Application of (2.13) to transitions from these and other low-lying states in the calcium system is not expected to deliver accurate results, especially for the optically forbidden transitions where no oscillator strength data is available.

Another source of effective collision strengths was found with the help of K. Behringer [private communication] in the ADAS (Atomic Data and Analysis System) Superstructure Code [60]. The accuracy in the rate coefficients can not be expected to be better than a factor two for optically allowed or an order of magnitude for the optically forbidden transitions, but values are obtained for transitions between nearly all levels, in a large part of the atomic system. Again, the data is available in tables of effective collision strengths. The same source of collision strengths is also used for transitions from the ground state to the states $p = 12 \ldots 18$, where R-matrix values are also not available.

4.3.4 Electron impact ionization

Ionization rate coefficients $K_{p,+}^{\mathrm{ion}}$ are calculated using equation (2.24). Ionization is most important for the highest states, due to the decrease in χ_p. The accuracy of (2.24) is best for these higher levels where the system is most hydrogen-like.

However, even for the highest state considered in the model ($p = 18$) the ionization rate coefficient is approximately two orders of magnitude smaller than the sum of the rate coefficients for deexcitation to lower states $K_{p,\mathrm{tot}}^{\mathrm{deexc}}$ in the temperature range considered. This is shown in figure 4.3, which also includes the spontaneous emission rate for level 18. The conclusion is that, although it is included for completeness, the effect of ionization on the occupation distribution is small in the expected temperature range.

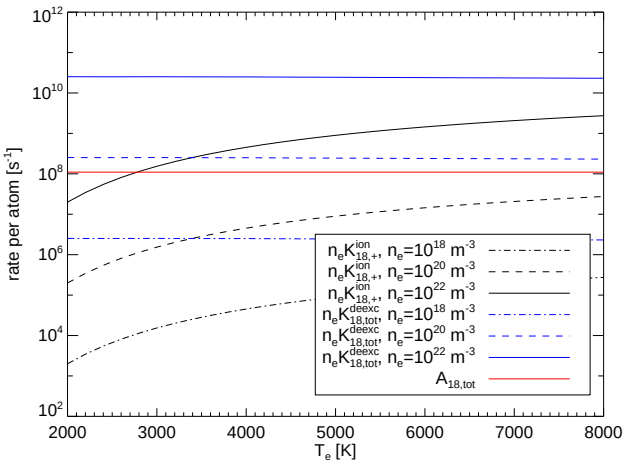

FIGURE 4.3: *Comparison of ionization, deexcitation and spontaneous emission rates (per excited atom) from the highest level considered in the model (p=18) at different electron densities. For $n_e \ll 10^{20}$ m^{-3} spontaneous emission is the dominant depopulating process for this level, for $n_e \gg 10^{20}$ m^{-3} this is electron impact deexcitation.*

4.3.5 Three-particle recombination

Three-particle recombination rate coefficients are calculated from the ionization rate coefficients using equation (2.42). The total rate (per atom) at which recombination occurs is $n_+ n_e^2 K_{+p}$, where $n_+ \approx n_{+,0}$ is the ion ground state density. The quadratic dependence on n_e ensures that in the limit of high n_e this process will be the dominant recombination process (for atomic ions). The rate rapidly decreases with increasing χ_p so the effect will be noticeable first (and only) for the highest states. Due to the fact that the deexcitation rate is higher than the ionization rate, even for the highest level considered here, Saha-equilibrium (or pLSE) is never reached in the model.

4.3.6 Radiative recombination

Figure 2.3 suggests that radiative recombination (or 'capture') may be more important than three-particle recombination for $n_e < 10^{22}$ and $T_e > 2000$ K. Therefore, accurate rate coefficients K^{rr}_{+p} for this process were sought. The values used are those tabulated in literature [20], using the appropriate values n_p and l_p for each state. The tabulation uses a scaled temperature $\Theta = T_e/Z^2_{eff}$ and listed are values of $K^{rr}_{+,nl}/Z_{eff}$. Here, Z_{eff} is the effective ion charge which is approximated by:

$$Z_{eff} = \left(Z' - \left[\frac{Z_C - Z_I}{2} \right] \left[\frac{\eta' - 1}{\eta' + 1 + 3l} \right] \right) \exp(-0.05[l-1]^2), \tag{4.18}$$

where

$$Z' = \frac{Z_C + Z_I}{2} \quad \text{and} \quad \eta' = \frac{Z'}{\tilde{k}_e}. \tag{4.19}$$

$Z_C = 20$ is the core charge, $Z_I = 1$ is the ion charge and $\tilde{k}_e$ is the electron momentum in Rydberg units: $\tilde{k}_e = \sqrt{E^{kin}_e/R_y}$, with E^{kin}_e/R_y the electron kinetic energy, also in Rydberg, which is approximated by $E^{kin}_e/R_y \approx 1.5 k_B T_e/R_y$ (the expression for Z_{eff} is only mildly dependent on $\tilde{k}_e$ [20]). Values of Z_{eff} vary between 1.5 and 2.5 and are highest for the lowest states and at high temperature (in which cases the shielding of the core is least effective). To obtain values at temperatures not listed in the table, linear interpolation is used.

The obtained rate coefficients $K^{rr}_{+,nl}$ are distributed over the individual states (singlet and triplet) according to their statistical weight. This gives: $K^{rr}_{+p} = \frac{3}{4} K^{rr}_{+,nl}$ for triplet and $K^{rr}_{+p} = \frac{1}{4} K^{rr}_{+,nl}$ for singlet states, except for S-terms in which case $K^{rr}_{+p} = \frac{1}{2} K^{rr}_{+,nl}$ for both singlet and triplet. For states with more than one electron outside the 4s state (indices $p = 8, 9, 12, 15, 15, 16, 17$ and 18 in figure 4.1) the radiative recombination coefficient was set to zero since it is assumed that these can not be accessed by capture of an electron by a ground state ion (with a single electron in the 4s state).

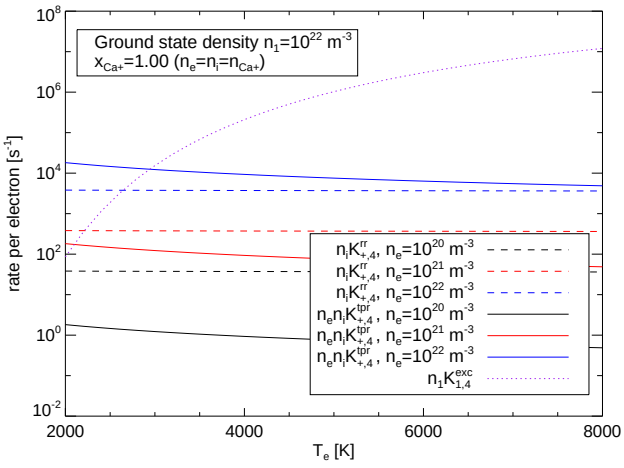

FIGURE 4.4: *Comparison of the rates (per free electron) for three-particle recombination and for radiative recombination at various electron densities ($n_i = n_e$ is assumed) to level $p = 4$. Three-particle recombination becomes the dominant recombination process with increasing n_e first at the highest levels. Also indicated is the rate of excitation from the ground state at a ground state density of 10^{22} m^{-3} (dotted lines). For the lower levels, this is usually the most important populating process.*

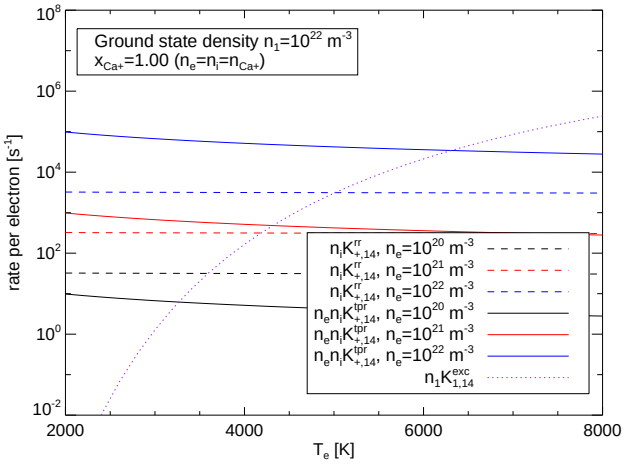

FIGURE 4.5: *Same as figure 4.4, but now for the higher level $p = 14$. The radiative recombination rates are about the same, but the three-particle recombination has increased.*

Figures 4.4 and 4.5 show a comparison of the radiative recombination and three-particle recombination rates for both a state that is low in the system ($p = 4$) and one that is higher ($p = 14$), in the expected temperature range at different electron densities ($n_e = n_+$ is assumed here). Also included are the rates for excitation from the ground state to these levels. It is clear that for the lower level, population from the ground state dominates both recombination processes, except for very high electron densities and low temperatures. The rate for three-particle recombination is small since it decreases rapidly with the ionization potential χ_p.

For the higher level, figure 4.5, radiative recombination may become an important populating process in case $n_e < 10^{21}$ m^{-3}. For higher electron densities, three-particle recombination is dominant, because of its n_e^2 dependence. It is important to notice that (de)excitation from other excited states, which is not included in this figure (because it depends on the populations) is often more important than direct excitation from the ground state. Therefore, and because at lower n_e the ion density is usually lower as well, it is estimated that the effect of radiative recombination is small in most cases.

4.4 Input parameters

As discussed in the previous section, the model relies on a set of atomic data such as energy levels, rate coefficients, etc. Apart from these 'fixed' quantities or functions, the basic input parameters, that depend on the plasma conditions, are the atomic and ion ground state densities n_1 and n_+ as well as the electron density n_e and temperature T_e. For n_1, values between 10^{20} m^{-3} and 10^{21} m^{-3} are used, depending on the experimental conditions.

A calculation of the ionization balance, *i.e.* a relation between n_1, n_+, n_e and T_e is not part of the model. However, a proportionality between the electron and ion densities is assumed: $n_+ = x_{Ca+} n_e$. In most cases $x_{Ca+} = 1$ is assumed.

Additionally, a collisional quenching rate is introduced, as mentioned. The number of non-radiative transitions to the ground state due to quenching is calculated as:

$$K_{q,1}^{Q}\ [\mathrm{s}^{-1}] = g_{q,\mathrm{tot}} k_Q \tag{4.20}$$

with $k_Q = 3.3 \cdot 10^5$ s^{-1} for all multiplets, which will be called the quenching rate from now on. This value is based on a rate $K_{2,1}^{Q} = 3 \cdot 10^6$ s^{-1} ($g_{2,\mathrm{tot}} = 9$) for quenching of the 4s4p ^{3}P^o metastable state by N_2, as reported in [61], assuming atmospheric pressure and $T_g \approx 2000$ K. The quenching rate it is most relevant for the metastable states, of which the spontaneous decay rate is smaller than k_Q.

Depending on whether optical thickness is considered, the plasma length along the line of sight l_p enter ins the expression for the line escape factors Θ_L (see section 2.5.1).

4.5 Results

The model has developed from simple to relatively complex and to present every aspect of the final product here is impossible. The number of parameter in the model allows for an endless amount of variations. At the same time, there are probably not enough parameters to accurately model the plasmoids emission during every stage of its lifetime, so no perfect agreement between measurement and simulation should be expected.

The first results presented show the working of the model and demonstrate the influence of the various parameters on the atomic state distribution function (ASDF). After this, a comparison between measured and simulated line intensity ratios is made. At the end of this section, measured and simulated spectra are compared.

4.5.1 Population

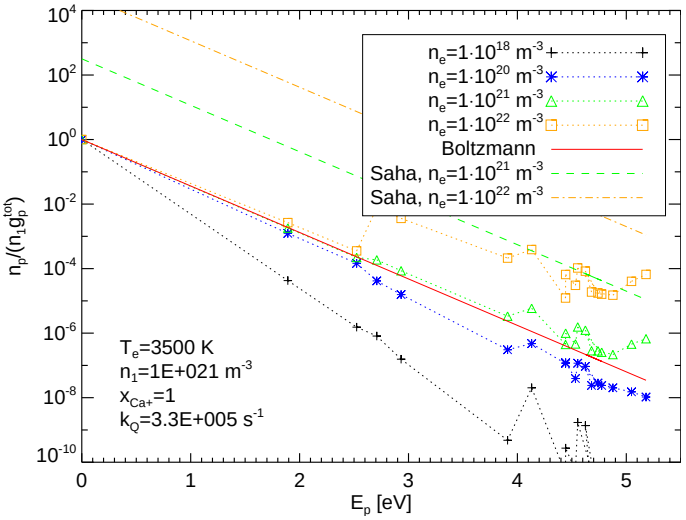

FIGURE 4.6: *Ca I excited state density divided by statistical weight as a function of the state energy ('Boltzmann plot') at various electron densities. $T_e = 4000$ K and the quenching rate is kept constant at $k_Q = 3.3 \cdot 10^5$ s^{-1} for all levels. The red solid line is the distribution calculated from a simple Boltzmann equilibrium with the ground state: $n_p/n_1 = g_p/g_1 \exp(E_p/k_B T_e)$. The dashed lines indicate the population in Saha equilibrium with the ion stage, according to equation (2.34).*

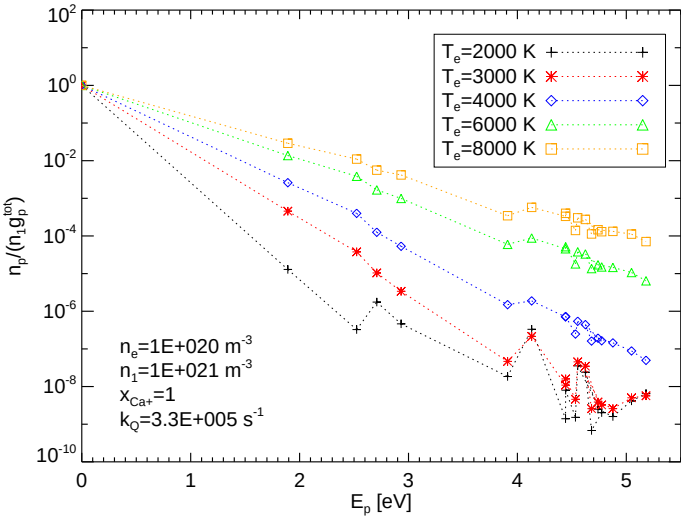

FIGURE 4.7: *Like figure 4.6, but for various electron temperatures. The fixed parameters are shown in the lower left corner.*

The effect of n_e, T_e and k_Q on the calculated ASDF is shown by means of a set of Boltzmann plots, in which the excited state density (relative to the ground state density), divided by the total statistical weight $g_{q,\mathrm{tot}}$ (see table 4.1), is plotted as a function of the state energy.

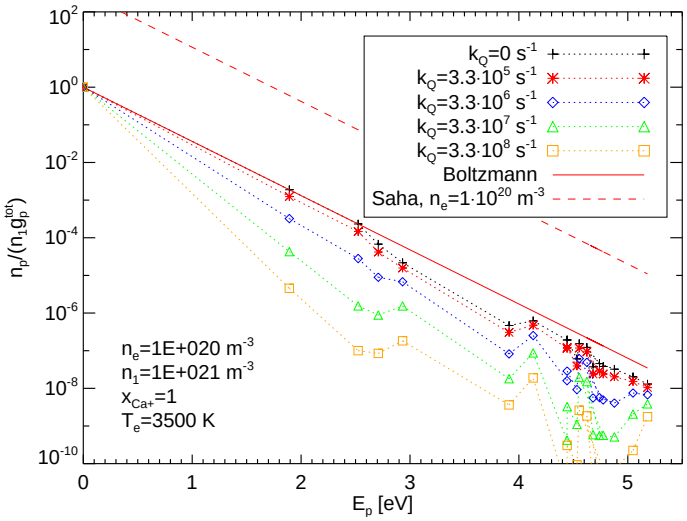

FIGURE 4.8: *Like figure 4.6, but for various values of the (collisional) quenching rate k_Q. The effect of quenching becomes noticeable in the occupation distribution only above a certain rate, at which quenching starts to dominate over electron impact deexcitation and/or spontaneous emission.*

In figure 4.6 this is shown for various values of the electron density, at a fixed electron temperatures $T_e = 4000$ K, quenching rate $k_Q = 3.3 \cdot 10^5$ s^{-1} and ground state density $1 \cdot 10^{21}$ m^{-3}. These fixed parameters are also shown in the box in the left hand corner of the figure and will not be mentioned for following results. The data points connected by the dotted lines are the output of the CRM, including all processes described in section 4.3. The ion ground state density is depending on n_e by $n_+ = x_{Ca+} n_e$, where $x_{Ca+} = 1$ is used, as indicated in the figure.

The solid red line is the so-called 'Boltzmann line' which indicates the population in Boltzmann equilibrium with the ground state, calculated using equation (2.32). The dashed lines are the 'Saha lines' for $n_e = 10^{21}$ m^{-3} (green) and $n_e = 10^{21}$ m^{-3} (yellow), giving the population for Saha-equilibrium with the ion ground state, equation (2.34).

Starting at a low value, an increasing n_e first leads to the ASDF approaching the Boltzmann line. Significant deviations from LTE can be seen below $n_e = 10^{20}$ m^{-3}, mainly due to the different (de)excitation cross sections and radiative lifetimes.

When n_e (and thus n_+) is comparable to the ground state density, the contribution of the ion stage becomes important for the higher levels, and their population can exceed the Boltzmann population. Ultimately the ASDF will approach the Saha line, but this is not reached for the parameters used here.

Figures 4.7 and 4.8 show Boltzmann plots using various values of T_e and k_Q respectively. As expected, a higher T_e leads to a higher population of excited sates in general. In this figure, $n_e = 10^{21}$ m^{-3} is used and the ion stage contribution is relatively unimportant, except for very low temperatures. The temperature changes the slope of the Boltzmann and Saha lines (not shown here) and lowers the Saha line (at constant ion density, due to the $T_e^{-3/2}$ dependence in the Saha equation). The effect of quenching (figure 4.8) becomes noticeable in the distribution only above a certain rate, at which quenching starts to dominate over electron impact deexcitation and/or spontaneous emission.

4.5.2 Line intensity ratios

For comparing with experiments (as well as for testing the model), integrated line intensity ratios are a convenient tool. In general, the ratios depend not only on n_e and T_e, but also on the quenching rate k_Q. This is demonstrated in figure 4.9, for at pair of lines at 616.2 nm and at 643.9 nm, which are lines that are relatively sensitive to changes in the electron temperature and density, and have sufficient intensity for measurements. This figure shows the ratio of the wavelength integrated intensity as a function of n_e and T_e, without quenching (left) and with a quenching rate $k_Q = 3.3 \cdot 10^5$ s^{-1}. It is clear that quenching has an important effect on the line ratio in the displayed parameter ranges. Only at high electron densities $n_e > 10^{22}$ m^{-3} the ratio

is unaffected by the collisional quenching. It should be noted that line escape factors were not used, *i.e.* the transitions are assumed to be optically thin.

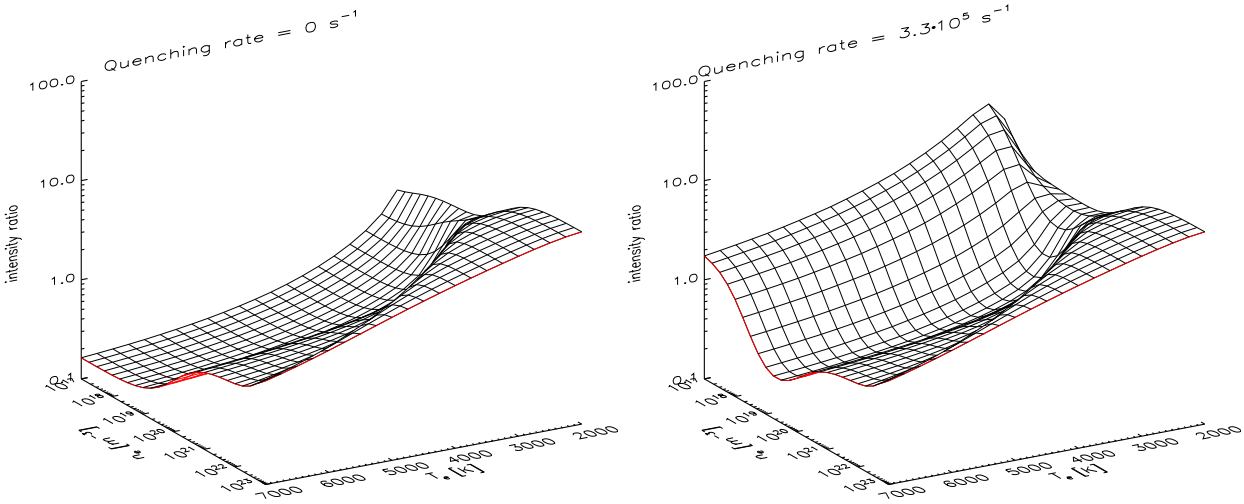

FIGURE 4.9: *Temperature and density sensitive line ratio I(λ=616.2 nm)/I(λ=643.9 nm) ∝ n_6/n_8 with (right) and without quenching ($n_1 = 1.0 \cdot 10^{21}$ s^{-1}, $x_{Ca+} = 1.0$). Only at high electron densities $n_e > 10^{22}$ m^{-3} the ratio is unaffected by the quenching at a rate of $3.3 \cdot 10^5$ s^{-1}. An optically thin plasma is assumed ($\Theta_L = 1$).*

A comparison with measurements is made in figure 4.10, where again $\Theta_L = 1$ is used, as well as a quenching rate of $k_Q = 8 \cdot 10^5$ s^{-1}. The figure contains the calculated line intensity ratio for the previous line pair (a), as well as for 616.2 nm and 527.0 nm (b). The measured data is determined from spectra recorded using the échelle (top view, $r = 0$, at various times) for a series of shots with 0.4 g/l $CaCl_2$ in tap water. For the first four data points, the intensity was measured from the broadening of H_β in the same spectra (see figure 3.23, so the electron temperature can be directly read from the graph. It decreases from just over $T_e = 5500$ K (not shown) at $t = 5$ ms to 4500 K at $t = 45$ ms, determined from the 616.2 nm / 643.9 nm line pair (a) and about 500 K higher from line pair (b). At later times, the measured line ratios are consistent with an electron electron density decreasing at a rate of roughly one decade per 60 ms. The electron temperature is also found to decrease. At $t = 155$ ms, T_e is estimated to be close to 3000 K, at later times the ratios are relatively insensitive to the temperature. It should be noted that the consistency of the line ratios depends on the value assumed for the quenching rate. To get the best agreement, the value of k_Q was adjusted to $8 \cdot 10^5$ s^{-1}, as compared to $3.3 \cdot 10^5$ s^{-1} used for other results presented here. For completeness, the same comparison is shown using $k_Q = 3.3 \cdot 10^5$ s^{-1} in appendix E.

It should be mentioned that the assumption $x_{Ca+} = 1$ is likely not realistic initially. At temperatures above 5000 K, other species (such as atomic hydrogen) will reach a considerable ionization degree and are expected to provide the bulk of the electrons [Fussmann, private communication].

Nevertheless, the same agreement between measurement and simulation is not obtained when the ion-stage contribution (*i.e.* three-particle- and radiative recombination) to the ASDF is neglected. Line ratios obtained in the latter case are shown in figure 4.11, using the same set of parameters as in figure 4.10.

As stated before, line escape factors were were not used for the calculation of the line ratios so far. When values of Θ_L, calculated using $l_p = 8$ cm and the estimated line widths according to equation (4.16) are included, the ratios become somewhat different, as is visible in figure 4.12. The line ratios are higher at intermediate n_e and high T_e, due to stronger absorption of the line at 616.2 nm (also see figure caption). In the limit of high n_e an increase of the line-ratio occurs that is a consequence of the assumption $x_{Ca+} = 1$. The lower state of the lines at 527.0 nm and

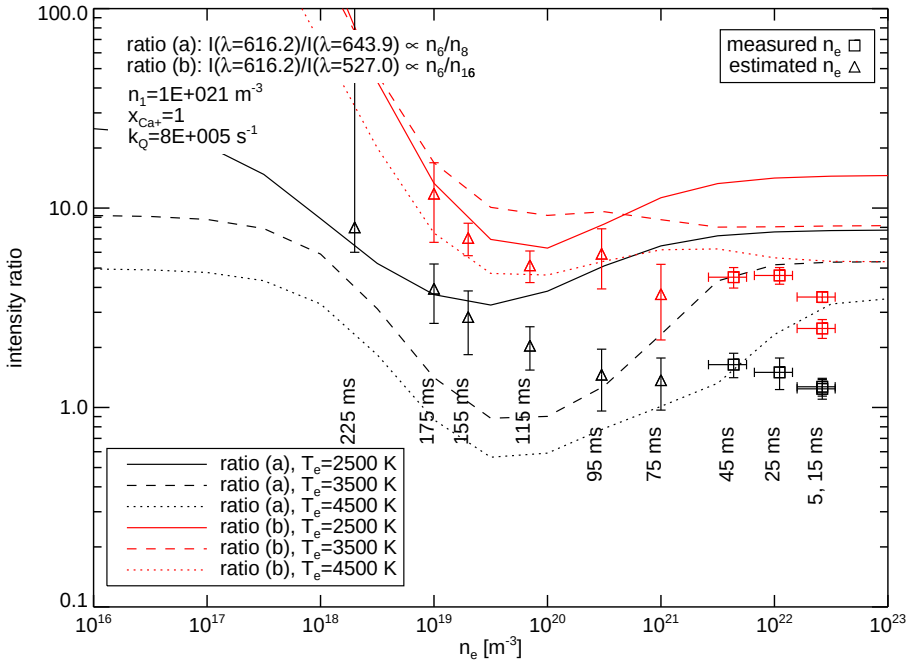

FIGURE 4.10: *This graph shows the calculated line ratios of two line pairs, with a relatively large difference in upper level energy (see the top-left legend and the Grotrian diagram in figure 4.1). As a consequence, the line ratios are relatively temperature sensitive. Also included in the graphs are measured line ratios, determined from spectra recorded using the échelle spectrometer (top view) at different times t after triggering the discharge (indicated by the text labels near the data points, the exposure time is between 1 and 6 ms.). For the first four points (squares) the density has been measured, using Stark broadening of the H_β line in the same spectra. The horizontal error bars indicate the measurement error in the Stark broadening measurements. For the other shots (triangles) the density could not be measured and the horizontal placement is estimated from the calculated and measured line ratios. The measured points clearly indicate that quenching is important (compare with figure 4.9). Although overall agreement is good, some small inconsistencies can be seen between the temperatures determined using ratios labeled (a) and (b). Line escape factors were not used and the other simulation parameter are shown in the top-left corner.*

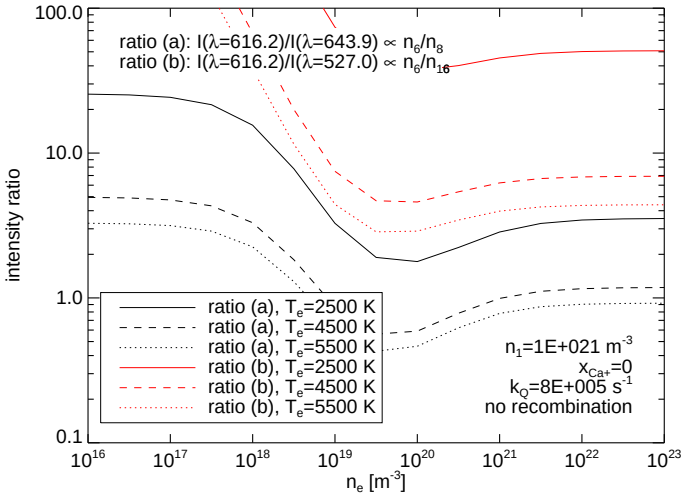

FIGURE 4.11: *Same line ratio as in figure 4.10, but with no contribution from the ion stage to the ASDF. Ratio (b) is higher by a factor 1 to 3, with respect to figure 4.10. This can be understood by the fact that the upper level of the line at 527.0 nm ($q = 16$) has a higher energy than that of the line at 643.9 nm ($q = 8$). The ion stage gives the highest contribution to the population of the states that are closest to the continuum (also see the Boltzmann plots).*

643.9 nm ($p = 3$) shows an increase of its population relative to $p = 2$ (the lower state of the line at 616.2 nm) due to recombination. That such an increase is not shown in the measurements is likely explained by $x_{\mathrm{Ca+}} \ll 1$ initially, as was discussed before. Also, the line widths due to Stark broadening, estimated using equation (4.16) may be too low, resulting in overestimating of the optical thickness at high n_{e}.

FIGURE 4.12: *Same line ratio as in figure 4.10, but with line escape factors included. The lines at 527.0 nm and 643.9 nm share the same lower state ($p = 3$) whereas 616.2 is a transition to the lower state $p = 2$. At most (intermediate) values of n_e and T_e, the line ratios decrease, due to the larger population of the lower state $p = 2$. In the limit of low density and temperature, the effect of absorption becomes negligible, whereas for low T_e and high density ($n_e \gtrsim 10^{21}$ m^{-3}), the line ratios increase as the state with $p = 3$ is more strongly populated due to recombination. The latter is a consequence of the assumption $n_e = n_{\mathrm{Ca+}}$ and most likely not realistic for the plasmoid in it's initial phase.*

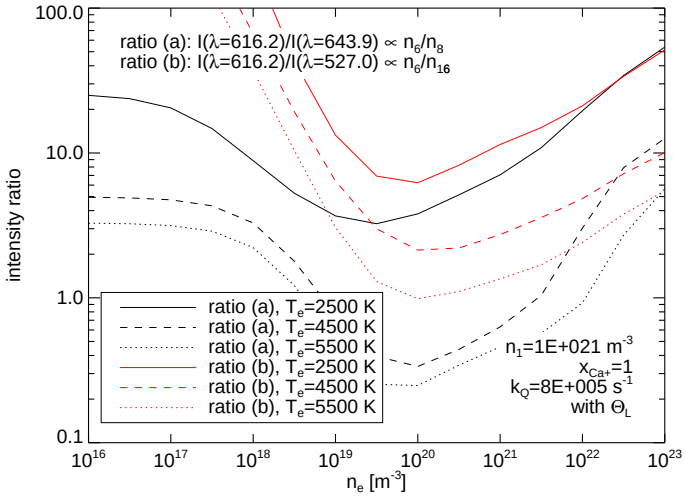

4.5.3 Measured and simulated spectra

Graphs containing (parts of) simulated and measured spectra are shown in figures 4.13, 4.14, as well as in appendix E, in figures E.2 to E.5. The spectral lines included in the model are indicated by their wavelengths above the spectra. Simulation parameters are shown in the box at the top-left corner of the page and measurement parameters in the legends. The initially estimated value for the quenching rate $k_{\mathrm{Q}} = 3.3 \cdot 10^5$ s^{-1} is used. It is important to note that the measured intensities (using the échelle spectrometer) are absolute; giving additional information, as compared to the line ratios.

Line broadening in the simulated spectra is due to the apparatus profile of the échelle spectrometer, which is approximated by a pseudo-Voigt profile with $w_{\mathrm{V}} = \lambda_0/18,000$ and $w_{\mathrm{G}} = 4w_{\mathrm{L}}$, where λ_0 is the transition wavelength.

Line escape factors Θ_{L} are used, calculated using optical path length l_{p} as indicated in each legend and (Lorentz) line widths according to equation (4.16). Figures 4.13, 4.14 also include the simulation results obtained when $\Theta_{\mathrm{L}} = 1$ is used for all transitions. Optical thickness is important for most transitions for $t \lesssim 100$ ms.

In the initial phase, *e.g.* at $t = 75$ ms, $r = 0$ in figure 4.13 or at $t = 55$ ms, $r = 0$ (figure E.2) or $r = 3$ (figure E.3), the signal-to-noise ratios are high and the agreement of measurement and simulation is generally very good, *i.e.* within 50 % for nearly all lines. In some cases (*e.g.* for the line at 430.3 nm at $t = 55$ ms), a deviation of line width due to optical thickness (only *line-integrated* escape factors are included) or Stark broadening can be seen, and as a consequence the simulated line is too high.

At later times, measurement and simulation are less consistent and only the stronger lines can be matched unambiguously to those in the measured spectra. Finally, the electron densities, temperatures and ground state densities obtained from compared spectra are summarized in table 4.2.

measurement		simulation			
t	r [cm]	n_1 [m^{-3}]	n_e [m^{-3}]	T_e [K]	l_p [cm]
55	0	$1.5 \cdot 10^{21}$	$5.0 \cdot 10^{21}$	4500	5
55	3	$1.5 \cdot 10^{21}$	$4.0 \cdot 10^{21}$	3600	5
75	0	$1.1 \cdot 10^{21}$	$2.0 \cdot 10^{21}$	3900	8
95	0	$5 \cdot 10^{20}$	$2.5 \cdot 10^{20}$	3100	10
155	0	$5 \cdot 10^{20}$	$1.6 \cdot 10^{20}$	2500	12
145	3	$5 \cdot 10^{20}$	$1.0 \cdot 10^{20}$	2400	11

Table 4.2: *Simulation parameters used for the simulated spectra, shown in figures 4.13, 4.14, and E.2–E.5.*

4.6 Discussion and conclusions

The results obtained for n_e and T_e agree well with those previously obtained in section 3.4.2. Particularly the electron temperatures at $r = 0$ for $t \lesssim 75$ ms are consistent with those determined from the Cu I lines and LTE assumption in figure 3.20. Also the electron temperature of 3600 K at $r = 3$ cm and $t = 55$ ms is the same as in figure 3.21.

As opposed to the Cu I LTE line-ratios in figure 3.21, the simulated Ca I spectra indicate a further decrease of T_e for $t > 75$ ms, down to about 2500 K at $t = 155$ ms, in the autonomous phase. This confirms that the values obtained from the Cu I lines are indeed incorrect at later times. Is must be noted however, that the values in table 4.2 for $t = 95$ ms, 145 ms and 155 ms have a considerable error margins, *i.e.* about 50 % for the densities and 500 K for the temperatures is estimated.

The estimated electron densities obtained from the line ratios in figure 4.10 are higher initially and decrease faster than those in table 4.2. It is important to note however, that different sets of measurement data are used: as mentioned, the data in figure 4.10 uses 0.4 g/l $CaCl_2$, whereas the comparison of measured and simulated spectra is done using 0.2 g/l HCl in tap water. The reason that a different data set is used for comparing the spectra, is that a lower light amplification (MCP voltage) was used for the experiments with added $CaCl_2$, to prevent overexposure of the strong calcium resonance lines. As a consequence, many of the weaker lines can not be resolved well.

Overall, the values of n_e obtained from the simulated spectra in the initial phase are consistent within an order of magnitude with those measured from Stark broadening, in figure 3.23. A noteworthy result of both the line-ratios in figure 4.10 and of the spectrum simulations in figures 4.14 and E.5, is that $n_e \gtrsim 10^{20}$ at $t \approx 150$ ms, so in the autonomous phase.

In contrast to the Ca I resonance line measurements of section 3.4.2, the results of the collisional radiative model do not indicate that the ground state density decreases faster than expected from the plasmoids expansion. Rather, the densities in the order of 10^{20} m^{-3} are needed to achieve the measured intensities at reasonable values for n_e and reproduce the measured relative line intensities (insofar these could be measured). It is likely that the calcium density at $t = 145$ ms in table 3.2 is incorrect, due to wrongfully assuming an LTE population of the resonance state in that section.

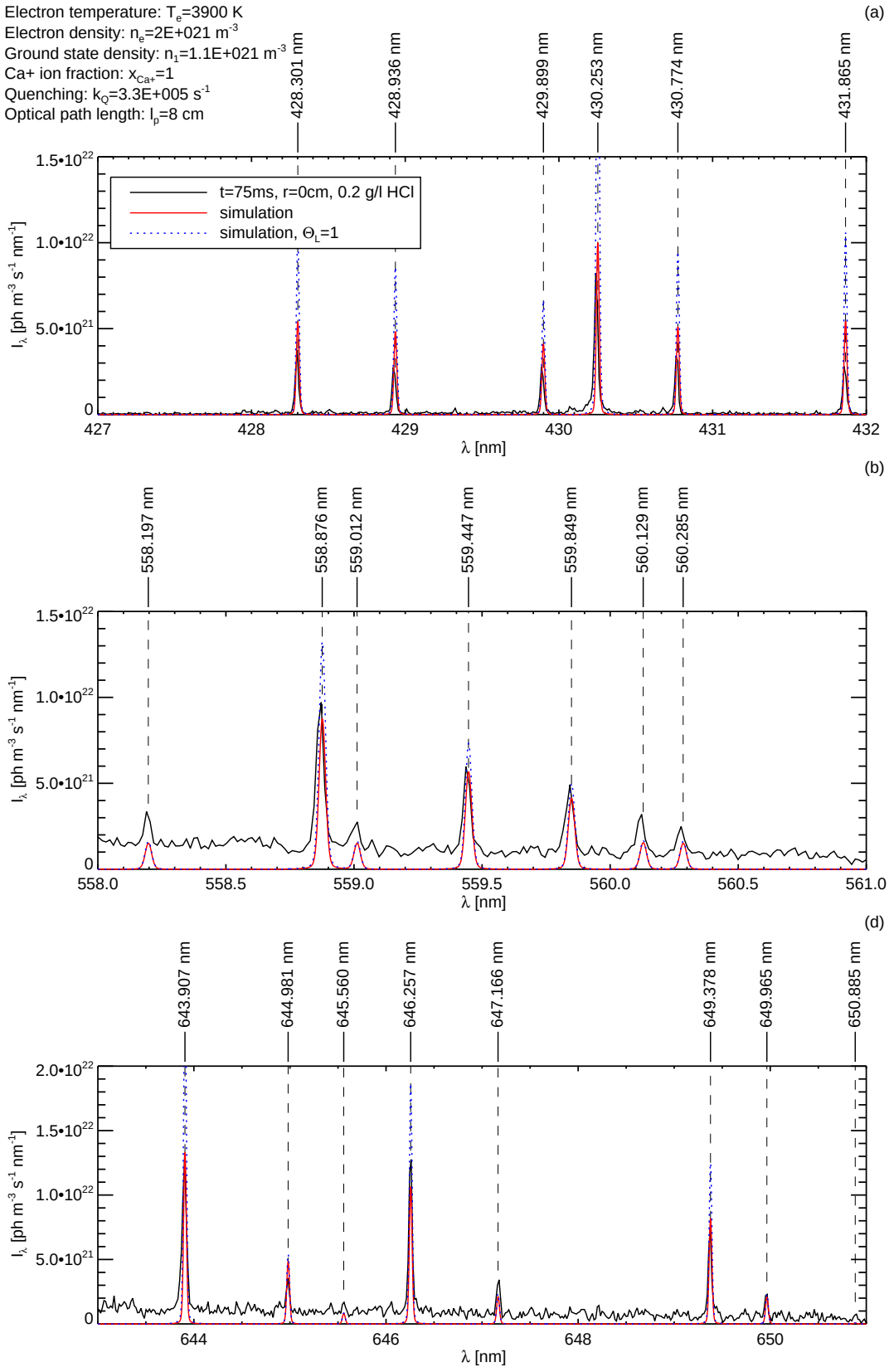

FIGURE 4.13: *Measured and simulated calcium emission spectrum. The measured spectrum was recorded at $r = 0$ and t=75 ms (top view). The simulation parameters are shown in the top left corner. The measured and simulated spectrum fit very well (also for transitions not shown here). Also shown is the simulation results when an optically thin plasma is assumed (blue dots).*

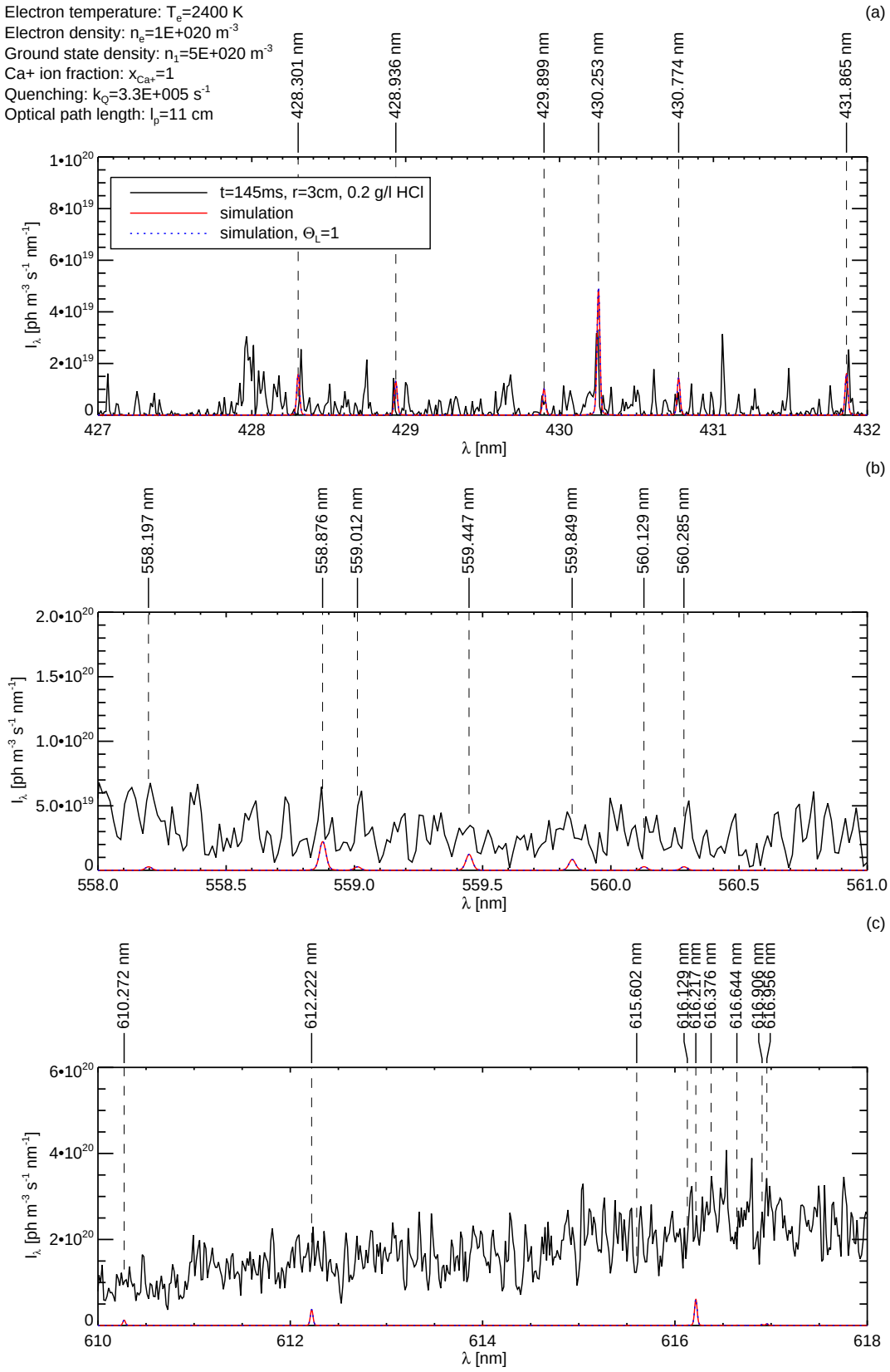

Figure 4.14: *Measured and simulated calcium emission spectrum. The measured spectrum was recorded away from the electrode at $r = 3$ and t=145 ms (top view). Also shown is the simulation result when an optically thin plasma is assumed (blue dots). Optical thickness does not play a role here.*

Chapter 5

Molecules

This chapter consists of three smaller parts, each dealing with molecular processes in a different way. The first part studies the dissociation of water, using the theory of chemical equilibrium and relates this to thermodynamic properties of the plasmoid via a simple model. The second section describes spectroscopic measurements on molecular bands and makes comparison with other experiments in literature. Also the vibrational distribution of OH is estimated from simulations. The part section deals with the measurements of the rotational temperature (and rotational distribution) of the OH band with its head at 306.4 nm.

5.1 Chemical composition and thermodynamics

The model presented here consists of two parts. The first part calculates the chemical composition of (partly dissociated) water as a function of temperature. The second part uses the outcomes of the first part, as well as some of the calorimetry results, in a simple model that calculates the enthalpy and some other thermodynamic properties of the plasmoid.

5.1.1 Chemical equilibrium model

When gaseous water is heated to a temperature $T > 1000$ K it will eventually (partly) dissociate. The degree of dissociation depends on T and can be calculated using the theory of chemical equilibrium introduced in section 2.6.1.

The number of possible reactions involving H_2O and its dissociation products is very large. An extensive list, including temperature dependent rate coefficients for many of these, can be found in [44]. Here the situation is greatly simplified and only the following reactions are considered:

$$\begin{aligned} H_2O &\rightleftharpoons OH + H && (5.1)\\ OH &\rightleftharpoons O + H && (5.2)\\ 2H &\rightleftharpoons H_2 && (5.3)\\ 2O &\rightleftharpoons O_2. && (5.4) \end{aligned}$$

The equilibrium equations are defined as in equation (2.124):

$$K_{\mathrm{r},i} = \left(\frac{T}{T_0}\right)^{f_{\mathrm{r}i}} \exp\left[-\frac{G_{\mathrm{r}i} + (T - T_0)\,(f_{\mathrm{r}i}R - S_{\mathrm{r}i})}{RT}\right] = \left(\frac{T}{T_0}\right)^{f_{\mathrm{r}i}} \exp\left[-\frac{G_{\mathrm{r}i} + (T - T_0)\,(f_{\mathrm{r}i}R - (H_{\mathrm{r}i} - G_{\mathrm{r}1})/\,T_0)}{RT}\right] \quad \text{for } (1 \le i \le 4) \quad (5.5)$$

with the reaction constants and the "reaction degrees of freedom" according to equations (2.109) and (2.112) respectively:

$$K_{\mathrm{r1}} = \frac{x_{\mathrm{OH}} x_{\mathrm{H}}}{x_{\mathrm{H2O}}} \quad , \quad f_{\mathrm{r1}} = 2 \tag{5.6}$$

$$K_{\mathrm{r2}} = \frac{x_{\mathrm{O}} x_{\mathrm{H}}}{x_{\mathrm{OH}}} \quad , \quad f_{\mathrm{r2}} = 3/2 \tag{5.7}$$

$$K_{\mathrm{r3}} = \frac{x_{\mathrm{O2}}}{(x_{\mathrm{O}})^2} \quad , \quad f_{\mathrm{r3}} = -3/2 \tag{5.8}$$

$$K_{\mathrm{r4}} = \frac{x_{\mathrm{H2}}}{(x_{\mathrm{H}})^2} \quad , \quad f_{\mathrm{r4}} = -3/2. \tag{5.9}$$

The concentrations and the mole fractions are:

$$\begin{array}{lcl} n_{\mathrm{H2O}} = 1 - \xi_{\mathrm{r1}} & , & x_{\mathrm{H2O}} = n_{\mathrm{H2O}}/n_{\mathrm{tot}} \\ n_{\mathrm{OH}} = \xi_{\mathrm{r1}} - \xi_{\mathrm{r2}} & , & x_{\mathrm{OH}} = n_{\mathrm{OH}}/n_{\mathrm{tot}} \\ n_{\mathrm{H}} = \xi_{\mathrm{r1}} + \xi_{\mathrm{r2}} - 2\xi_{\mathrm{r3}} & , & x_{\mathrm{H}} = n_{\mathrm{H}}/n_{\mathrm{tot}} \\ n_{\mathrm{O}} = \xi_{\mathrm{r2}} - 2\xi_{\mathrm{r4}} & , & x_{\mathrm{O}} = n_{\mathrm{O}}/n_{\mathrm{tot}} \\ n_{\mathrm{H2}} = \xi_{\mathrm{r3}} & , & x_{\mathrm{H2}} = n_{\mathrm{H2}}/n_{\mathrm{tot}} \\ n_{\mathrm{O2}} = \xi_{\mathrm{r4}} & , & x_{\mathrm{O2}} = n_{\mathrm{O2}}/n_{\mathrm{tot}}, \end{array} \tag{5.10}$$

with ξ_{r1} the extent of reaction (5.1), etc. and with:

$$n_{\mathrm{tot}} = n_{\mathrm{H2O}} + n_{\mathrm{OH}} + n_{\mathrm{H}} + n_{\mathrm{O}} + n_{\mathrm{H2}} + n_{\mathrm{O2}}. \tag{5.11}$$

The reaction enthalpies and Gibbs energies are given by:

$$G_{\mathrm{r1}} = G_{\mathrm{OH}} + G_{\mathrm{H}} - G_{\mathrm{H2O}} \tag{5.12}$$

$$H_{\mathrm{r1}} = H_{\mathrm{OH}} + H_{\mathrm{H}} - H_{\mathrm{H2O}}, \tag{5.13}$$

etc. The standard formation enthalpies and Gibbs energies for the molecules are given in [45]. The following values are used:

$$\begin{array}{lcl} G_{\mathrm{H2O}} = -228.6 \cdot 10^3 \text{ J/mol} & , & H_{\mathrm{H2O}} = -241.8 \cdot 10^3 \text{ J/mol} \\ G_{\mathrm{O}} = 231.7 \cdot 10^3 \text{ J/mol} & , & H_{\mathrm{O}} = 249.2 \cdot 10^3 \text{ J/mol} \\ G_{\mathrm{H}} = 203.2 \cdot 10^3 \text{ J/mol} & , & H_{\mathrm{H}} = 218.0 \cdot 10^3 \text{ J/mol} \\ G_{\mathrm{OH}} = 34.2 \cdot 10^3 \text{ J/mol} & , & H_{\mathrm{OH}} = 39.0 \cdot 10^3 \text{ J/mol} \\ G_{\mathrm{H2}} = 0 & , & H_{\mathrm{H2}} = 0 \\ G_{\mathrm{O2}} = 0 & , & H_{\mathrm{O2}} = 0. \end{array} \tag{5.14}$$

At given T, equations (5.6)–(5.9), with equations (5.10) and (5.11) substituted, form a system of four polynomial equations in four variables $(\xi_{\mathrm{r1}} \ldots \xi_{\mathrm{r4}})$. This system can be solved numerically, giving four complex solutions, one of which is real.

5.1.2 Results of the chemical equilibrium model

The solution procedure was implemented using `Mathematica` software. The resulting mole fractions in thermal equilibrium at temperature T and standard pressure are shown in figure 5.1. The model shows that a transition from almost no dissociation to almost complete dissociation takes place between about 2000 K and 4000 K. Molecular OH, H_2 and O_2 reach their maximum mole fraction at about 3200 K. At $T > 4000$ K only atomic O and H remain.

5.1.3 Thermodynamical model

In the following, the thermodynamic properties of the plasmoid are considered and related to the chemical composition, as well as the work delivered to the plasmoid by the discharge. This part

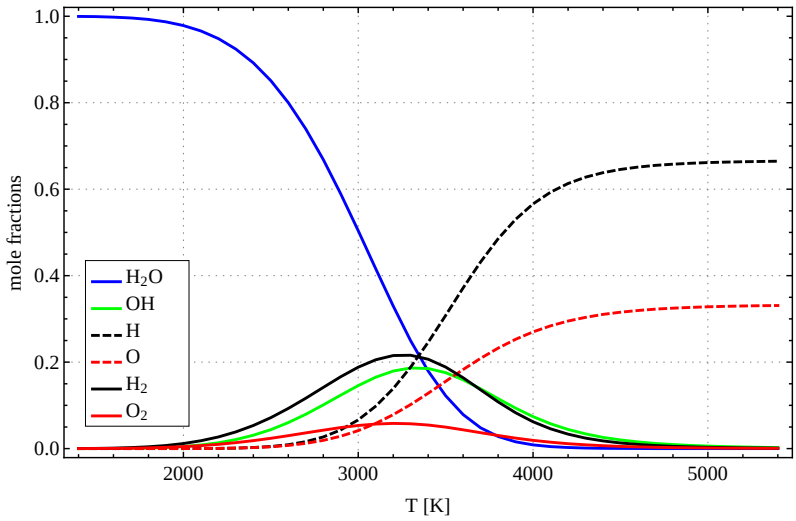

FIGURE 5.1: *Mole fractions in thermal equilibrium, when pure water is heated to a temperature T at constant pressure (see text).*

is based on work by Fussmann [private communication], extended with the set of four reactions (5.6)–(5.9) instead of one.

The enthalpy of a small mass of water m is calculated as a function of temperature, based on the dissociation model above. Again, a closed system at constant pressure is assumed. Defining the initial enthalpy (at room temperature) as zero and including heating-, vaporization- and reaction enthalpies, the total enthalpy can be written as:

$$H(T) = \begin{cases} \frac{m}{M} C_{p,\mathrm{water}}(T - 273\ [\mathrm{K}]) & \text{for } T \leq 373\ [\mathrm{K}] \\ \frac{m}{M}[C_{p,\mathrm{water}} 100\ [\mathrm{K}] + H_{\mathrm{vap}} + \sum_{i=1}^{4} \xi_{\mathrm{r}i} H_{\mathrm{r}i} \\ \quad + (\frac{f_{\mathrm{H2O}}+2}{2} n_{\mathrm{H2O}} + \frac{f_{\mathrm{OH}}+2}{2} n_{\mathrm{OH}} + \frac{f_{\mathrm{H}}+2}{2} n_{\mathrm{H}} \\ \quad + \frac{f_{\mathrm{O}}+2}{2} n_{\mathrm{O}} + \frac{f_{\mathrm{H2}}+2}{2} n_{\mathrm{H2}} + \frac{f_{\mathrm{O2}}+2}{2} n_{\mathrm{O2}}) R(T - 373\ [\mathrm{K}])] & \text{for } T > 373\ [\mathrm{K}] \end{cases} . \quad (5.15)$$

Here, $C_{p,\mathrm{water}} = 75.2\ \mathrm{Jmol^{-1}K^{-1}}$ is the heat capacity of liquid water, $H_{\mathrm{vap}} = 40.66 \cdot 10^3\ \mathrm{Jmol^{-1}}$ is the enthalpy of vaporization of water, and $M = 18\ \mathrm{gmol^{-1}}$ its molar mass. The results of the previous section enter through the reaction enthalpy term: $\sum_{i=1}^{4} \xi_{\mathrm{r}i} H_{\mathrm{r}i}$. The heat capacity of the gas phase molecules depends on the number of degrees of freedom for each of them. The following values are used:

$$\begin{array}{lcl} f_{\mathrm{H2O}} & = & 6 \\ f_{\mathrm{OH}} = f_{\mathrm{O2}} = f_{\mathrm{H2}} & = & 5 \\ f_{\mathrm{H}} = f_{\mathrm{O}} & = & 3 \end{array} . \quad (5.16)$$

It is assumed that the enthalpy $H(T)$ equals an amount of work $W(t)$ delivered to the plasmoid by the discharge. The derivative of the work function (input power) is assumed to be approximately proportional to the product of discharge current and voltage (see figure 3.7). This leads to the following approximation for $W(t)$:

$$W(t) = \begin{cases} W_0 \left(1 - e^{-\frac{2t}{\tau}}\right) & \text{for } t < t_1 \\ W_0 \left(1 - e^{-\frac{2t_1}{\tau}}\right) & \text{for } t \geq t_1 \end{cases} , \quad (5.17)$$

where W_0 is the work that would be delivered by an uninterrupted discharge, τ the characteristic time of the current and voltage decay, and t_1 the time at which the discharge is stopped.

From the ideal gas law and the molar volume of 24.7 l at 298 K, the plasma ball radius r_{ball} can be written as:

$$r_{\mathrm{ball}} = \left(\frac{3}{4\pi} \frac{T}{298.15} 24.7 \cdot 10^{-3}\ [\mathrm{m^3}] \frac{m}{M} \right)^{1/3} \quad \text{for } T > 373\ \mathrm{K}. \quad (5.18)$$

5.1.4 Results of the thermodynamical model

It is assumed that the initial water mass $m = 0.1$ g, as obtained from the precision scales measurements in section 3.3.2. Figure 5.2 (a) shows the enthalpy of this amount of partly dissociated water as a function of temperature, calculated using equation (5.15). Also in this figure is the value of the chemical energy term $\frac{m}{M}\sum_{i=1}^{4}\xi_{ri}H_{ri}$ (dashed curve), which attributes more than 50 % to the total enthalpy for $T \gtrsim 3000$ K. Part (b) of this same figure shows the discharge work function

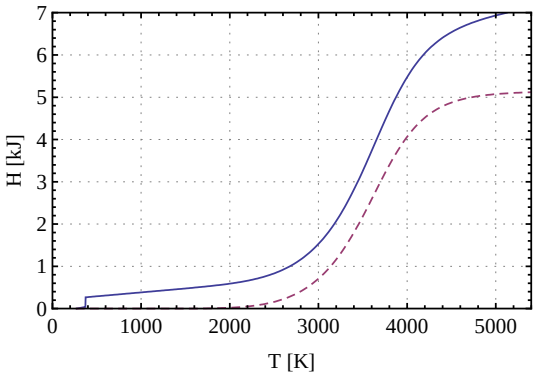

(a) Enthalpy H of 0.1 g of (partly dissociated) water as a function of temperature (solid curve) and chemical energy term (dashed curve, see text).

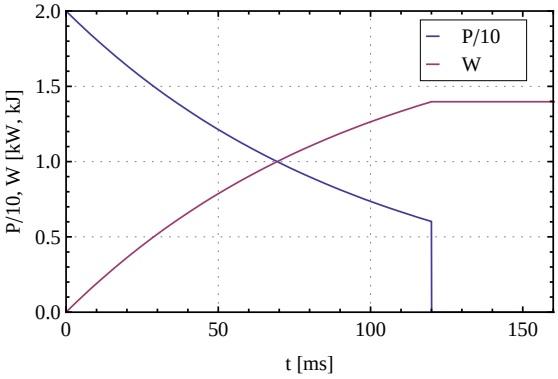

(b) Input power P and work W delivered to the plasmoid. Note that the power has been divided by 10 for clarity.

Figure 5.2: *Temperature dependent enthalpy of the dissociation-reaction mixture (a) and model input power and work.*

$W(t)$ evaluated using equation (5.17). Its derivative, the power $P(t)$, is also shown. The following parameters of the work function are used: τ=200 ms, t_1=120 ms and $W_0 = 2$ kJ. The latter value is estimated from the conclusion in section 3.3.3, that 3 kJ is available for the formation of the plasmoid. With the assumptions made here, just under half of that amount (1.4 kJ, see figure 5.2 (b)) is used to raise the enthalpy of the equilibrium mixture to its final value $H(T_{\max})$ at $t = t_1$. The difference may be explained by losses, *e.g.* by radiation.

By solving $H(T) = W(t)$ numerically, the temperature as a function of time is obtained, as shown in figure 5.3 (a). This solution for $T(t)$ is used to calculated the plasmoid radius $r_{\text{ball}}(t)$, as shown in part (b) of this figure. The mass density ρ follows from $r_{\text{ball}}(t)$ and m and is shown in figure 5.4 (a). For other parameter choices, different results may be obtained. An example is shown in figure 5.4 (b), where the maximum temperature $T_{\max} = T(t_1)$ is plotted as a function of the mass m of the system. The work function is still the same as in figure 5.2 (b).

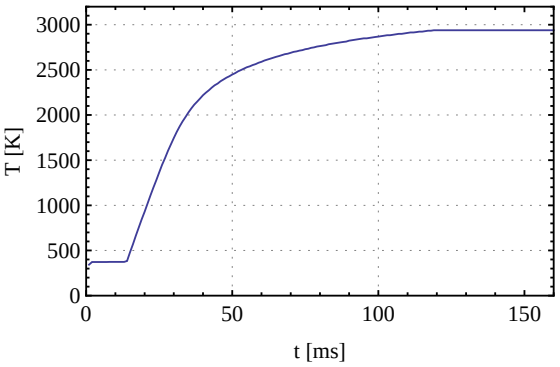

(a) Calculated temperature as a function of time. Note that in the equilibrium mixture, the temperature does not increase above the boiling point until the complete mass of water m is evaporated.

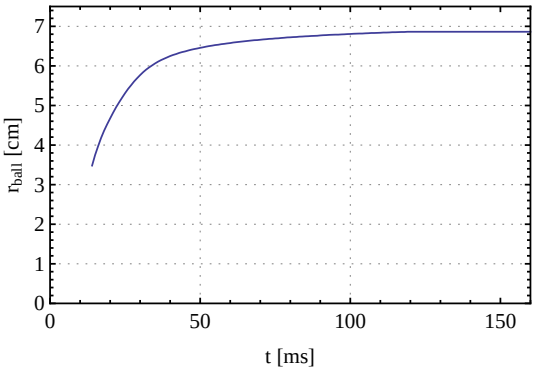

(b) Calculated plasma ball radius as a function of time. The initial part is left out as the model does not calculate the volume of the liquid water.

FIGURE 5.3: *Calculated gas temperature (a) and plasma ball radius (b) for* $m_{\text{water}} = 0.1$ *g and the work-function in figure 5.2 (b).*

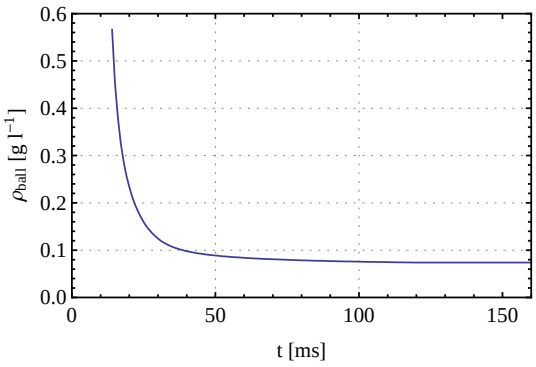

(a) Calculated mass density as a function of time.

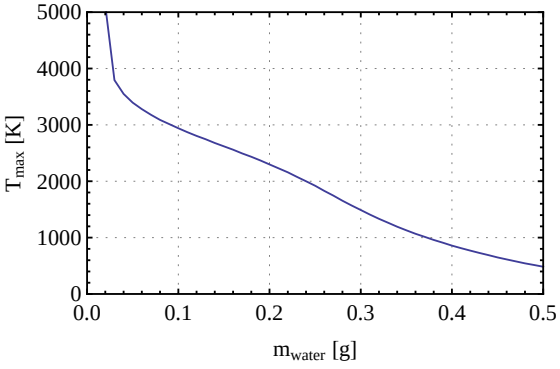

(b) Calculated maximum gas temperature as a function of the initial water mass.

FIGURE 5.4: *Calculated plasma ball mass density for* $m_{\text{water}} = 0.1$ *g (a) and the maximum gas temperature (for* $t \geq 120$ *ms) depending on the mass (b).*

5.1.5 Discussion and conclusions

Chemical equilibrium model

The thermocouple measurements had shown $T_g > 1300$ K for $t \lesssim 210$ ms and lower at later times (section 3.3.2). Van der Waals broadening of Cu I lines suggests that the gas temperature is at least $T_g \gtrsim 3000\ K$, for 20 ms $< t <$ 50 ms (section 3.4.2). Under the assumption that the plasmoid is formed from water vapor, the chemical equilibrium model predicts that this is initially dissociated to a degree $\gtrsim 50\%$ and subsequently recombines again to nearly pure water vapor for $t \gtrsim 210$ ms. Of course, this simple model relies on a number of assumptions (*e.g.* closed, uniform system in equilibrium). Important deviations can occur due to temperature gradients, diffusion, reactions with atmospheric gasses, etc.

Nevertheless, the model can explain that OH radicals are formed. The emission of OH increases in intensity up to about $t = 100$ ms and then gradually decreases again, as will be shown in the following section 5.2. With the échelle spectrometer, OH emission was measured up to about $t \approx 250$ ms. These observations fit well with the results in figure 5.1 and the mentioned gas temperatures.

As mentioned in section 2.6.1 the equilibrium equations do not give any information on the rate at which reactions take place. Assuming reaction (5.1) is induced by collision with other water molecules it can be written as:

$$H_2O(+H_2O) \rightarrow OH + H(+H_2O). \tag{5.19}$$

In [44] (page 918) the following expression is given for the rate coefficient of this reaction:

$$k\ [\mathrm{m^3 molecule^{-1} s^{-1}}] = 3 \cdot 10^{-14} \exp(-52920/T) \quad \text{for } (2000\ \mathrm{K} < T < 4000\ \mathrm{K}), \tag{5.20}$$

with $[H_2O]$ the concentration of water in m^{-3}. The characteristic time for the reaction is given by:

$$\tau = [H_2O] \left(\frac{\mathrm{d}[H_2O]}{\mathrm{d}t} \right)^{-1} = k[H_2O]. \tag{5.21}$$

When assuming $[H_2O]$ equals the ideal gas density, τ equals 3 s, 60 ms and 10 μs at $T = 2000$ K, 3000 K and 4000 K respectively. Thus, gas temperatures roughly above 3000 K are required for this reaction to reach near-equilibrium concentrations during the lifetime of the plasmoid. The rate coefficients for the decomposition of H_2, the reverse reaction of (5.3) can also be found in [44] and is comparable or higher than that of reaction (5.1) for 2000 K $< T <$ 4000 K.

Thermodynamics

The thermodynamical calculations demonstrate that the chemical equilibrium model can be integrated with calorimetry results in a way that is consistent with observations and measurements. Most importantly, it is shown that gas temperatures in the range of 2000 K to 4000 K can indeed be expected from the known amount of evaporated water and the available energy. Also, the calculated plasmoid radii agree well with measurement results in figure 3.7. It should be noted that the temperature and radius in the initial phase of the discharge are expected to deviate from the model, as the evaporation is not an equilibrium process (*i.e.* the temperature in the vapor phase is expected to rise above 373 K, also before the complete mass m is evaporated).

It is shown in figure 5.2 (a) that for gas temperatures above 3000 K the chemical energy term $\frac{m}{M} \sum_{i=1}^{4} \xi_{ri} H_{ri}$ is the largest contribution to the plasmoids enthalpy. One could call this a form of chemical "energy storage". The buildup of chemical energy reduces further temperature increase and thus heat losses, *e.g.* due to radiation.

An apparent inconsistency is provided by the mass density in figure 5.4. The final value $\rho = 0.1$ g/l can be used in combination with the density of air at room temperature $\rho_{air} \approx 1.2$ g/l to estimate the (constant) velocity of the rising plasma ball. Assuming the friction force is given

by the drag equation $F_\mathrm{f} = -\frac{1}{2} c_\mathrm{w} \pi r_\mathrm{ball}^2 \rho_\mathrm{air} v^2$, this leads to:

$$v = \left[\frac{8 r_\mathrm{ball} g}{3 c_\mathrm{w}} \left(1 - \frac{\rho}{\rho_\mathrm{air}} \right) \right]^{1/2}, \tag{5.22}$$

with g the gravitational acceleration and c_w the drag coefficient. Using $c_\mathrm{w} = 0.45$ (typical value for a closed sphere moving in air) this evaluates to $v \approx 2$ ms^{-1} at $\rho = 0.1$ g/l. The observed velocity of the ball's upper boundary is only 0.8 ms^{-1} (figure 3.7). Mixing with cooler air on the outside of the plasmoid may explain the observed boundary velocity being lower than that of the (invisible) inner material.

5.2 Molecular emission and chemical reactions

Besides atomic lines, molecular bands of OH and CaOH have been identified in the spectra of the plasmoids (see figure 3.10). This section describes this molecular emission in more detail. By comparing with literature spectra and simulation of the OH vibrational bands, the emission is connected to chemiluminescence reactions. The well known emission band of the OH radical at 306 nm is studied in more detail in the next section 5.3. As this section is more descriptive than most of this report, the structure is chosen somewhat differently. First the most important observations are given, accompanied by comparisons with spectra from literature and simulation. The conclusions and remaining topics of discussion follow after this.

5.2.1 Observations and comparisons

The UV bands between about 300 nm and 330 nm are long known to belong to the ($A^2\Sigma^+ \rightarrow X^2\Pi$) transition of the OH radical (see [62]). The green and orange/red molecular bands at 544–567 nm and 586–651 nm have been assigned by several authors to CaOH (calcium hydroxide) emission from the $B^2\Sigma^+$ and $A\Pi^+$ states respectively (see [63, 64, 65] and the references therein). The left part of figure 5.5 shows the OH band recorded at several times, using the échelle spectrometer. The intensity of the OH band shows a different evolution than that of most spectral lines. During

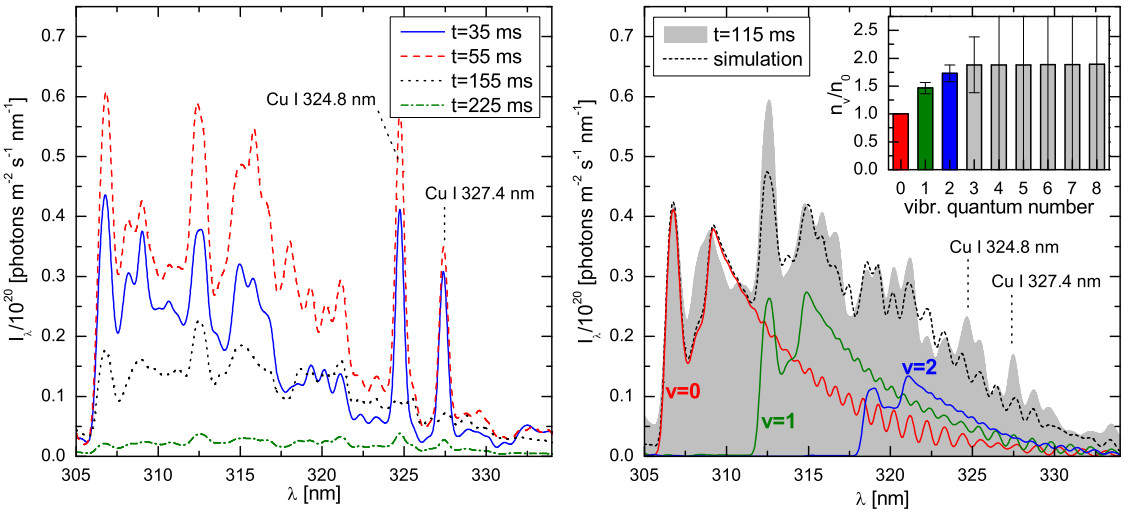

Figure 5.5: *Left: OH emission spectrum measured at different times. Maximum intensity is reached approximately at current zero. Right: comparison of measured and simulated spectrum. The contribution of the individual bands with vibrational quantum numbers $v = 0$, 1 and 2 are indicated by the solid (colored) lines. The inset shows the occupation of the vibrational levels relative to $v = 0$ in the simulation.*

the first 50 ms the intensity rises. Then, between 50 ms and 120 ms the intensity of the band remains at approximately the same level. After that (and after the discharge current reaches zero), the intensity decreases again, but it decays slower than that of the atomic lines. The evolution of the CaOH bands is very similar to this behavior.

OH vibrational populations

OH radicals may be formed from the (endothermal) decomposition reaction of water during the discharge, induced electrically (electrolysis) and/or by thermal dissociation, as shown in the previous section 5.1. The right part of figure 5.5 shows a comparison with a simulated OH emission

spectrum, produced using the LIFbase simulation program [51]. The program contains a database of energy levels and vibrationally and rotationally resolved Einstein coefficients for spontaneous emission, obtained as described in [66]. The state populations (thermal or non-thermal) form the input of the program. The intensity of a particular transition is then calculated according to equation (2.128). Predissociation and quenching are included in the model by means of a quantum yield like in equation (2.127). The (state dependent) predissociation rates are included in the program. The quenching rate was estimated assuming H_2O perturbers at 2000 K and atmospheric pressure and a rate coefficient of $5 \cdot 10^{-16}$ m^3s^{-1} from [67] for all levels. This gives $K^{quench} = 5 \cdot 10^{-16}$ $m^3s^{-1} \cdot 3.6 \cdot 10^{24}$ $m^3 = 1.8 \cdot 10^9$ s^{-1}.

The intensity of the vibrational band heads was matched with that of a measurement at $t = 115$ ms. A rotational temperature of 15,000 K was assumed for all vibrational bands (see next section). The simulation indicates a non-thermal vibrational population distribution. The higher vibrational levels are overpopulated, likely because they are fed by chemical reactions. It is noted that it is important to include the quenching rate in the simulation. When neglecting collisional quenching, the measured vibrational bands can not be reproduced at realistic population distributions.

CaOH emission

The evolution of intensity of the CaOH molecular bands at 544–567 nm and 586–651 nm is similar to that of the OH bands: an initial increase throughout the period of the current flow, followed by a relatively slow decay. Therefore it is likely that CaOH is formed in the vapor phase following the discharge triggering. Calcium is available in tap water in considerable quantities (in the order of 20 mg/l). The CaOH emission persisted using various salt additives and also at a reduced calcium concentration achieved by de-ionizing. This suggests that the species reacting with Ca (or Ca^+) to form CaOH is available in relatively large amounts, independent of the precise composition of the solution.

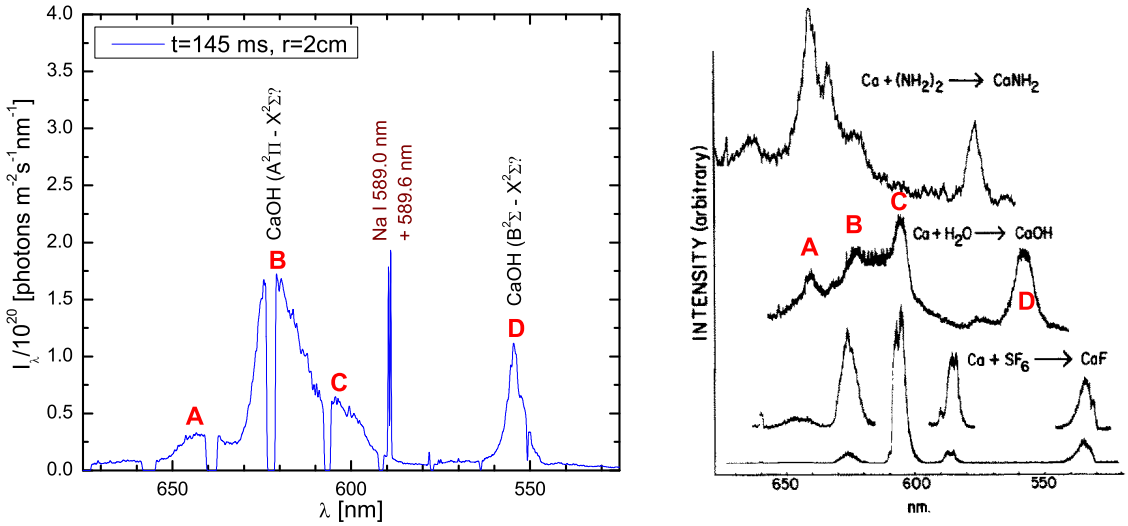

FIGURE 5.6: *Molecular band spectra recorded with the échelle spectrometer from above at t =145 ms and r =2 cm (left) (convoluted with 10 pixel wide Gaussian to reduce noise) and figure showing chemiluminescence spectra of various reactions involving calcium, copied from literature [64]. The measured spectrum shows CaOH peaks at the same position (but different relative intensity) as those of the reaction: $Ca + H_2O \rightarrow CaOH + H$. The literature spectrum was not corrected for the apparatus profile. Corresponding peaks are indicated with red capital letters.*

CaOH emission occurs in chemiluminescence reactions, for instance in flames [63]. A reaction of calcium and water forming excited calcium hydroxide is possible, but the reaction cross section

is relatively small. The right part of figure 5.6 shows spectra from literature [64] recorded in a low pressure (1-3 Torr) calcium–water vapor mixture at a gas temperature of 500–700 K. The chemiluminescence was described as weak by the authors. For comparison, a spectrum recorded from the atmospheric plasmoid in the same wavelength range is shown on the left. The peak locations are the same, confirming the CaOH assignment, but the relative intensities are quite different. It should be noted though that no correction for the apparatus response was applied to the literature spectrum.

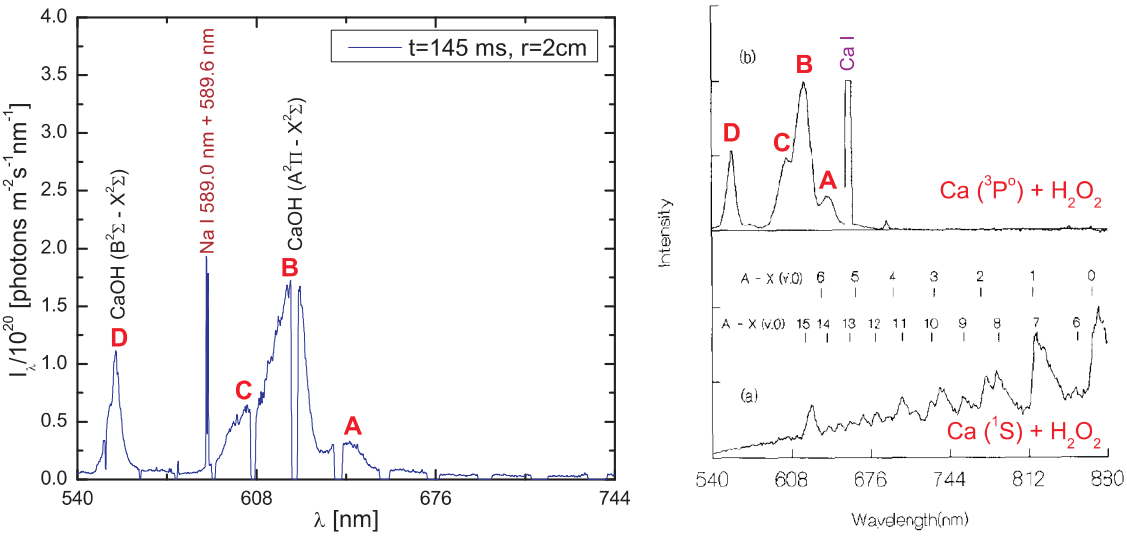

Figure 5.7: *Same plasmoid spectrum as in figure 5.6, now compared with another set of chemiluminescence spectra copied from literature [65]. The measured spectra is practically identical to that of the of CaOH produced in the reaction of $^3P^o$ Ca with H_2O_2 (top right). The bottom right spectrum is that of CaO produced in the reaction of ^1S Ca with H_2O_2. These spectra are all corrected for apparatus response.*

Another possible source of electronically excited CaOH is a chemiluminescence reaction with H_2O_2. This reaction was studied by Oberlander *et al.* [65] in a calcium-vapor mixture at temperature of 800–900 K and pressure of 0.4 ± 0.05 Torr. It is reported that the chemiluminescence reaction of calcium with H_2O_2 is much more efficient than that with water [65]: the signal in a vapor consisting of a mixture of 70% by weight H_2O_2 and 30% H_2O is more than two orders of magnitude stronger than that using pure water vapor. Also, these authors were able to distinguish between reactions with ground state (^{1}S) calcium atoms and those in the excited metastable (^{3}P^o) state, leading to different reaction products: ^{1}S produces mainly CaO (not detected here) whereas ^{3}P^o results only in CaOH chemiluminescence. An overview of these reactions with experimentally derived cross section is given in table 5.1.

Table 5.1: *Chemiluminescence reactions of calcium and hydrogen peroxide with experimentally derived cross section. The estimated uncertainties in the cross sections are ±20%. Source: [65]*

Index	Reaction	σ_{reaction} [Å^2]	λ range [nm]
(a)	$Ca(^3P^o)+H_2O_2 \rightarrow CaOH(A^2\Pi)+OH$	6.5	586–651
(b)	$Ca(^3P^o)+H_2O_2 \rightarrow CaOH(B^2\Sigma)+OH$	1.3	544–567
(c)	$Ca(^1S)+H_2O_2 \rightarrow CaO(A^1\Sigma, A'^1\Pi)+H_2O$	1.6	551–883
(d)	$Ca(^1S)+H_2O_2 \rightarrow CaOH(A^2\Pi)+OH$	0.03	616–633

A comparison of the literature spectra for the reactions in this table with those of the plasmoid

is shown in figure 5.7. There is a nearly perfect match in both peak positions and relative intensities with the Ca ($^3P^o$) + H_2O_2 chemiluminescence spectrum, whereas CaO appears to be absent.

Based on this agreement of the emission spectra, the experimental reaction cross sections in table 5.1 and the abundance of OH radicals and excited (metastable) calcium atoms in the plasmoid (see chapter 4 for the latter), reactions (a) and (b) in this table are proposed as a source of CaOH emission. A possible source of H_2O_2 is the combination reaction of two OH radicals:

$$\mathrm{OH{+}OH(+M)} \rightarrow \mathrm{H_2O_2(+M)}. \tag{5.23}$$

An alternative scenario is the direct combination reaction of OH and Ca:

$$\mathrm{Ca{+}OH(+M)} \rightarrow \mathrm{CaOH(A^2\Pi \text{ or } B^2\Sigma^+)(+M)}, \tag{5.24}$$

for which no reference data was found. For this reaction, the chemical potential of the reactants in their ground state exceeds that of the products by an amount slightly greater than that for for reactions (a) and (b) in table 5.1 [65], so that ground state calcium atoms will probably react as well.

The combination reactions (5.24) and (5.23) are most effective at low temperatures ($\lesssim 10^3$ K), *e.g.* on the outside of the plasma ball and may cause the yellowish-green boundary layer (see *e.g.* figure 3.3; the orange/red band is suppressed by the response of the human-eye).

5.2.2 Discussion and conclusions

Both the vibrational population of OH and the observed CaOH spectra indicate that chemical processes are the likely cause of the molecular band emission – and thus of the bright appearance and observed long lifetime of the plasmoids (see figures 3.10 and 3.11). As the mole fractions of calcium or other elements dissolved in the water are small (*e.g.* of the order of 10^{-4} or less), it is unlikely that these elements play a role in transferring energy to the autonomous phase. Rather, the chemical energy of the plasmoid is stored in the dissociation products of water. However, as the OH emission is mostly in the UV, the chemiluminescence reactions involving calcium may be crucial to transfer part of this chemical energy to the visible wavelength range.

Chemiluminescence reactions analogue to those in table 5.1 can also occur between other group 2 metals, such as Sr and Ba, and H_2O_2, as well as with other oxygen containing molecules such as *t*-BuOOH (=$(CH_3)_3COOH$), HNO_3 and NO_2 [50].

5.3 OH rotational temperature

5.3.1 Introduction

The UV bands of OH have been studied quite extensively in the past [52, 68, 69, 70, 71, 72]. The bands in the 280–355 nm range belong to the same electronic transition: $A^2\Sigma \rightarrow X^2\Pi$. The band with its head at 306.4 nm ($v' = 0 \rightarrow v'' = 0$) is frequently used for temperature measurements in hot gases or plasmas containing oxygen and hydrogen, under the assumption that the rotational temperature is equal to the gas temperature (see section 2.6.2).

Therefore, an attempt is made to measure the rotational temperature of the atmospheric plasmoids from the OH emission spectrum. For this, the approach sketched in section 2.6.2 is used to simulate the emission spectrum. The wavelengths λ_{qp}, upper level energies E_q and reference intensities I_{qp}^{ref} at $T_{\mathrm{ref}} = 3000$ K, for 113 lines between 306.2 nm and 310 nm, are obtained from Dieke and Crosswhite [70]. The intensity $I_\lambda(T_{\mathrm{rot}})$ is then calculated using equations (2.132)–(2.134), assuming $Q(T_{\mathrm{ref}})/Q(T_{\mathrm{rot}}) \approx 1$. Line broadening ($P(\lambda)$) is assumed to be due to the apparatus profile of the échelle spectrometer, which is approximated by a pseudo-Voigt profile with w_{V}=16 pm and $w_{\mathrm{G}} = 4w_{\mathrm{L}}$.

5.3.2 Results

Figure 5.8 shows the calculated emission spectra at rotational temperatures of 2000 K, 4000 K, 6000 K and 8000 K. The intensities of the highest peak (at 308.9 nm) was kept fixed, so that the relative differences are clear. These spectra agree well with simulated and measured spectra found in literature [51, 52, 72].

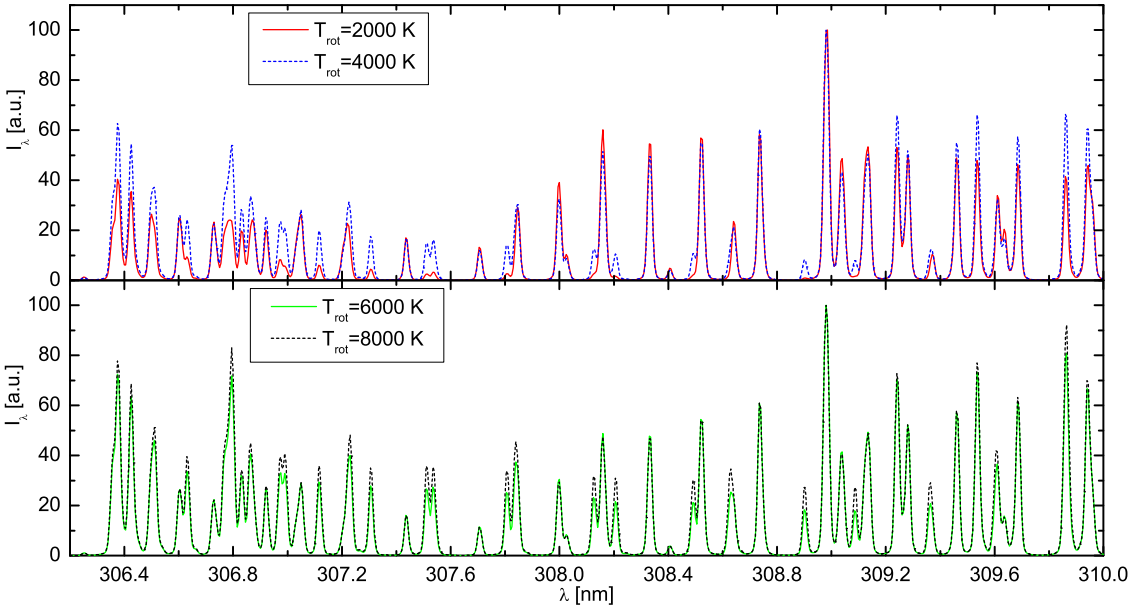

Figure 5.8: *Simulated OH spectrum in the range of 306 nm to 310 nm for various rotational temperatures. The spectra are scaled to match the intensity of the highest peak at 308.9 nm. The simulated apparatus profile is a Voigt distribution with w_{V}=16 pm and $w_{\mathrm{G}} = 4w_{\mathrm{L}}$, an approximation of the échelle spectrometer apparatus profile.*

The simulated spectra were compared to measured spectra of the atmospheric plasmoid, for shots using tap water with 0.2 g/l HCl. The measured data is recorded using the échelle spectrometer (top view), at a radial position $r = 2$ cm, to avoid light from the electrode region and

reduce the effect of possible vertical temperature gradients (which are expected to be greater at the center). These comparisons are shown for $t = 55$ ms and $t = 145$ ms in figure 5.9. The upper part of this figure (a) shows the measurement at $t = 55$ ms and simulated spectra at two temperatures: $T_{\rm rot} = 2000$ K, the estimated gas temperature (from thermocouples) and $T_{\rm rot} = 9000$ K, which shows the best overall agreement between measurement and simulation. At $t = 145$ ms the situation is similar, as shown in part (b).

It is clear that for none of the temperatures, the simulated spectra agree completely with the measured ones. To find the reason for this, the emission from the R_2-branch was investigated in more detail. The indicator near the upper axis in figure 5.9 (a) and (b) assigns the upper level rotational quantum numbers N' of the peaks belonging to this band (peak locations from [70]). The simulation at $T_{\rm rot} = 2000$ K was scaled to match the peak height for the peak with $N' = 4$, as indicated by the arrow. This gives reasonable agreement in relative intensity for the peaks at $N' = 3$ and $N' = 7$, that can also be resolved. On the other hand, the simulations at higher $T_{\rm rot}$ give the correct relative intensities at $N' = 13$ and higher. To confirm this, a Boltzmann plot was made. (For information about the Boltzmann plot-method to determine the rotational temperature, see *e.g.* [70, 71]). This Boltzmann plot is shown in figure 5.10 for $t = 55$ ms. Measurements at different radial positions were used to determine if temperature gradients could explain the deviations from the simulations.

It follows from equations (2.131) and (2.129) that for thermal rotational population distribution, the plotted points in figure 5.10 should all lie on a single line, the slope of which equals -1/($T_{\rm rot}$ [eV]). However, it is clear from this figure that this is not the case. As is shown in this figure the higher rotational quantum numbers $N' \geq 8$ can be fitted well with a line corresponding to a rotational temperature $T_{\rm rot,1}$ in the order of 10^4 K. For $3 \leq N' \leq 7$ on the other hand, $T_{\rm rot,2} = O(10^3$ K) is obtained. The results of the fits at various radial positions are shown in 5.10.

5.3.3 Discussion and conclusions

An investigation of the rotational population distribution of the R_2-branch of the $(v', v) = (0, 0)$ band between 306 and 310 nm shows that the excited state rotational distribution is non-thermal, like the vibrational distribution. A high rotational temperature $T^{0,0}_{\rm rot} = O(10^4$ K) describes the higher rotational levels ($N' > 7$) best, whereas $T^{0,0}_{\rm rot} = O(10^3$ K) is more appropriate for $3 \leq N' \leq 7$.

The Boltzmann plots obtained agree well with those of OH($\rm A^2\Sigma^+, v' = 0$) produced by dissociative excitation of water vapor in literature. In [69] a rotational temperature of about 800 K is reported for the low rotational quantum numbers and 15,000 K for the higher ones. An electrodeless high-frequency discharge in water vapor is used in the experiments described in this article. The authors report that the lower temperature is in the order of the gas temperature in their experiment.

Similar results, but at higher rotational temperatures of about 3400 K and 30,000 K, can be found in [71] for water vapor exposed to an electron beam (1–1000 eV). In [71] strong bending vibrations in excited state H_2O molecules are mentioned as a possible cause of this 'abnormal' rotational energy in OH($A^2\Sigma^+$). The reader is referred to this text and the references therein for a further discussion of this topic.

The effect of absorption, *i.e.* optical thickness, has been neglected in the above results. In [70] it is reported that for the case of an oxy-acetylene flame, self absorption plays a role for the strongest lines. Indications that this is the also case for the spectra recorded here may indeed be seen in figure 5.9, where the simulated intensity of the strongest lines (*e.g.* at 308.9 nm) lies above that in the measurements. This is not further investigated.

It is concluded that the higher rotational temperatures are a consequence of the dissociation process of water and that the lower temperature in the order of 1000 K is expected to be closest to the gas temperature.

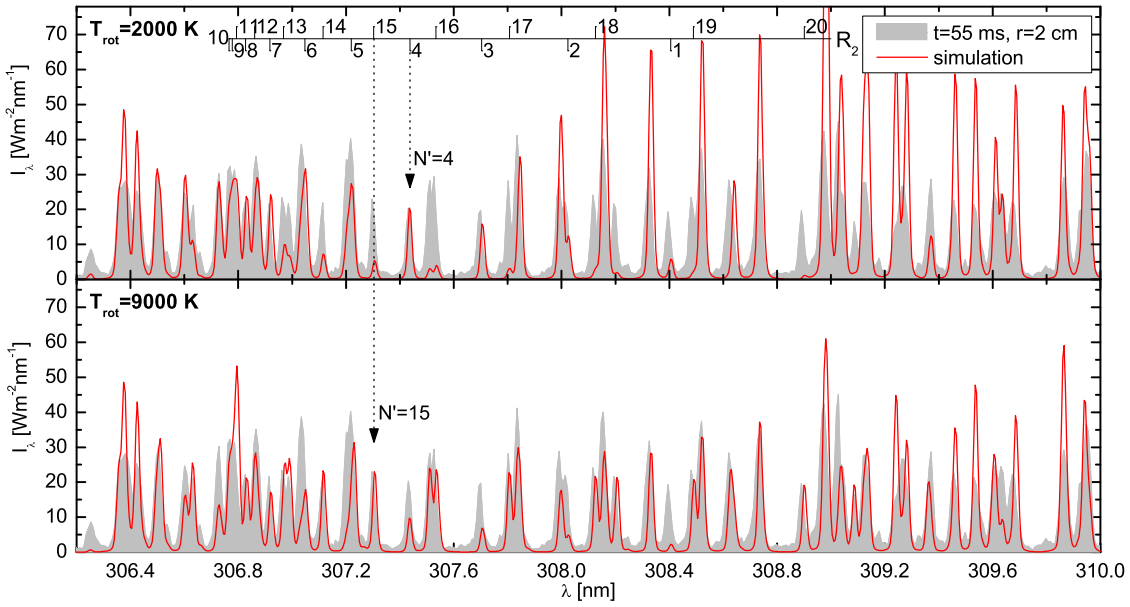

(a) $t = 55$ ms

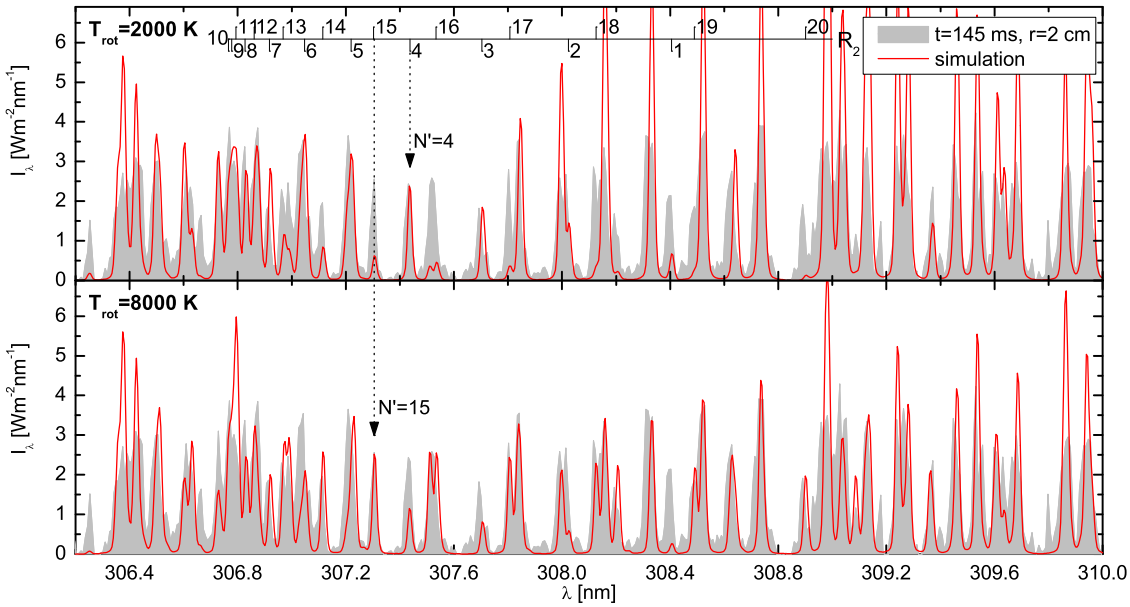

(b) $t = 145$ ms

FIGURE 5.9: *Comparison between measured OH spectra between 306.2 nm and 310.0 nm at t=55 ms (a) and t=145 ms (b) and simulations. Measurements were done using the échelle spectrometer at a radial position r = 2 cm (top-view). The simulations use rotational temperatures of* $T_{\mathrm{rot}} = 2000$ *K (upper parts) and* $T_{\mathrm{rot}} = 11500$ *K. The simulated spectra were scaled to match the peaks at 307.437 nm and 307.303 nm respectively. These peaks correspond to transitions in the* R_2*-branch of the* $A^2\Sigma^+, v' = 0 \rightarrow X^2\Pi, v'' = 0$ *electronic transition, with upper-level rotational quantum numbers* $N' = 4$ *and* $N' = 15$ *respectively. The upper-level rotational quantum numbers of the first 20 peaks in the* R_2*-branch are shown by the indicators in the upper part of each graph. Note that there are many peaks belonging to other branches in the spectra as well.*

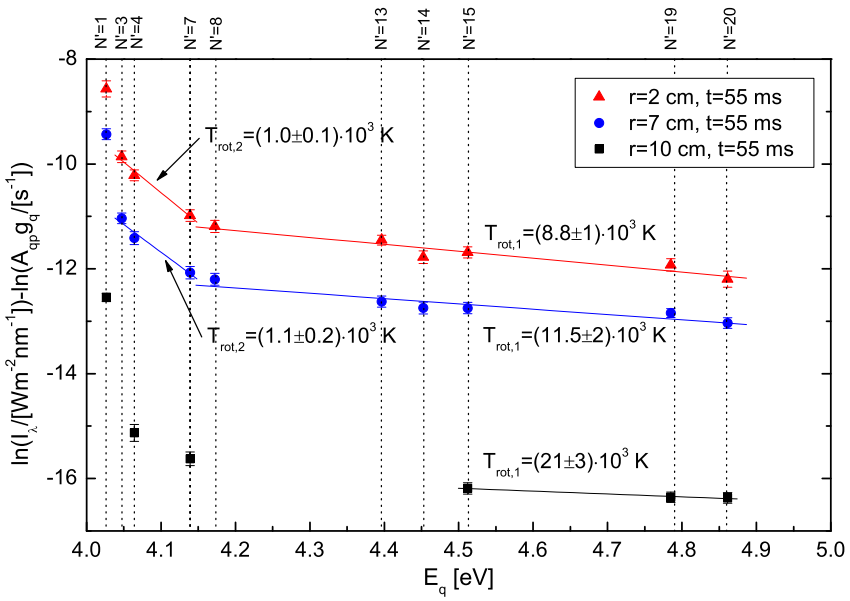

FIGURE 5.10: *Boltzmann plot of the R_2-branch of the $A^2\Sigma^+, v' = 0 \rightarrow X^2\Pi, v'' = 0$ vibrational band in the spectrum of OH. The degeneracy of the upper level equals $g_q = 2J' + 1$, with $J' = N' - 1/2$, where N' is the upper level rotational quantum number (without spin) as indicated along the upper axis. Emission coefficients A_{qp} are taken from [66]. Shown are three measurements at t=55 ms, at different radial positions. The data has been fitted with two linear functions, giving two rotational temperatures: $T_{\mathrm{rot},1}$ for the rotational quantum numbers $N' \geq 8$, and $T_{\mathrm{rot},2}$ for $3 \leq N' \leq 7$.*

Chapter 6

Conclusions

In this report, ball-like plasmoids generated from a capacitor discharge in a water vessel were studied using a variety of diagnostic techniques. Various models were presented that provide insight in different aspects of the complex phenomenon. Below, the main conclusions concerning the plasma parameters, energy storage, and appearance and other properties are summarized and the methods used to arrive at these conclusions are mentioned.

Plasma parameters

Most investigations have focussed on finding the time-dependent plasma parameters of the plasmoids, mainly via spectroscopic methods.

Two spectroscopic techniques have been applied to measure the electron density. Stark broadenings measurements on spectral lines of different elements were conducted, providing information on n_e in the first 75 ms of the plasmoid's lifetime. Spectroscopic electron density measurements at later times provided the biggest challenge, and were obtained from the relative and absolute intensities in the spectrum of atomic calcium, by comparing with simulations using a collisional radiative model (CRM). The results of both methods are consistent with an exponentially decreasing electron density from 10^{22} m^{-3} and higher in the first 10 ms to about 10^{20} m^{-3} at $t = 150$ ms.

Also decreasing electron temperatures were measured spectroscopically from intensity ratios of atomic copper lines, under assumption of local thermodynamic equilibrium, and from calcium lines using the CRM. In both cases, the effect of optical thickness was considered and proved to play an important role, also for transitions between excited states. The electron temperature development is summarized as follows: in the center of the plasmoids T_e decreases from about 5500 K initially to 2900 K at, $t = 120$ ms, when the current is quenched. Comparison of measured spectra with simulations using the CRM indicate that in the autonomous phase, the temperature decreases further, as expected, to about 2500 K at $t = 150$ ms. Away from the center, the electron temperature is lower: measurements indicate that a hot core about half the diameter of the plasmoid is surrounded by cooler plasma.

It is shown that calcium, present in tap water or in the form of salt, reaches considerable ionization degrees: $n_{\mathrm{CaII}}/(n_{\mathrm{CaI}} + n_{\mathrm{CaI}}) \approx 0.7$ at $t = 55$ ms is obtained from comparing opacity broadening in the atomic and ionic resonance lines. This is consistent with a Saha-ionization equilibrium at the measured electron temperatures and estimated (total) calcium density. For other elements with low ionization energies, such as K, Na, Sr and Al, comparable ionization degrees are expected. These elements are expected to provide the bulk of the free electrons causing atomic line radiation in the autonomous phase.

Energy storage and chemical processes

From calorimetric measurements, an estimate of the energy available for the plasmoid formation (about 3 kJ) was obtained. A total emitted radiation energy of 700 J was measured using a

pyroelectric sensor. These and other measurements, *e.g.* of water evaporation, using precision scales, were combined in a simple model, that calculates the enthalpy, temperature and other thermodynamic properties of the plasmoid under the assumption of chemical equilibrium in a closed system. The model shows that gas temperatures in the range of 2000 K to 4000 K can be expected, consistent with thermocouples that indicate $T_g > 1200$ K at later times. The calculated plasma ball radii are in agreement with observations. The same model predicts the chemical composition of the plasmoid, which is assumed to arise from the dissociation of water, driven by the capacitor discharge.

The theoretical prediction that water is dissociated during formation of the plasmoid, is supported by measurements of the vibrational and rotational distributions in the molecular spectrum of the OH radical. Both are shown to be non-thermal and the rotational distribution of the OH band with its head at 306.4 nm fits well to that found in various literature sources, in which it is attributed to the dissociation of water.

The thermodynamic calculations also show that at the expected (central) gas temperature of 3000 K or more, after the capacitor discharge, at least half of the plasmoids total enthalpy consists of chemical energy of the various dissociation products of water. This can be called a form of chemical energy storage.

Appearance and other properties

The largest part of the visible radiation power was found to be emitted by molecular bands of CaOH and OH, causing the bright appearance of the plasmoids. The characteristic colors of the boundary layer can be explained by chemiluminescence reactions that are most effective at the lower gas temperature on the outside of the plasmoid and produce electronically excited CaOH that emits in the green and orange/red wavelength range. Vortices were observed that likely attribute to the characteristic stable spherical shape of the plasmoids. Using small double probes it was measured that the plasmoids boundary layer consists of an electric double layer, with nett negative charge on the outside.

Acknowledgements

Firstly, I would like to express my gratitude Prof. Dr. Gerd Fussmann and Prof. Dr. Burkhard Jüttner for starting this unique research project, for their enthusiasm about the subject and for supporting me on countless occasions with their great experience and knowledge in the field of plasma physics and beyond.

Prof. Dr. Gerrit Kroesen is thanked for enabling me to embark on this project in the first place, for his excellent support and for visiting me here in Berlin more than once.

I am also grateful to Prof. Dr. Kurt Behringer for being continuously interested in the project, for his many helpful comments and suggestions and for providing the atomic data from the ADAS system. Dr. Ursel Fantz is thanked for providing, installing, and calibrating the échelle spectrometer, and for even bringing it from Garching bei München to Berlin. Without this, most of the results could not have been obtained.

Dipl. Phys. Ole Waldmann and Dipl. Phys. Tilmann Lunt provided much help with their many corrections and comments to the manuscripts of this report and the submitted paper, and by the fruitful discussions I had with them on so many occasions.

Dr. Joost van der Mullen is thanked for his advice concerning the collisional radiative model and for interrupting his holidays to visit me at the institute here in Berlin.

I am grateful to the complete staff and students of the Arbeitsgruppe Plasmaphysik for their countless helpful comments and suggestions, for their technical support and mostly for making me feel welcome.

Personally, I am in great depth to my girlfriend Maike and my parents for supporting me in many different ways during this project and the writing of this report.

References

[1] A. G. Shabanov, Krivshich, B. Yu. Sokolovsky, and O. M. Zherebtsov. *Proc. 9th Int. Symp. on Ball Lightning, Eindhoven*, 2006.

[2] A. A. Egorov, S. I. Stephanov, and G. D. Shabanov. *Physics-Uspekhi*, 47:99–101, 2004.

[3] Y. Sakawa, K. Sugiyama, T. Tanabe, and R. More. *Plasma and Fusion Research: Rapid Communications 1*, 1(39):1–2, 2006.

[4] A. G. Shabanov, Krivshich, B. Yu. Sokolovsky, and O. M. Zherebtsov. *Proceedings of 3rd International Conference on Natural and Antropogenetic Aerosols, St. Petersburg*, page 368, 2001.

[5] B. M. Smirnov. The physics of ball lightning. *Physics Reports*, 224(4):151–236, 1993.

[6] J. Abrahamson, A. V. Bychkov, and V. L. Bychkov. Recently reported sightings of ball lightning: observations collected by correspondence and russian and ukrainian sightings. *Phil. Trans. R. Soc. Lond. A*, 360:11–35, 2002.

[7] J. Abrahamson and J. Dinniss. Ball lightning caused by oxidation of nanoparticle networks from normal lightning strikes on soil. *Nature*, 403(519–521), 2000.

[8] G. S. Paiva, A. C. Pavao, E. A. de Vasconcelos, Jr. O. Mendes, and Jr. E. F. da Silva. Production of Ball-Lightning-Like Luminous Balls by Electrical Discharges in Silicon. *Phys. Rev. Lett.*, 98(4):048501–1–4, 2007.

[9] H. R. Griem. *Principles of Plasma Spectroscopy*. Cambridge University Press, 1997.

[10] I.H. Hutchinson. *The principles of plasma diagnostics*. Cambridge University Press, 1987.

[11] U. Fantz. Basics of plasma spectroscopy. *Plasma Sources Sci. Technol. (2006)*, 15:S137S147, 2006.

[12] A. Versteegh, K. Behringer, U. Fantz, G. Fussmann, B. Juettner, and S. Noack. Long-living plasmoids from an atmospheric water discharge. Submitted to Plasma Sources, Sci. and Technol., 2007.

[13] G. Fussmann. Einführung in die Plasmaphysik. Vorlesung an der Humboldt Universität zu Berlin.

[14] L. Vriens and A. H. M. Smeets. Cross-section and rate formulas for electron-impact ionizatoin, excitation, deexcitation and total depopulation of excited atoms. *Physical Review A*, 22(3):940–951, January 1980.

[15] Yu. Ralchenko, F.-C. Jou, D.E. Kelleher, A.E. Kramida, A. Musgrove, J. Reader, W.L. Wiese, and K. Olsen. NIST Atomic Spectra Database (version 3.1.1). available: `http://physics.nist.gov/asd3`. 2007.

[16] J.A.M. van der Mullen. Excitation equilibria in plasmas; a classification. *Physics Reports*, 191(2,3):109–220, 1990.

[17] A. N. Cox, editor. *Allen's Astrophysical Quantities*. Springer, New York, 4th edition, 1999.

[18] W. Lotz. An empirical formula for the electron-impact ionization cross-section. *Zeitschrift für Physik*, 206(2), 1967.

[19] M. J. Seaton. Radiative recombination of hydrogenic ions. *Monthly Notices of the Royal Astronomical Society*, 119:81–89, 1959.

[20] Y. Hahn and MCLaughlin D. J. Scaling behavior of radiative recombination cross-sections and rate-coefficients. *Physical Review A*, 43(3):1313–1323, 1991.

[21] A. L. Irwin. Polynomial partition function approximations of 344 atomic and molecular species. *The Astrophysical Journal, Supplement Series*, 45:621–633, 1981.

[22] B. Makin. Variational theory of three-body electron-ion recombination rates. *Phys. Rev. Let.*, 11(6):281–283, 1963.

[23] Y. Hahn. Electronion recombination processesan overview. *Rep. Prog. Phys. 60*, 60:691–759, 1997.

[24] K. Behringer. Escape factors for line emission and population calculations. IPP report IPP 10/11, Max-Planck-Institut für Plasmaphysik, April 1998.

[25] F. E. Irons. The escape factor in plasma spectroscopy i - the escape factor defined and evaluated. *J. Quant. Spec. Rad. Trans.*, 22(1), 1979.

[26] I. I. Sobel'Man, L. A. Vainshtein, and E. A. Yukov. *Excitation of Atoms and Broadening of Spectral Lines*. Springer, 1995.

[27] H. R. Griem. *Plasma Spectroscopy*. McGraw-Hill, New York, 1964.

[28] N. Konjević. Plasma broadening and shifting of non-hydrogenic spectral lines: Present status and applications. *Physics Reports*, 316:339–401, 1999.

[29] C. W. Allen. *Astrophysical Quantities*. Athlone Press, New York, 3rd edition, 1973.

[30] H. R. Griem. Strak broadening of isolated spectral lines from heavy elements in a plasma. *Phys. Rev.*, 128(2):515–523, 1962.

[31] H. R. Griem. *Spectral Line Broadening by Plasmas*. London: Academic Press, 1974.

[32] M. A. Gigososy and V. Cardenosoz. New plasma diagnosis tables of hydrogen Stark broadening including ion dynamics. *J. Phys. B: At. Mol. Opt. Phys.*, 29:47954838, 1996.

[33] C. Stehlé and R. Hutcheon. Extensive tabulations of stark broadened hydrogen line profiles. *Astron. Astrophys. Suppl. Ser.*, 140:93–97, 1999.

[34] C. R. Vidal, J. Cooper, and E. W. Smith. Hydrogen stark-broadening tables. *Astrophys. J.*, 25(214):37–136, 1973.

[35] M. S. Dimitrijević, S. Sahal-Bréchot, and V. Bommier. *Astron. Astrophys. Suppl. Series*, 89:581, 1991.

[36] N. Konjević and Roberts. A critical review of the stark widths and shifts from non-hydrogenic atoms. *J. Phys. Chem. Ref. Data*, 5(2):209–257, 1976.

[37] N. Konjević and W. L. Wiese. *J. Phys. Chem. Ref. Data*, 19(6):1307–1385, 1990.

[38] N. Konjević, A. Lesage, J. R. Fuhr, and W. L. Wiese. *J. Phys. Chem. Ref. Data*, 31(3):819–927, 2002.

[39] M. S. Dimitrijević and S. Sahal-Bréchot. Stark broadening of Ca II spectral lines. *J. Quant. Spectrosc. Radiat. Transfer*, 49(2):157–164, 1993.

[40] M. S. Dimitrijević and S. Sahal-Bréchot. Stark broadening of Li I lines. *J. Quant. Spectrosc. Radiat. Transfer*, 46:41–53, 1991.

[41] D. E. Cox P. Thompson and J. B. Hastings. *J. Appl. Cryst.*, 20:79–83, 1987.

[42] F.L. Pedrotti and L.S. Pedrotti. *Introduction to Optics, 2nd ed.* Prentice Hall, 1993.

[43] J. Allington-Smith. *Basic equations for astronomical spectroscopy with a diffraction grating.* University of Durham, February 2000.

[44] Baulch, D. L. *et al.* Evaluated Kinetic Data for Combustion Modeling: Supplement II. *J. Phys. Chem. Ref. Data*, 34(3):757–1397, 2005.

[45] M. A. Lieberman and A. J. Lichtenberg. *Principles of Plasma Discharges and Materials Processing.* Wiley, 2nd edition, 2005.

[46] P.W. Atkins and J. de Paula. *Physical Chemistry.* 7th edition, 2002.

[47] G. Herzberg. *Molecular Spectra and Molecular Structure, Vol. I: Spectra of Diatomic Molecules.* Krieger Publishing Company, 1989.

[48] G. Fussmann. Atom- und Molekülphisk. Vorlesung an der Humboldt Universität zu Berlin.

[49] V. Guerra, P.A. Sá, and J. Loureiro. Kinetic modeling of low-pressure nitrogen discharges and post-discharges. *Eur. Phys. J. Appl. Phys. 28*, 28:125152, 2004.

[50] B. S. Cheong and M. Parson. Chemiluminescent reactions of group 2 (Ca, Sr and Ba) elements with H_2O_2, *t*-BuOOH, HNO_3 and NO_2: reactivities and product state distributions.

[51] J. Luque and D.R. Crosley. LIFbase: Database and Spectral Simulation Program (Version 2.0). available: `http://www.sri.com/psd/lifbase/`. Report MP 99-009, SRI International, 1999.

[52] C. de Izarra. UV OH spectrum used as a molecular pyrometer. *J. Phys. D: Appl. Phys.*, 33:1697–1704, 2000.

[53] V.I. Demidov, S.V. Ratynskaia, and K. Rypdal. Electric probes for plasmas: The link between theory and instrument. *Review of Scientific Instruments*, 73(10), October 2002.

[54] G. K. Batchelor. *An introduction to Fluid Mechanics.* Cambridge Univeristy Press, 1992.

[55] Wikipedia (`http://wikimedia.org/wiki/Image:Mushroom_cloud.svg`), credits are given to Wikimedia Commons. November 2007.

[56] H. R. Griem. Shifts of hydrogen and ionizaed-helium lines from $\Delta n = 0$ interactions with electrons in dense plasmas. *Phys. Rev. A*, 38(6), 1998.

[57] A.M. Samson and K.A. Berrington. Electron impact excitation cross sections and rates from the ground state of atomic ca. *Atomic Data and Nuclear Data Tables*, 77(1):87–95, January 2001.

[58] V. Ehlers and A. Gallaghar. *Phys. Rev. A.*, 7:1573, 1973.

[59] G. Crandall, G.H. Dunn, D. Gallagher, Hummer C.V., D. Kunasz, D. Leep, and P.O. Taylor. *Astrophys. J.*, 191:789, 1974.

[60] H. P. Summers. *The ADAS User Manual, version 2.6 http://adas.phys.strath.ac.uk*, 2004.

[61] D Husain and J Schifino. *J. Chem. Soc. Faraday Trans.*, 2(79):1265, 1983.

[62] R W B Pearse and A G Gaydon. *The Identification of Molecular Spectra*. New York: Wiley, 1950.

[63] A. G. Gaydon. Green and orange band spectra of caoh, caod and calcium oxide. *Proceedings of the Royal Society of London. Series A, Mathematical and Physical Sciences*, 231(1187):437–445, 1955.

[64] R. F. Wormsbecher, M. Trkula, C. Martner, R.E. Penn, and D. O. Harris. Chemiluminescent reactions of alkaline-earth metals with water and hydrazine. *Journal of Molecular Spectroscopy*, 97:29–36, 1983.

[65] M. D. Oberlander, Kampf R.P., and J.M. Parson. Chemiluminescence reactions of ca with hydrogen peroxide. *Chemical Physics Letters*, 176(3,4):395–389, 1991.

[66] J. Luque and D.R. Crosley. Transition probabilities in the $A^2\Sigma^+ - X^2\Pi_i$ electronic system of OH.

[67] M. Tamura, P. A. Berg, J. E. Harrington, J. Luque, J. B. Jeffries, G. P. Smith, and D. R. Crosley. Collisional Quenching of CH(A), OH(A), and NO(A) in Low Pressure Hydrocarbon Flames. *Combustion and Flame*, 114:502–514, 1998.

[68] E. R. Lyman. Rotational Energy Distribution of OH Molecules from the λ3064 Band. *Phys. Rev.*, 53:379, 1938.

[69] H. P. Broida and W. R. Kane. Rotational Intensity Distribution of OH and OD in an Electrodeless Discharge through Water Vapor. *Phys. Rev.*, 89(5):1053–1059, 1953.

[70] G. H. Dieke and H. M. Crosswhite. The Ultraviolet Bands of OH. *J. Quant. Spectrosc. Radiat. Transfer*, 2:97–199, 1961.

[71] G. R. Möhlmann, C. I. M. Beenakker, and F. J. de Heer. The rotational excitation and population distribution of OH($A^2\Sigma^+, v' = 0$) produced by electron impact on water. *Chemical Physics*, 13:375–385, 1975.

[72] R. Rabat and C. de Izarra. Check of OH rotational temperature using an interferometric method. *J. Phys. D: Appl. Phys.*, 37:2371–2375, 2004.

Appendix A

Pyroelectric sensor calibration

The pyroelectric sensor consists of a circular thin sheet of black pyroelectric material, with a high absorption coefficient (higher than 97 % in the wavelength range of 0.2–20 μm). The pyroelectric material generates an electrical potential when its temperature changes, *i.e.* when it is heated or cooled. This potential difference is the output signal of the pyrosensor. At short timescales (< 1 s) the output is proportional to the radiation power. The constant of proportionality was determined by calibration using a light bulb and a calibrated radiation power meter. The light from the light bulb was collimated to uniformly fill the sensor surface and power of the same collimated light beam was measured using the radiation power meter, at various intensities. The result of this calibration procedure is shown in figure A.1 below. The constant of proportionality determined from the fit is used for all measurements. The response time of the pyrosensor was determined by using a chopped light beam, as shown in the inset. The response time depends only weakly on the radiation power in the measured range and is characterized by a rise time (from 10 to 90 % of the maximum) of just below 20 ms. It should be noted that the measured intensities were in some cases above the range used for calibration, *e.g.* up to $I_{\mathrm{rad}} \approx 850$ Wm^{-2} at 66 cm from the electrode (figure 3.7 (c)).

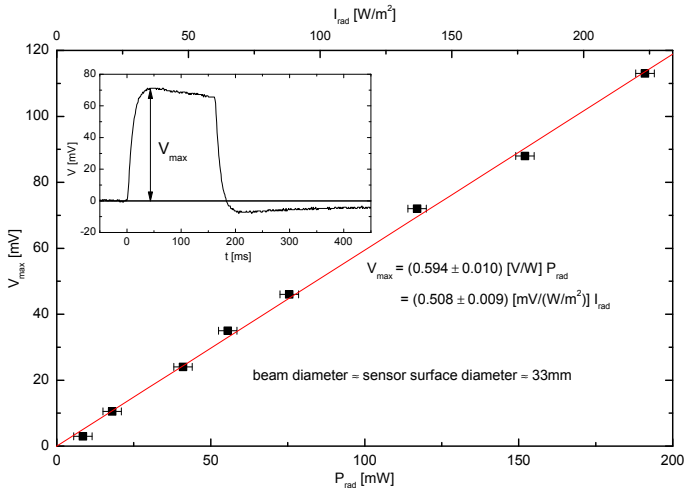

FIGURE A.1: *Results of the pyroelectric sensor calibration. The lower horizontal axis shows the radiation power incident on the pyroelectric sensor. The upper horizontal axis is the corresponding average intensity on the sensor surface.* V_{max} *is the maximum value of pyrosensor's output voltage, using a pulsed light source. The inset shows a typical time-dependent output signal of the pyrosensor, when illuminated with the pulsed light source.*

Appendix B

Data collection

A systematic storage of experimental data was desirable to make sure the collected data is available and easily accessible, also to other persons involved in the project and after experiments have been stopped. A database system was developed, using a simple web-interface (PHP+MySQL) so the data could be accessed from anywhere in the network. A shot-number was introduced to link all data (*e.g.* results of several diagnostics, discharge parameters and remarks) belonging to a particular experiment. Images of the web-interface is shown figure B.2 and B.1. In all data of more than 1,000 shots has been collected and stored in the database.

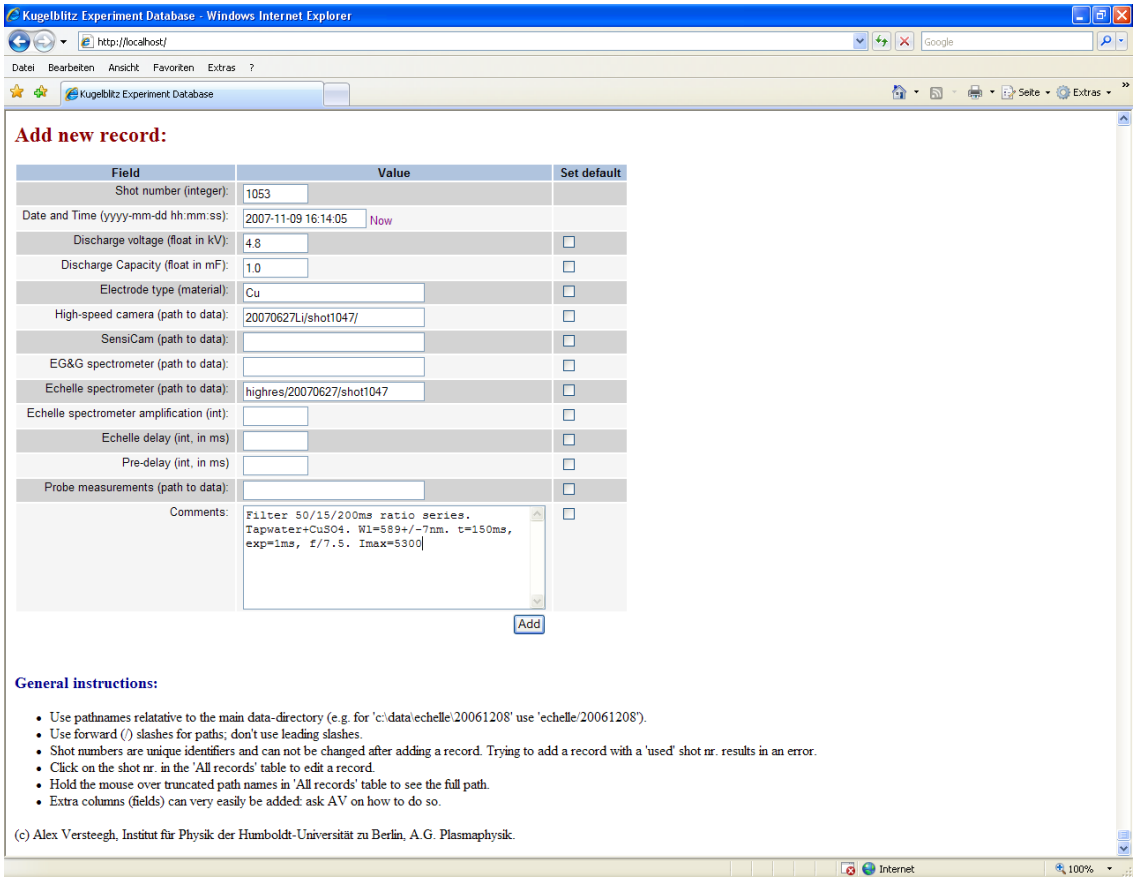

FIGURE B.1: *User interface for adding new records to the database.*

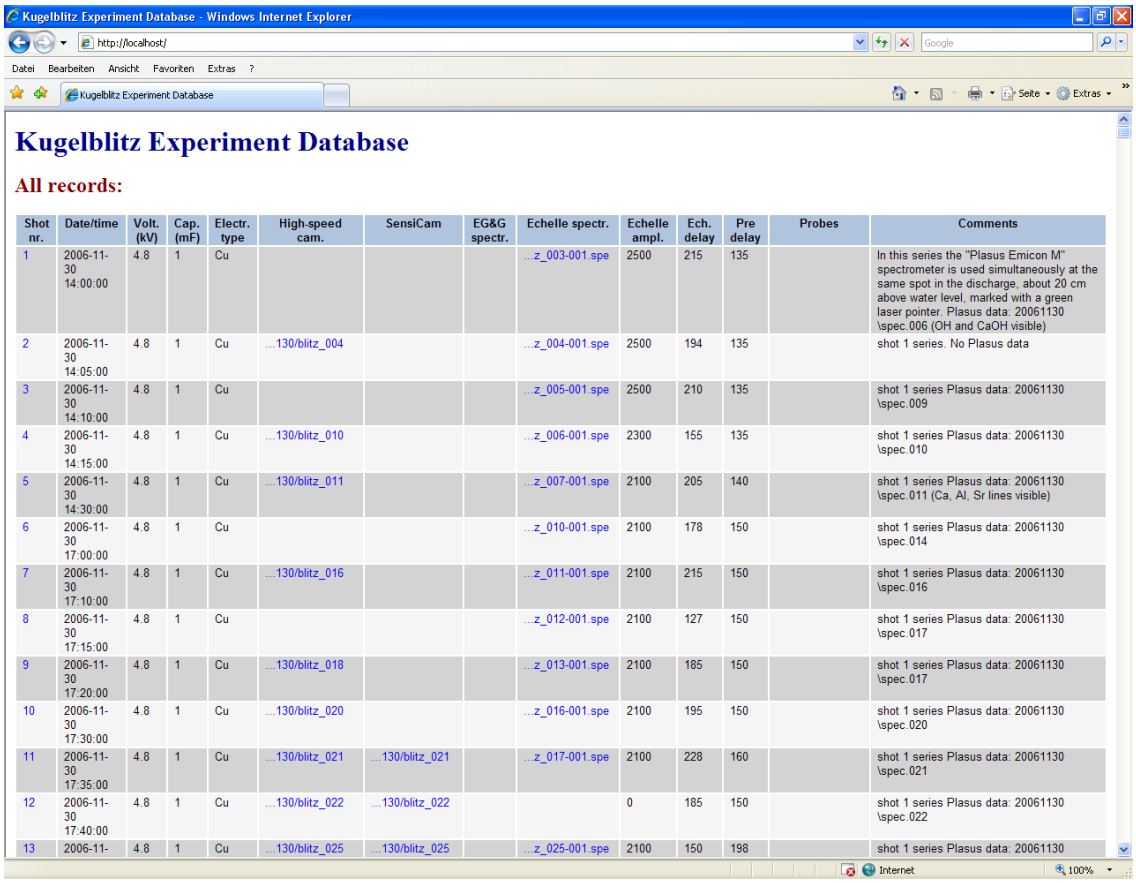

Shot nr.	Date/time	Volt. (kV)	Cap. (mF)	Electr. type	High-speed cam.	SensiCam	EG&G spectr.	Echelle spectr.	Echelle ampl.	Ech. delay	Pre delay	Probes	Comments
1	2006-11-30 14:00:00	4.8	1	Cu				...z_003-001.spe	2500	215	135		In this series the "Plasus Emicon M" spectrometer is used simultaneously at the same spot in the discharge, about 20 cm above water level, marked with a green laser pointer. Plasus data: 20061130 \spec.006 (OH and CaOH visible)
2	2006-11-30 14:05:00	4.8	1	Cu	...130/blitz_004			...z_004-001.spe	2500	194	135		shot 1 series. No Plasus data
3	2006-11-30 14:10:00	4.8	1	Cu				...z_005-001.spe	2500	210	135		shot 1 series Plasus data: 20061130 \spec.009
4	2006-11-30 14:15:00	4.8	1	Cu	...130/blitz_010			...z_006-001.spe	2300	155	135		shot 1 series Plasus data: 20061130 \spec.010
5	2006-11-30 14:30:00	4.8	1	Cu	...130/blitz_011			...z_007-001.spe	2100	205	140		shot 1 series Plasus data: 20061130 \spec.011 (Ca, Al, Sr lines visible)
6	2006-11-30 17:00:00	4.8	1	Cu				...z_010-001.spe	2100	178	150		shot 1 series Plasus data: 20061130 \spec.014
7	2006-11-30 17:10:00	4.8	1	Cu	...130/blitz_016			...z_011-001.spe	2100	215	150		shot 1 series Plasus data: 20061130 \spec.016
8	2006-11-30 17:15:00	4.8	1	Cu				...z_012-001.spe	2100	127	150		shot 1 series Plasus data: 20061130 \spec.017
9	2006-11-30 17:20:00	4.8	1	Cu	...130/blitz_018			...z_013-001.spe	2100	185	150		shot 1 series Plasus data: 20061130 \spec.017
10	2006-11-30 17:30:00	4.8	1	Cu	...130/blitz_020			...z_016-001.spe	2100	195	150		shot 1 series Plasus data: 20061130 \spec.020
11	2006-11-30 17:35:00	4.8	1	Cu	...130/blitz_021	...130/blitz_021		...z_017-001.spe	2100	228	160		shot 1 series Plasus data: 20061130 \spec.021
12	2006-11-30 17:40:00	4.8	1	Cu	...130/blitz_022	...130/blitz_022			0	185	150		shot 1 series Plasus data: 20061130 \spec.022
13	2006-11-	4.8	1	Cu	...130/blitz_025	...130/blitz_025		...z_025-001.spe	2100	150	198		shot 1 series Plasus data: 20061130

Figure B.2: *Overview of all data.*

Appendix C

Échelle spectrometer calibration

For the calibration of the échelle spectrometer two sets of data were used. Both were obtained from U. Fantz. The first is the spectrum of a deuterium lamp with known intensity in the range of 200 nm to 800 nm (approximately). The corresponding calibration curve (spectral intensity per count) is shown as the blue line in figure C.1 (a). This calibration was conducted in September 2003, using slightly different optics than used in the experiments here. Therefore a second calibration was done in November 2006, shortly before starting the measurements, using the same optics as in measurements. This second calibration uses an Ulbricht sphere with known intensity between 380 nm to 800 nm (at shorter wavelengths the intensity drops steeply). This is the green curve in figure C.1 (a). The final calibration curve is obtained by scaling the deuterium lamp calibration curve, up to the level of the more recent Ulbricht sphere calibration. Since quartz optics (fiber+lense) were used, an absolute calibration up to the near UV (approximately 280 nm is obtained.

The 'exposure time' of the intensified CCD is controlled by two parameters. The first is the length t_{mcp} of the pulse used to drive the multichannel plate. The maximum width is 12 ms according to manufacturer specifications. When a $t_{\mathrm{mcp}} < 12$ ms (*e.g.* $t_{\mathrm{mcp}} = 6$ ms was often used) the calibration curve was scaled accordingly (by a factor (12 ms)/t_{mcp}). In fact, the effect of the MCP pulse length on the sensitivity may not be exactly linear. This was not investigated further.

The second possibility to influence the 'exposure' is by adjusting the voltage V_{mcp} of the multichannel plate. All calibration curves were taken at $V_{\mathrm{mcp}} = 2900$ V. Higher (lower) values of this voltage resulted in higher (lower) sensitivity. The effect is approximately equal over the spectral range and results in an additional calibration factor, shown in figure C.1 (b). The ability to control the MCP voltage serves as an independent 'amplifier' and proved very convenient for measuring the wide range of intensities throughout the plasmoids lifetime. Values of V_{mcp} greater than 3000 V result in a noticeable increase of the amount of noise in the recorded spectra.

The major sources of error in the absolute calibration are expected to be:

- the possible non-linear response of the sensitivity to t_{mcp},
- absorption of air at wavelengths < 300 nm (no correction for this is made, as results at these wavelengths were rarely used),
- inaccuracy of the Ulbricht spheres specifications.

In all, the accuracy of absolute intensities is estimated at 50%. The accuracy of relative intensities is much better ($< 10\%$), depending on the difference in wavelength.

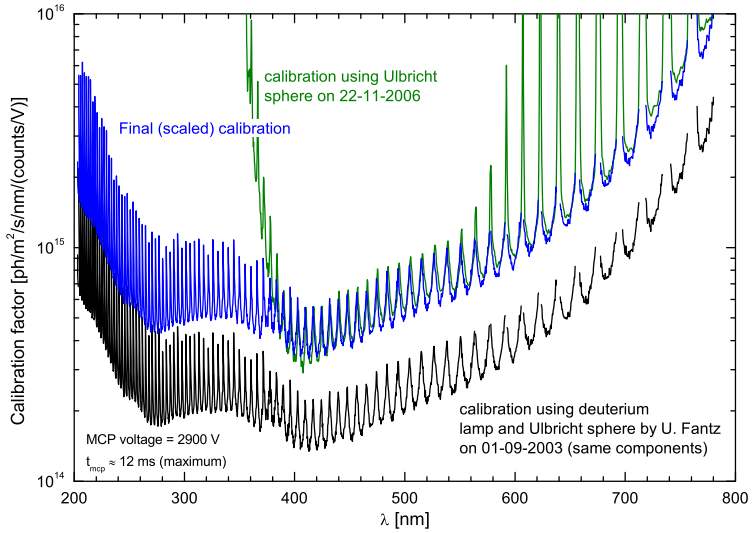

(a) absolute spectral calibration factors

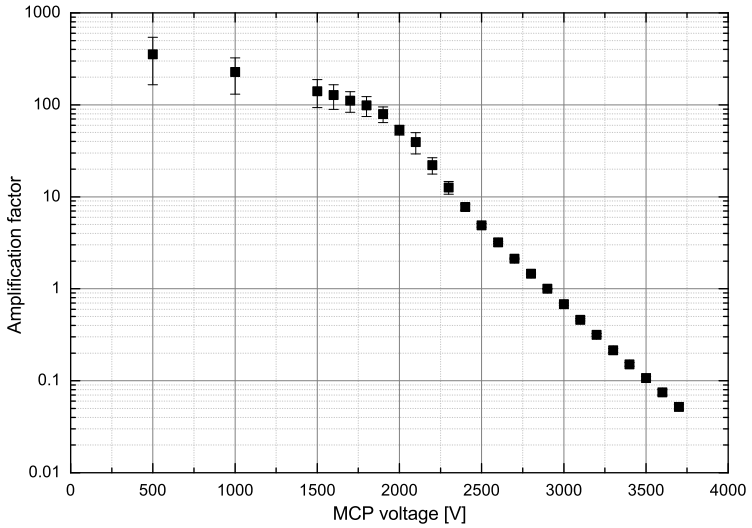

(b) multichannel plate (MCP) amplification factor

FIGURE C.1: *Echelle spectrometer calibration curves. The absolute spectral radiance in* $[photons \cdot m^{-2} s^{-1} nm^{-1}]$ *is given by the number of counts times the spectral calibration factor, which is the blue curve in figure (a), times the amplification factor of the multichannel plate, determined by* V_{mcp} *using figure (b) times* $(12\ ms)/t_{mcp}$.

Appendix D

H-beta Stark broadening

The next two pages show measurement of the Stark-broadened H_β line recorded using the échelle spectrometer (top view, at $r = 0$) at various times in the initial phase of the discharge. The data has been fitted using Lorentz profile. The fit parameters are used for determining the electron density in section 3.4.2.

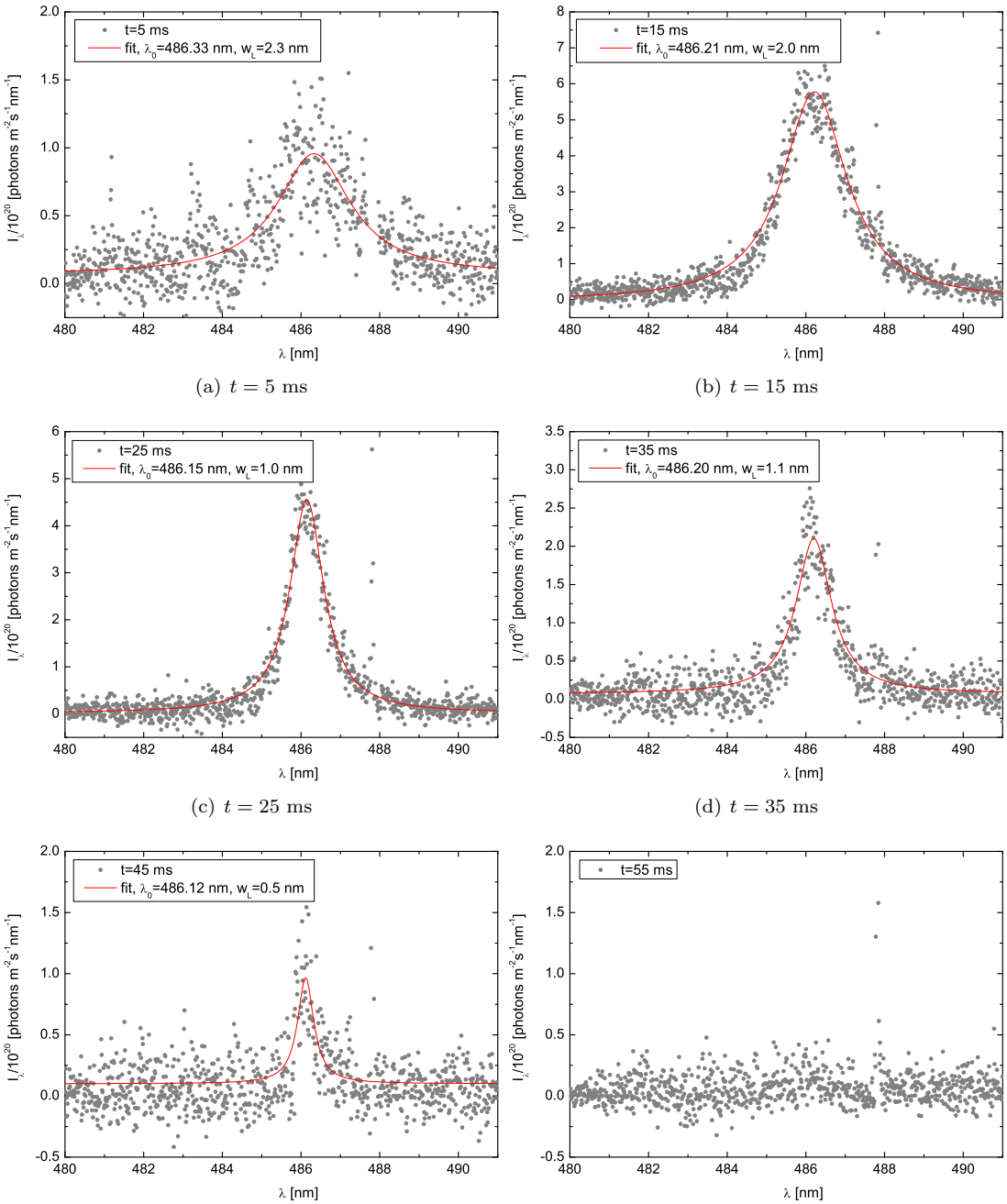

(a) $t = 5$ ms (b) $t = 15$ ms

(c) $t = 25$ ms (d) $t = 35$ ms

(e) $t = 45$ ms (f) $t = 55$ ms

FIGURE D.1: *Fitted H_β line at various times, recorded with the échelle spectrometer using tap water with 0.4 g/l $CaCl_2$. The lines were fitted with a Lorentz profile of width w_L (FWHM) and line center λ_0 as indicated in each legend.*

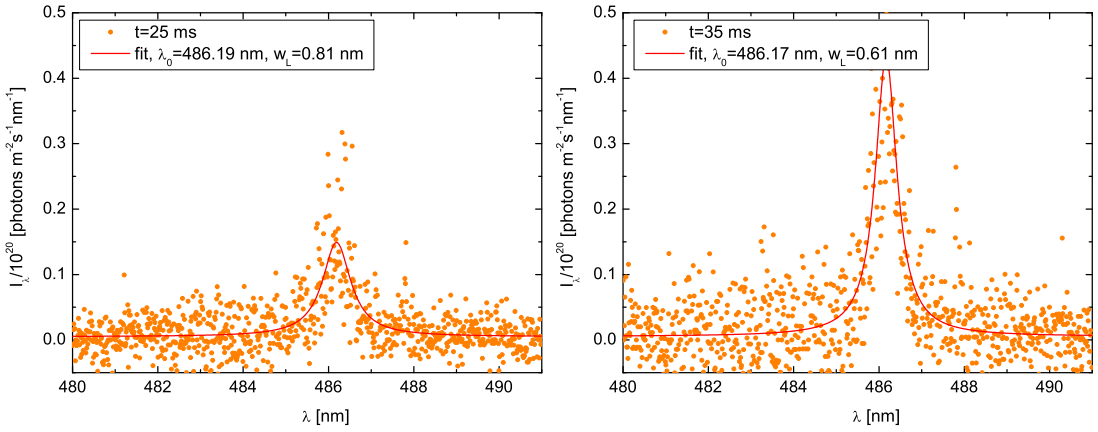

(a) $t = 25$ ms (b) $t = 35$ ms

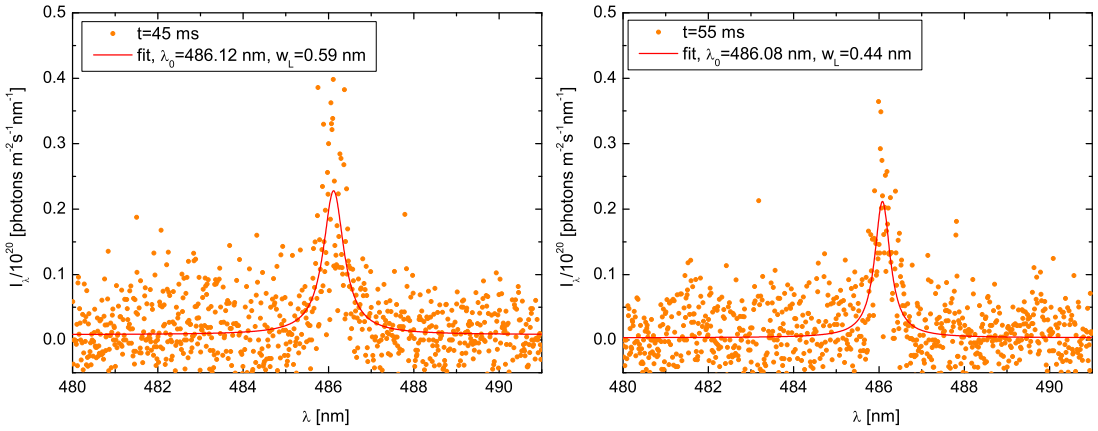

(c) $t = 45$ ms (d) $t = 55$ ms

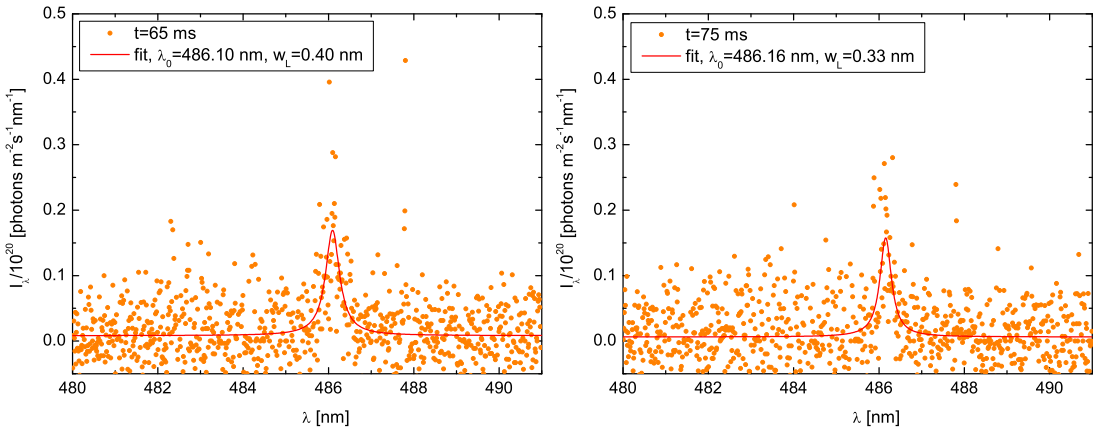

(e) $t = 65$ ms (f) $t = 75$ ms

FIGURE D.2: *Fitted H_β line at various times, recorded with the échelle spectrometer using tap water with 0.3 g/l $CaCl_2$. The lines were fitted with a Lorentz profile of width w_L (FWHM) and line center λ_0 as indicated in each legend.*

Appendix E

Additional CRM results

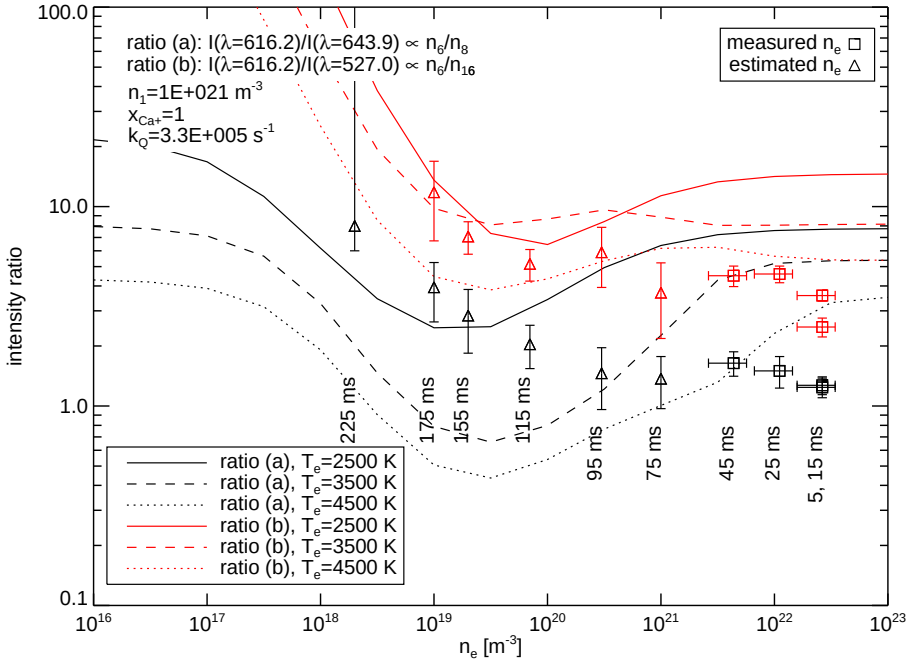

FIGURE E.1: *Same line ratio as in figure 4.10, but with a quenching rate* $k_Q = 3.3 \cdot 10^5\ s^{-1}$*, as is used in all other results of the collisional radiative model. Now, the line ratio (a) is lower by approximately a factor 1.5, as compared to 4.10, and consistency of* n_e *and* T_e *values obtained from both line pairs is not as good.*

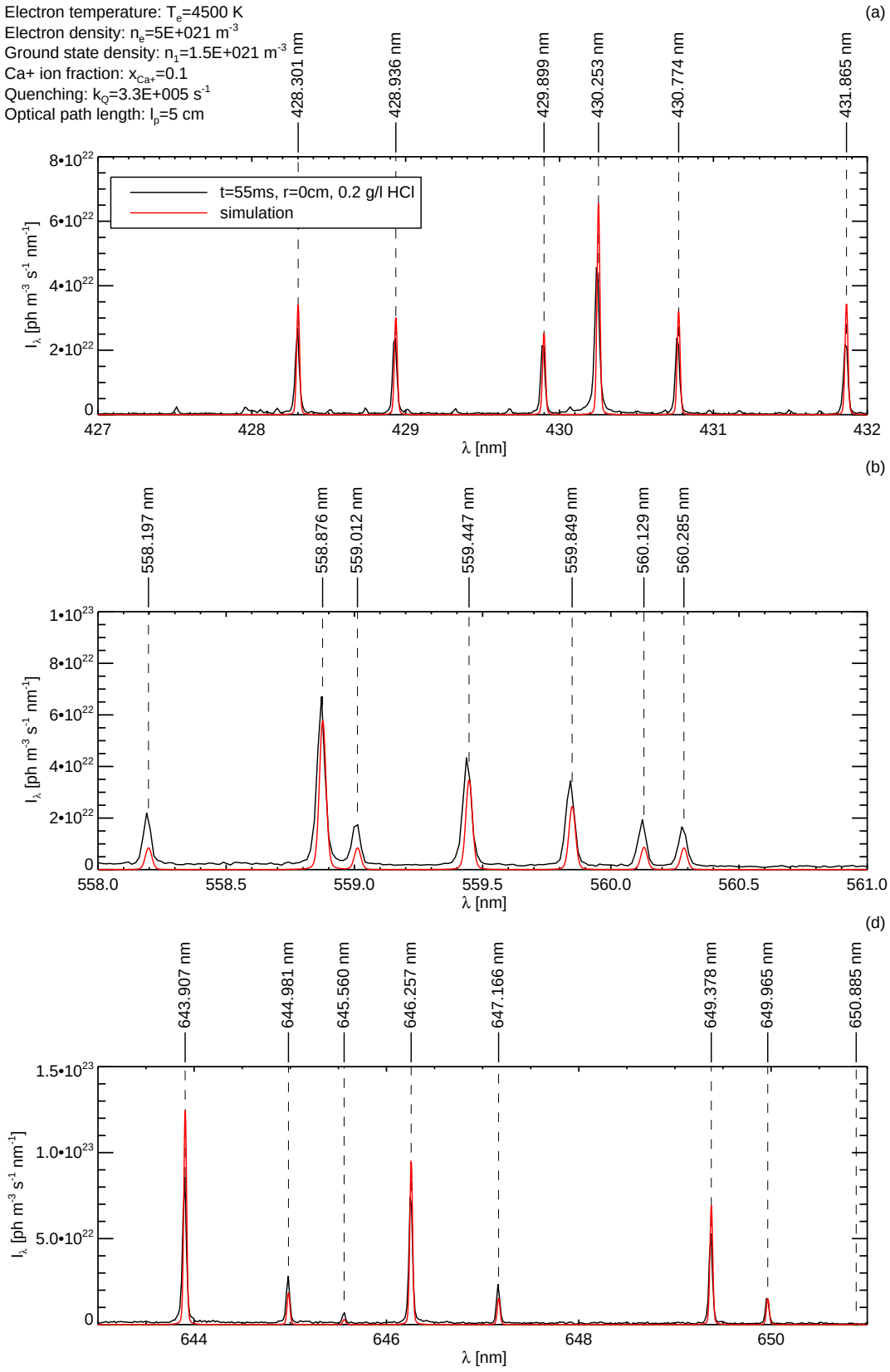

FIGURE E.2: *Measured and simulated calcium emission spectrum. The measured spectrum was recorded at $r = 0$ and t=55 ms (top view). The simulation parameters are shown in the top left corner.*

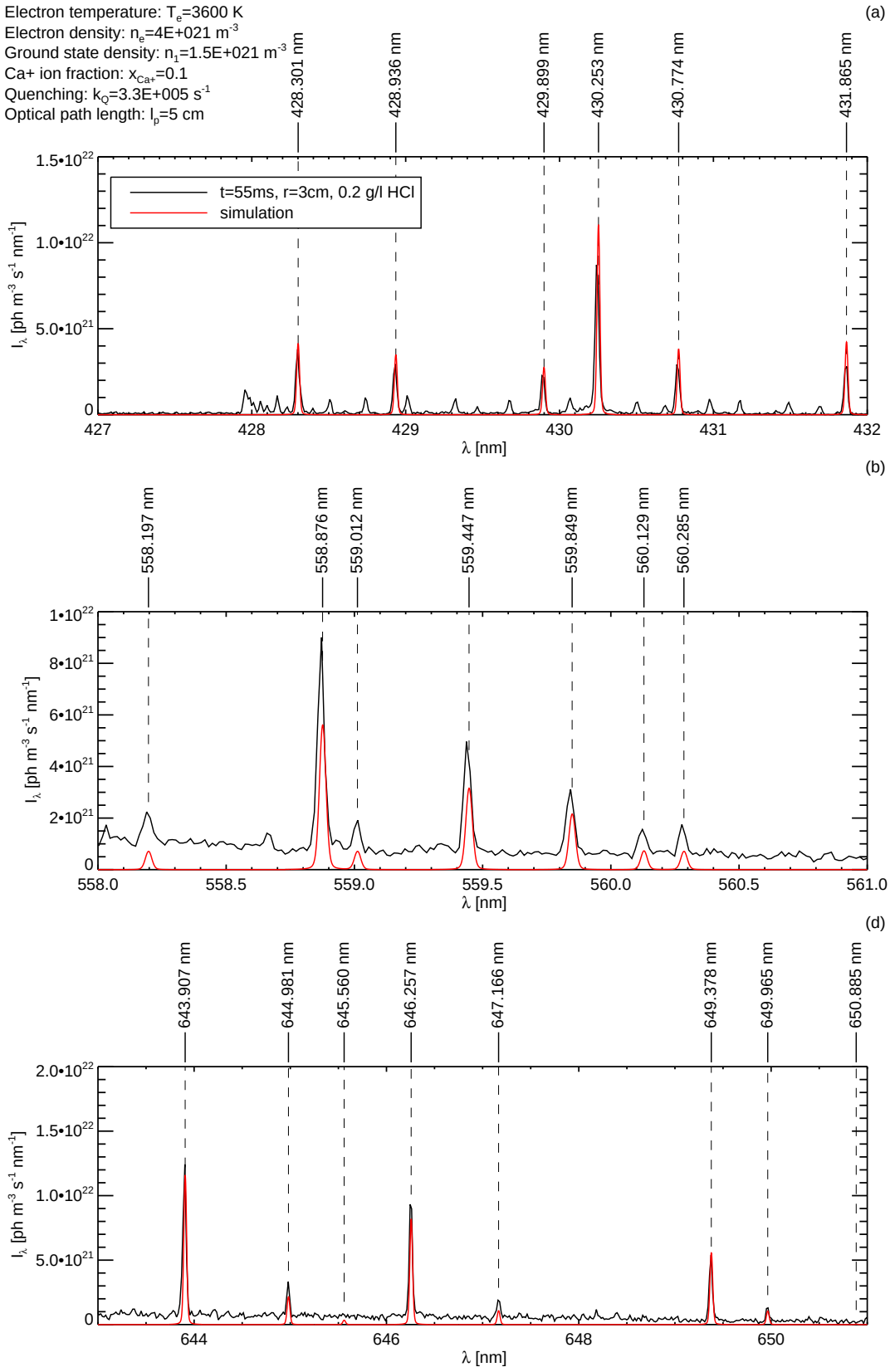

FIGURE E.3: *Measured and simulated calcium emission spectrum. The measured spectrum was recorded at $r = 3$ and t=55 ms (top view). Note that in the central figure the optical thickness is somewhat overestimated (from the relative intensities of the lines from the same multiplet).*

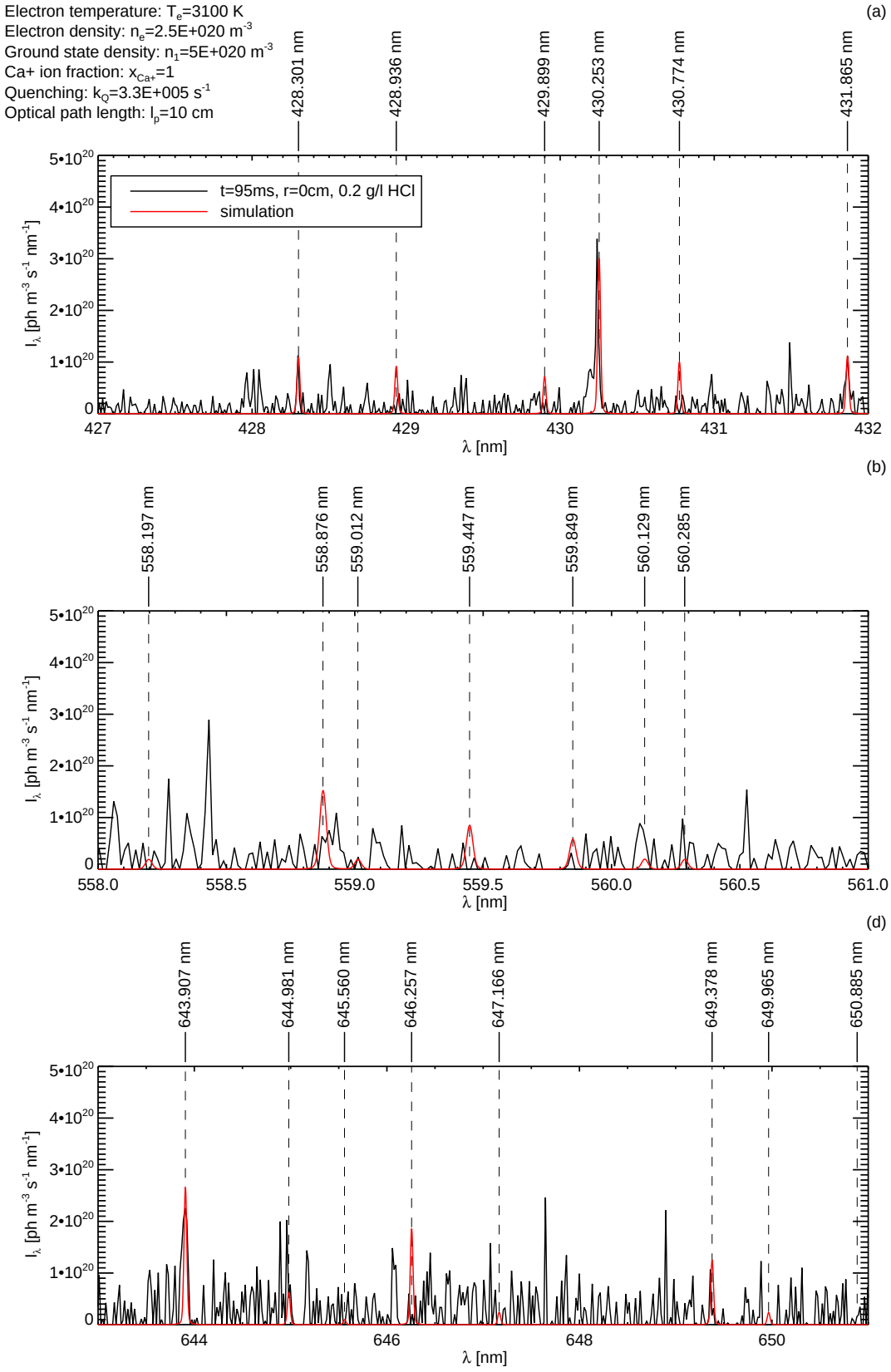

FIGURE E.4: *Measured and simulated calcium emission spectrum. The measured spectrum was recorded at $r = 0$ and t=95 ms (top view).*

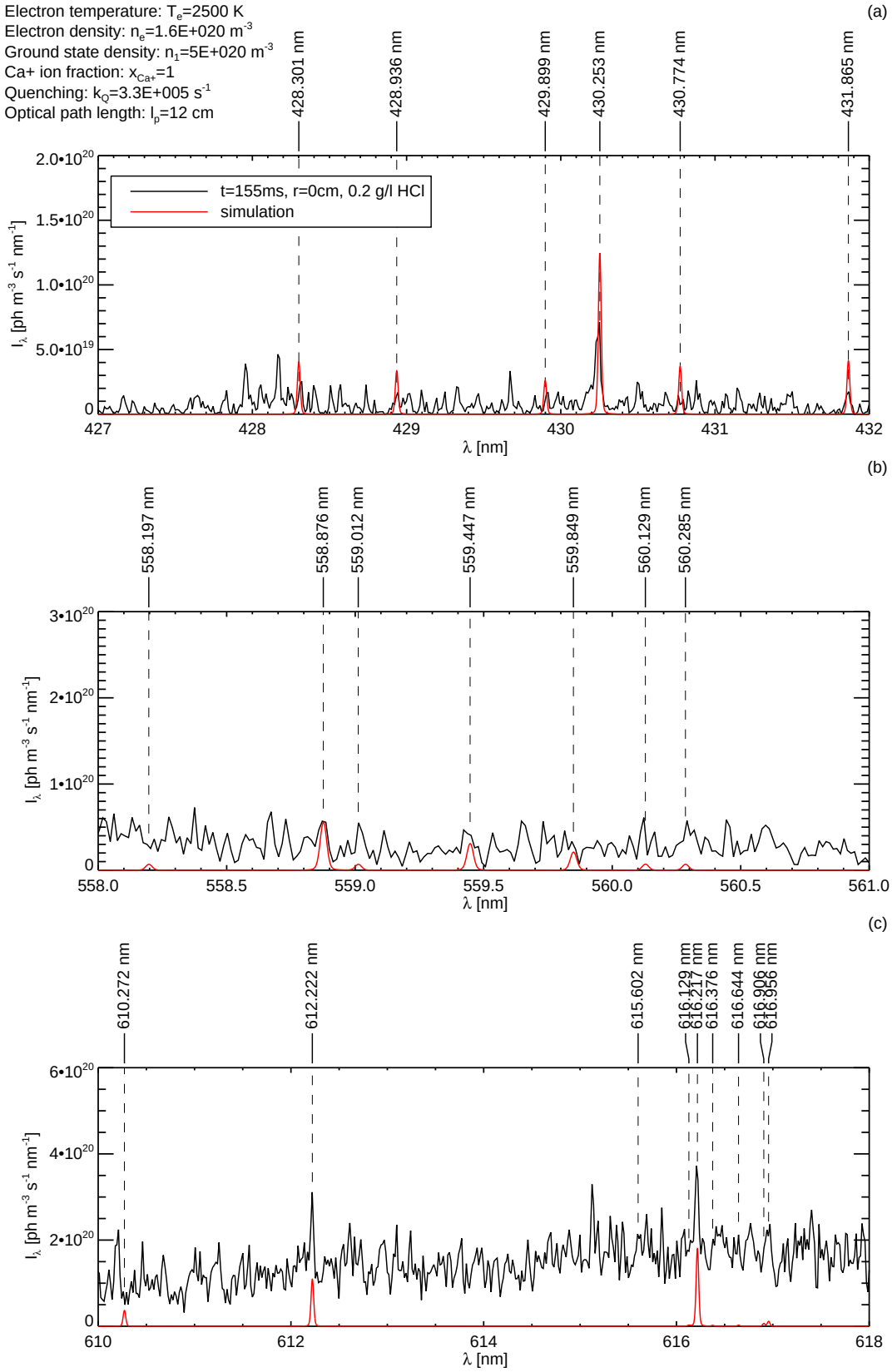

FIGURE E.5: *Measured and simulated calcium emission spectrum. The measured spectrum was recorded at $r = 0$ and t=155 ms (top view).*

Appendix F

Submitted article